UNIVERSITY OF CRETE
DEPARTMENT OF MATERIALS SCIENCE AND TECHNOLOGY

# "Non-linear micro/nanolithography with short-pulse lasers: applications on biomaterials and biosensors"

**PhD thesis:**

**Konstantina Terzaki**

**Supervisors: Assoc. Prof. Anna Mitraki**
**Dr. Maria Farsari**

FORTH
Institute of Electronic Structure and Laser

November 2013

**Abstract**

The present PhD thesis focuses on the combination of two strategies: the top-down laser fabrication (i.e. the possibility to control the scaffold geometry and micro-nano-topography) and the bottom-up design possibilities of the self-assembling peptides (driving self-assembly from the nanoscale to millimeter scale) for the development of biocompatible high-precision scaffolds with complex architectures. The positioning and integration of self-assembled peptides into devices fabricated with femtosecond laser technologies was examined for applications in the field of biomaterials and photonics.

3D scaffolds with microscale features were fabricated with Direct femtosecond Laser Writing (DLW). The 3D structures were synthesized using a novel zirconium-containing organic-inorganic photosensitive material incorporating a metal-binding organic monomer in order to be further functionalized with metal-binding peptide fibrils. The scaffolds' resolution in structurability and metallization quality was investigated as well as their mechanical properties and their biocompatibility.

The precise positioning of self-assembled peptide fibrils, their controlled assembly and their integration into microsystems was investigated. Conductive 3D metallic micro/nanostructures were fabricated using a silver plating technique and subsequently previously studied metal-binding peptide fibrils were selectively positioned over the metalized structures forming oriented peptide bridges which were metalized in situ. The developed system can be proposed for conductivity measurements of self-assembled peptide fibrils and its use in the field of biosensing is highly envisaged.

Based on a previously studied octapeptide building block, bi-functional self-assembling oligopeptides were designed, having acidic amino acids in their sequence in order to nucleate calcium phosphate as well as metal ions. The self-assembled peptide fibrils were positioned on gold-ion functionalized 3D structures and subsequently acted as secondary scaffolds for the deposition of calcium phosphates aiming at hard tissue regeneration. Pre-osteoblastic cell adhesion, proliferation and a statistically significant increase of biomineralization makes the scaffold a promising method for bone tissue engineering.

## Acknowledgements

I would like to thank my supervisor Assoc. Prof. Anna Mitraki, at the Materials Science and Technology Department for her advice and guidance to perform this PhD thesis and for contributing to collaborate with scientists from abroad that have imparted their experimental techniques to fundamental parts of my work.
I would also like to express my gratitude to my advisor Dr. Maria Farsari for guiding my research at FORTH in the non-linear lithography lab, for her support and encouragement to surpass the several difficulties encountered.

I wish to thank the other members of my supervising committee, Prof. Maria Vamvakaki for her contribution in my research and her collaboration, and of course Prof. Costas Fotakis, being the first person to contact with six years ago, who contributed for working initially at the Institute of Electronic Structure & Laser and for starting a PhD later.

I need to thank also Assist. Prof. Maria Chatzinikolaidou for the collaboration and for being a member in my defense committee, as well as Prof. George Chalepakis, Prof. Irene Athanassaki and Prof. Michael Kokkinidis for accepting to take part in my defense committee.

It would not have been possible to arrive to the end of this doctoral thesis without the help and support of The Electron Microscopy Facility people Aleka Manousaki, Alexandra Siakouli, Stefanos Papadakis and Katerina Tsagaraki in the Microelectronics group, for their practical and general support in microscopy issues as well as in more general topics.

The students being in both the biomaterials and the laser lab I have been working with, contributed in many positive ways. Arune Gaidukeviciute being the first person to collaborate with, inspired me in carrying through some endless and disappointing experiments after spending several night hours in the lab. The rest old and new people of

the group for the perfect communication: Alexandros Selimis, Vassilia Melissinaki, Elmina Kabouraki, Mary Manousidaki, Leoni Georgiadi, Aggelos Xomalis, Argiro Giakoumaki, Stratos Galanopoulos, and last but not least Paulius Danilevicius who left the group suddenly.
At the biomaterials lab I would like to thank Ariadni Prigipaki, Manolis Kasotakis, and Vangelis Georgilis for the effective communication and idea exchange in the moments needed, as well as the new students Grazziano Deida, Rena Ornithopoulou and Chrissa Kokkotidou.
Ioanna Sakellari, Anthi Ranella and Hara Simitzi, as well as all my friends and my family who motivated me in their own way to accomplish this goal.

This research has been financed by the Greek national funds through the Operational Program "Education and Lifelong Learning" of the National Strategic Reference Framework (NSRF) - Research Funding Program: Heracleitus II.

**Contents**

A. EXAMPLES OF NATURAL BOTTOM-UP PROCESSES

1. Introduction ……9

1.1 Strategies for material fabrication: ‘Top-down’ and ‘bottom-up’ approach…...…9

1.2 Examples of macromolecular assemblies in nature…….…….……..9

2. Natural strategies for composite material fabrication (Biomineralization)…….……...11

2.1 Biological composite materials …….11

2.2 Biomineralization …….……...….11

2.3 Shells - Calcium carbonate…….…….…..12

2.4 Calcium phosphate – hydroxyapatite……...….14

2.5 Organic matrix……..…...16

2.6 Introduction to Bone……17

2.6.1 Structural hierarchy in bone…….....18

2.6.2 Bone mineralization……..…20

2.6.3 Bone cells…….…20

2.7 Introduction to tooth and Structural hierarchy……..…...22

2.8 Epitaxy - Structural matching…….…….....23

3 Bone Tissue Engineering…….……..25

3.1 The concept of tissue engineering…….…….....25

3.2 Bone tissue engineering…….…….…26

3.3 Biomaterials…….…….....27

4. Self-Assembly and Amyloid Fibers……..……..28

4.1 Amyloid fibrous assemblies…….…….…..29

4.2 Self-assembling peptides…….…...30

4.3 Applications of biomolecular templates for nanowire fabrication.....31

4.4 The adenovirus……...33

B. HYBRID MATERIAL PROCESSES

1. Scaffold fabrication techniques…….……37

2. Stereolithography …….38

2.1 Stereolithography with Femtosecond Lasers……38

2.2 Photopolymerization - Multi-Photon polymerization technique……....….39

2.3 The mechanism of Two-Photon Absorption ……40

2.4 The diffraction limit…….....…42

2.5 Advantages of MPP……...……..42

2.6 Materials for MPP…….....43

3. Hybrid materials …….....43

3.1 The Sol-Gel method…….....43

3.2 Hybrid material fabrication with the sol-gel method.....44

3.2.1 Hydrolysis and condensation .....45

3.2.2 Gelation.....45

3.2.3 Aging.....46

3.2.4 Drying.....41

C. THESIS RATIONALE.....47

D. EXPERIMENTAL PART

1. TECHNIQUES

1.1 Transmission electron microscopy (TEM) .....49
1.2 Scanning Electron Microscopy (SEM) .....50
1.3 Energy-Dispersive X-ray Spectroscopy (EDS) .....51
1.4 Optical microscopy.....51
1.5 Atomic Force Microscopy (AFM) .....52
1.6 X-Ray Fiber Diffraction.....53
1.7 Selected – Area – Diffraction technique (SAED) .....53
1.8 Nanoindentation test.....54

**2.** MATERIALS AND METHODS

**2.1** Proteins and FMN.....56
**2.2** Peptides.....56
**2.3** Hybrid materials.....57
**2.4** 3D hybrid structure fabrication with DLW.....60
**2.5** Polymeric thin film preparation.....61
**2.6** Mineralization protocol of amyloid peptide fibrils with calcium phosphate on a holley grid.....61
**2.7** Mineralization of amyloid peptides with calcium phosphate in solution.....62
**2.8** Scaffold mineralization with calcium phosphate.....62
**2.9** Metallization protocol of amyloid peptide fibrils .....63
**2.10** Scaffold functionalization with metal-binding amyloid peptides.....64
**2.11** Electroless plating protocols for 3D conducting nanostructures.....65
**2.12** Functionalization of conductive 3D structures with amyloid peptides and further metallization.....67
**2.13** Conductivity measurements.....67
**2.14** X-ray Diffraction (XRD) .....67
**2.15** Transmission measurements for photonic crystals.....67
**2.16** Nanoindentation test.....67
**2.17** Transmission electron microscopy (TEM).....68
**2.18** Scanning Electron Microscopy (SEM) – Field Emission SEM (FESEM).....67
**2.19** Energy – Dispersive X – ray Spectroscopy (EDS).....67
**2.20** Optical microscopy.....67
**2.21** AFM imaging.....69
**2.22** X-ray Fiber Diffraction.....69
**2.23** Selected – Area – Diffraction technique (SAED) .....70

E. RESULTS AND DISCUSSION

**4.** Applications in 3D patterning of self-assembled peptides on hybrid structures-Part 1: Metallized structures for biosensing.....71
4.1 Fabrication of 3D conducting structures.....71
4.2 Directed 3D patterning of self-assembled peptides on hybrid microstructures and further metallization..... 79

**5.** Applications in 3D patterning of self-assembled peptides on hybrid structures - Part 2: Scaffolds for hard tissue engineering.....84
5.1 Novel material fabrication and characterization of their mechanical properties and biological response.....84
5.2 Mineralized self-assembled peptides on 3D laser-made scaffolds: A new route towards ‘scaffold on scaffold’ hard tissue engineering.....86
**6.** Photocrosslinking of protein microstructures: evaluation of processability and bioactivity.....98

F. GENERAL CONCLUSIONS AND OUTLOOK.....102

G. BIBLIOGRAPHY.....104

# A. EXAMPLES OF NATURAL BOTTOM-UP ROCESSES

## 1. Introduction

### 1.1 Strategies for material fabrication: ‘top-down’ and ‘bottom-up’ approach

The need for the evolution of material science arises since the prehistoric period when the earliest human species had access to materials occurring naturally including stone, wood and clay, the development of which was characterizing their civilization (Stone Age, Bronze Age, Iron Age). With time techniques were discovered for producing materials with superior properties with the help of technology meeting the needs of modern society.

The traditionally used approach for material fabrication is the ‘top-down’ approach, where nanoscale devices are being created using larger, externally controlled ones to direct their assembly. Micropatterning techniques, such as photolithography and inkjet printing belong to this category, but disadvantages including the high cost of equipment and materials needed, low biocompatibility and poor resolution led to the need for evolution of another kind of approach.

Since the critical limit of resolution of a material structure is being confined by the physical properties of matter, the 'bottom-up' approach would be more appropriate for material fabrication, where strong and specific interactions of molecules that are energetically favourable, based on non-covalent interactions are involved. Viruses, amyloid fibrils and nucleic acids are some of the examples of nature that organize their molecules in a ‘bottom-up’ approach (Gazit 2008),(Gazit 2007). The building blocks for this process vary considerably and include both organic and inorganic species. Peptides is a characteristic example being described by the ‘bottom-up’ approach due to the simplicity and their ability to be decorated with chemical and biological molecules.

### 1.2 Examples of macromolecular assemblies in nature

Fibrous proteins are macromolecular assemblies, usually inert and insoluble to water, which have interesting mechanical and elastic properties, being the inspiration for the design of novel fibrous biomaterials. Protein filaments are long proteins lacking true tertiary structure, extending mainly in two dimensions. These proteins can be found intracellularly and extracellularly. Intracellularly three distinct but interconnected, filament systems are composing the cytoskeleton (microfilaments), which are the actin filaments, microtubules and intermediate filaments. They are all involved in the generation of cellular movements. Fibrous proteins found extracellularly are collagen and keratin that can self-assemble into ligaments and hair. Some other fibrous proteins can be found also in nails and tendons.

Collagen

Collagen is found in connective tissue of mammals. The skin, the ligaments, the tendons, the teeth and the bones are constituted of collagen. The structure of collagen is a triple helix of three polypeptide chains, which can be combined in more than one way. Thus, there have been identified more than 30 different types of collagen.
The sequence of the polypeptide chain of collagen has the following repetitive sequence in which every third residue is glycine (Gly):

-Gly-Xaa-Yaa−Gly-Xaa-Yaa-Gly-Xaa-Yaa,

Xaa and Yaa are any other amino acid, most possibly proline or lysine. The triple helix is being stabilized by Van der Waals interactions while polypeptide chains are connected with hydrogen bonds. The hydrogen bond donors the amide (NH) group of one glycine and hydrogen bond acceptors the backbone carbonyl (C=O) group of residue Xaa on adjacent chains. (Whitford 2005), (Sipe 2005)

Silk fibroin

Fibroin is being produced by insects and spiders. It is made up of an array of β-strands assembled into a β-sheet and it is composed of a six residue repeat:

(Gly-Ser-Gly-Ala-Gly-Ala)*n.*

Silk is stronger than steel and more resilient than Kevlar. Its mechanical properties depend on the kind of silk. An average number of tensile strength is estimated to be 1.7 GPa, while for stainless steel is around 800 MPa. As it can be seen at the following figure of stress-strain measurements the spider silk provides the best balance of strength and toughness in comparison to other textile fibers. Its strength is attributed to the strong covalent bonds of the β-strands, where any further extension would require their breakage. This strength is coupled with flexibility due to the Van der Waals interactions that exist between the antiparallel β-strands. The intrinsic mechanical properties of silk are the reason that scientists have spent decades trying to find a way to mimic it. (Whitford 2005),(Bruce Alberts 2002),(Ko, Kawabata et al. 2001), **(**ENGINEERING PROPERTIES OF SPIDER SILK)

Flagellin

Flagellin is a protein which polymerizes to form the filaments of bacterial flagella which are their locomotory organelles. The filament is about 10 to 15 μm long and 12-25 nm in diameter, arranged in a hollow tube. In the case of e.coli flagellin protein different functional residues can be displayed on the surface of the flagellum and through genetic engineering modifications it can be templated with metal nanoparticles such as Au, Cu, Co, Pd and Cd (Erhardt, Namba et al. 2010), (Kumara, Tripp et al. 2007).

## 2. Natural strategies for composite material fabrication (Biomineralization)

### 2.1 Biological composite materials

Biological composite materials are complex structures composed of a brittle inorganic and an organic ductile part, which are relatively weak constituents, being arranged in complex hierarchical patterns. Hierarchical materials contain elements that have high order of structure, providing them with extraordinary mechanical properties. The mechanical properties of nacre, bone and other materials, based on their rich hierarchical structure have inspired the development of a large class of biomimetic materials, some of which are going to be discussed below.

Furthermore, most of the biological materials are characterized by their multifunctionality. Bone provides structural support for the body plus blood cell formation; the chitin-based exoskeleton in arthropods offers an attachment for muscles, environmental protection, and a water barrier; sea spicules offer light transmission plus structural support; and roots anchor trees plus provide nutrient transport.

Self-healing ability is another fundamental characteristic of biological materials in contrast to the synthetic ones. In nature biological fibers tent to template inorganic materials, some of which are referred below.

(Lakes 1993)

### 2.2 Biomineralization

Biomineralization is the processes by which organisms synthesize and control mineral formation in order to harden or stiffen existing tissues, where both organic and inorganic matter is involved. Biomineral depositions can be found to form exoskeletons, a phenomenon observed in mollusc shells, or endoskeletons like in vertebrates. (Krampitz and Graser 1988; Weiner 2003), (Biomineralization: conflicts, challenges, and opportunities Boskey AL)

Over half of the elements essential for life are incorporated in biomineral deposits, of which calcium is the common constituent of bones, teeth and shells. Bones and teeth are composed of calcium phosphate, shells, corals and eggs are made of calcium carbonate while amorphous silica is utilized in diatoms, sponges and several plants.

Biomineralization is a cellular detoxification process, since concentration of $Ca^{2+}$ more than $10^{-6}$mol/L has a toxic effect on the living cell. In this case calcium ions must be eliminated. Thus, since excess of ions is being detected in the cytoplasm it can be removed either intracellularly by Ca-binding proteins into the mitochondria, which is a calcium storage site and where calcium phosphate is synthesized, or it can be transported extracellularly.

Intracellular mineralization is the most widespread form of mineralization, where the biomineral is nucleated within the cell before becoming extracellular. Thus, the cell

controls mostly the process regulating the pH and pCO2, resulting in very complex morphologies. A typical example being formed with this mechanism is echinoderms. In extracellular mineralization, mineralization occurs in the outer surface of the cell where macromolecules are being produced by the cell (proteins, polysaccharides or glycoproteins) that assemble to form a three-dimensional framework. The basic components of the proteins are acidic amino acids and phosphorylated groups. The mollusk shell nacreous layer is being formed with this mechanism.
(Krampitz and Graser 1988),(Weiner 2003), (Mann 2001)

### 2.3 Shells - Calcium carbonate

Shells are made of pure calcium carbonate (CaCO3) that has different structures, of which calcite and aragonite, differing in their crystal lattice, are the most thermodynamically stable and the shells usually are made of these two calcium carbonate structures.

#### Mollusc shells- nacre

The shells of mollusks have an outer layer which is made of crystals of calcite and an inner layer (nacre), which is composed of a 'brick-wall' arrangement of plate–like aragonite crystals, where between them organic matrix mediates in order to absorb the vibrations, like mortar between the bricks of a wall.

Initially the outer layer of a shell is deposited and then the nacre starts to grow. Mollusc shells are composed of organic material (proteins, polysaccharides) which doesn't exceed 5% and 95% of minerals (calcite, aragonite). This alteration of organic and inorganic matrix in comparison to the parallel arrangement of the polygonal aragonite platelets makes them the strongest structures found in shells reaching an elastic modulus of 70 GPa, and a strength of 120 MPa. By comparison, human femoral bone is softer (E = 20 GPa) but stronger (150–200 MPa strength). The shells of molluscs are used as models for armor design due to their toughness in combination to the fact of being lightweight.

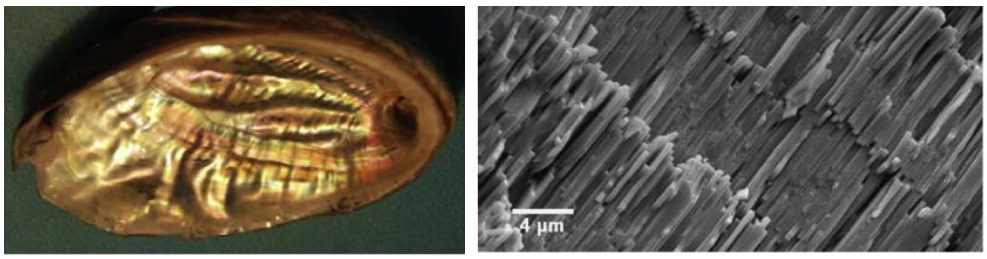


**Figure 1. (left) Photograph of the inner nacreous layer of the abalone shell, (right), Scanning Electron Microscopy of the fracture surface of the cross-section of N. pompilius septum, showing the layered structure of nacre (Nudelman, Gotliv et al. 2006), (Liu and Jiang 2011)**

The iridescence of nacreous surface is attributed to the thickness of the aragonite platelets (around 0.5μm), which is comparable to the wavelength of visible light, resulting in constructive and destructive interference. The variation of the gap separating the two platelets can be an even or an odd multiple of λ/2, where λ is the

wavelength of incident light. In the case that it is even the light waves interfere constructively, while in the case that it is an odd multiple the waves cancel each other. Thus, since the gap between the platelets varies slightly at different points, alternating bright and dark bands are seen. (Mann 2001),(Nudelman, Gotliv et al. 2006), (Krampitz and Graser 1988)

### Strombus shells

The strombus shells have a spiral shape and a complicate structure in order to protect themselves from rocks and debris from the waves. Their cross-lamellar structure is characterized by parallel layers of aragonite tiles arranged in a tweed pattern. It is a much more complex structure than nacre's as it is described in the following figure, where it is described macroscopically of 3 layers. The outer and the inner layer have the same orientation (first order lamellae), while the middle one is vertical to them. In the meantime, the middle layer is composed by smaller crystals being tilted at $45^{o}$ (second order lamellae), which are further comprised of smaller laths forming a third order lamellae.

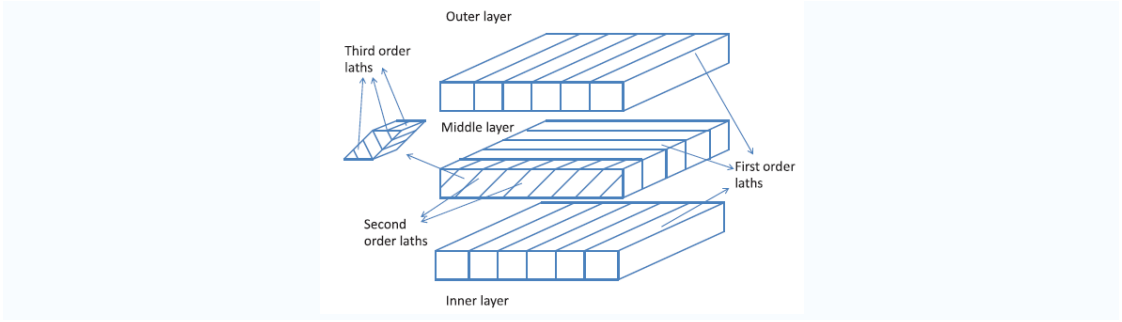


**Figure 2. Cross-lamellar structure of strombus shell (Karambelas, Santhanam et al. 2013)**

This pattern has been found to describe the architecture of Florence Brunelleschi's duomo, whose bricks are arranged in a tessellated array having the same structure arrangements and analogy of dimensions as the tiles in conches (Marc A. Meyers 2006) and it is being mimicked for the production of ceramics in order to minimize building distortions (Karambelas, Santhanam et al. 2013).

### Sea spicules

The protruding rods (spicules) of sponges have been extensively studied for their excellent flexural toughness as well as their optical properties, distributing light in the deep sea. They are made of amorphous silica layers arranged in a concentric structure like the onion skin, between of which silicatein is contained. Some species of spicules resemble optical fibers in a way that their inner layers have a high refractive index (high-index core) while the outer layers exhibit a lower refractive index, like the cladding of optical fibers. Their unique structure gives them high flexural strength where a crack progresses steadily and not at once like for the commercial communication fibers.

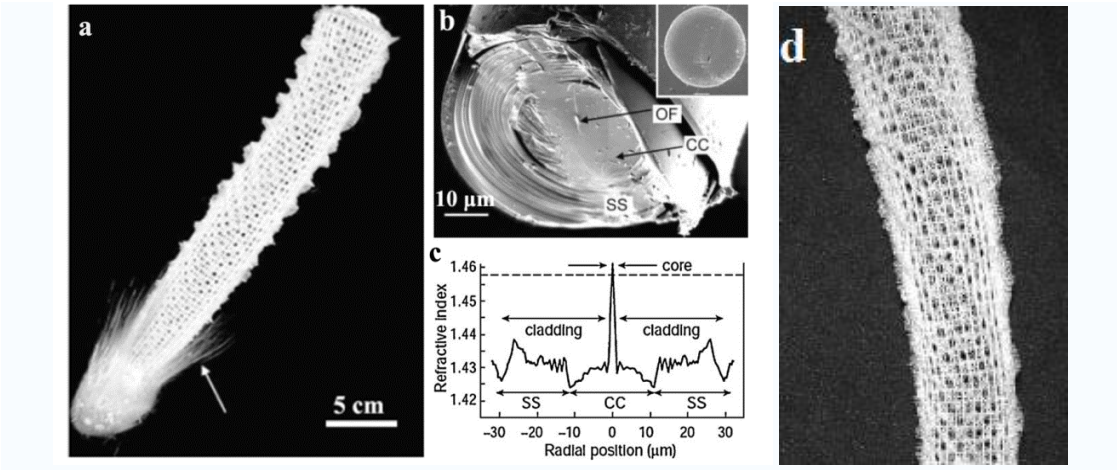


**Figure 3. (a) The glass sponge, (b) fraction of a sea sponge spicule consisting of: OF, organic filament; SS, outer striated shell; CC, central cylinder and (c) the refractive-index profile, where the dashed line indicates the refractive index of vitreous silica, (d) a closer look of showing the lattice-like skeleton (Aizenberg, Sundar et al. 2004)**

The arrangement of the fibers of these sea spicules run diagonally in both directions inside alternate squares in the lattice, inspired civil and mechanical engineers for the construction of very famous high-tech architectural buildings like the Swiss Tower in London, Hotel De Las Artes in Barcelona and the Eiffel Tower in Paris. (Marc A. Meyers 2006),(Espinosa, Rim et al. 2009),(Nudelman, Gotliv et al. 2006), (Luz and Mano 2009),(Liu and Jiang 2011),(Lakes 1993)

### 2.4 Calcium phosphate – hydroxyapatite

Bone and teeth are made of calcium phosphate and a large number of proteins. Calcium phosphate is more commonly found in the form of hydroxyapatite (HAP). Enamel, being the hardest material in vertebrates, is almost entirely inorganic in composition, while bone has relatively high organic composition.

Apatite is a calcium phosphate mineral with the chemical formula $A_4B_6(MO_4)6X_2$, where A and B are both calcium, $MO_4$ is a phosphate group, and X is a hydroxide ion. Hydroxyapatite is the mineral found in bones, teeth and fish scales and its chemical formula is $Ca_5(PO_4)_3(OH)$, where the molar ratio of Ca/P according to X-ray diffraction patterns is 1.67. Nevertheless, this ratio in biomineralized tissues can vary significantly from this value due to imperfections that may occur in the body because the organism tries to maintain homeostasis regulating calcium, magnesium, and phosphate ions.

**Table 1. Calcium phosphate salts at ambient temperatures and aqueous solutions (Koutsopoulos 2002)**

| Molecular Type | Ca/P Ratio | Name |
|---|---|---|
| $Ca(H_2PO_4)_2 \cdot H_2O$ | 0.50 | Monohydrate calcium phosphate (MCPH) |
| $Ca(H_2PO_4)_2$ | 0.50 | Monocalcium phosphate (MCP) |
| $Ca(HPO_4) \cdot 2\ H_2O$ | 1.00 | Dicalcium phosphate dihydrate (DCPD) |
| α- and β- $Ca_3(PO_4)_2$ | 1.50 | Tricalcium phosphate (TCP) |
| $Ca_4H(PO_4)_3 \cdot 2.5\ H_2O$ | 1.33 | Octacalcium phosphate (OCP) |
| $Ca_5(PO_4)_3(OH)$ | 1.67 | Hydroxyapatite (HAP) |

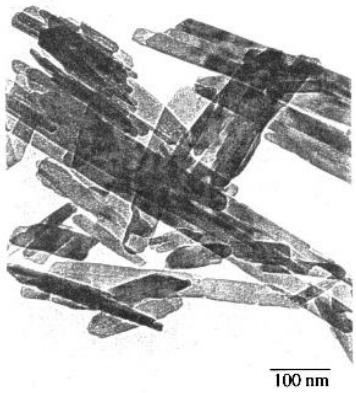


**Figure 4. Transmission electron microscopy pictures of HAP crystals. (Koutsopoulos 2002)**

While all the other calcium phosphates form a plate-like crystal morphology, hydroxyapatite forms needle–like hexagonal crystals, which increase their size mainly in length (c axis) but also in width and thickness (a and b axis). The crystal growth is being regulated through proteins.

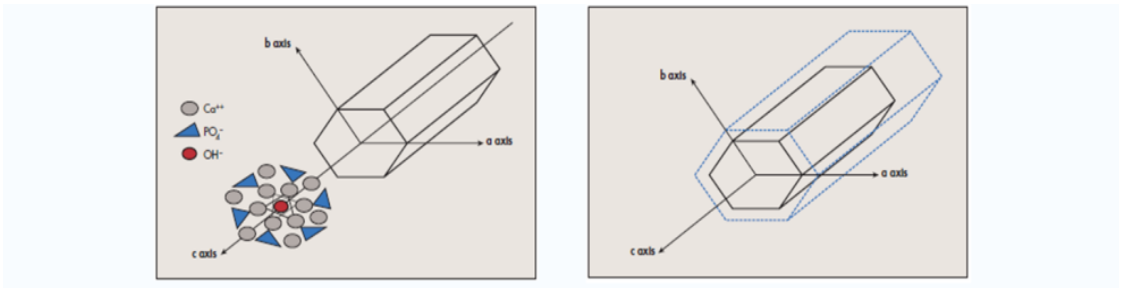


**Figure 5. (left) Schematic illustration of hydroxyapatite crystal unit cell, (right) growth of the crystal increasing their size mostly in length. (n 2007)**

Nowadays many prosthetic materials in bone tissue engineering are made of calcium phosphate ceramics due to their osteophilic character, as it will be discussed later. The properties of these materials depend on their composition, the presence of trace impurities and physical characteristics such as porosity and particle size.

**Differences between biologic apatite and geologic hydroxyapatite**

Geological hydroxyapatite, as referred before, has a molar ratio Ca/P 1.67, while bone and tooth Ca/P ratio is non-stoichiometric since they are made of a highly disordered apatite, of small crystal size, high degree of carbonate, OH deficiency, presence of

lattice vacancies, and increased solubility. On the other hand, geological hydroxyapatite incorporates inclusions along the long period of time it needs to form. Bone and dentin mineral usually can switch from a poorly crystalline apatite to a higher crystallinity mineral, to a more organized structure. Moreover bone mineral is always remodeled (resorbed and redeposited) keeping a dynamic state, while geologic hydroxylapatite is modified only by physicochemical processes (dissolution, reprecipitation, and incorporation of foreign ions). However, enamel is not remodeled at all, but degrades forming dental cavities. (Mann 2001), (Palmer, Newcomb et al. 2008), (Dalas and Koutsoukos 1989),(Boskey 2007)

### 2.5 Organic matrix

Proteins, phospholipids and polysaccharides constitute the organic matrix. These macromolecules are mainly hydrophobic in order to act as an insoluble mechanical support. The organic matrix is equally important as the inorganic for the overall mechanical properties of the bone, for example while the bone's strength tension is 130MPa, by removing the organic part it drops to 6MPa.

Two kind of macromolecules constitute the organic matrix: the framework and the acidic macromolecules. Collagen, chitin and cellulose belong to the framework macromolecules. Acidic macromolecules usually contain aspartic and glutamic acid residues, as well as serine and threonine modified with covalently bound phosphate groups. In some cases the acidic macromolecules can be also phospholipids as well as glycoproteins (proteins covalently linked with polysacchyride side chains), often containing sulfate and carboxylic acid. Both collagen and noncollagenous proteins regulate the extent to which the calcium phosphate crystals can expand, while cells affect the maturation of the crystals. (Boskey), (Mann 2001), (Collier and Messersmith 2001)

**Table 2. Main types of macromolecules associated with organic matrix-mediated biomineralization (Mann 2001)**

| System | Framework macromolecules | Acidic macromolecules |
|---|---|---|
| Bone and dentine | Collagen | Glycoproteins<br>Osteopontin<br>Osteonectin<br>Proteoglycans<br>Chondroitin sulfate<br>Keratin sulfate<br>Gla-containing proteins<br>Osteocalcin |
| Tooth enamel | Amelogenin | Glycoproteins<br>Enamelins |
| Mollusc shells (nacre) | $\beta$-Chitin<br>Silk-like proteins (MSI 60)<br>N16/N14?<br>Lustrin A | Glycoproteins<br>Nacrein<br>N66 |
| Crab cuticle | $\alpha$-Chitin | Glycoproteins |
| Diatom shells | Frustulins | Glycoproteins<br>HEP200<br>Silaffins |
| Silica Sponges | Silicatein | No data |
| Plant silica | Cellulose | Proteins<br>Carbohydrates (xylose, glucose) |

**Mineral nucleation on the organic matrix**

In biomineralization process mineral nucleation is promoted by the organic matrix. Macromolecules having negative charge, nucleate the positive ions of calcium which in turn will nucleate the phosphate anions $HPO_4^{2-}$. The activation energy of mineral nucleation ($\Delta G^*_{N(2)}$) in the presence of an organic surface (curve 2) is expected to be significantly reduced in comparison to the activation energy needed in the absence of organic matrix (curve 1) as it can be seen in the following figure. r is the size of the critical cluster needed for nucleation, which is smaller where organic matrix is present:

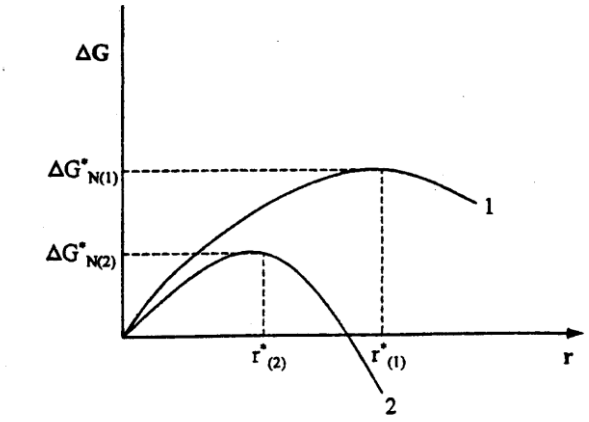


**Figure 6. Free energy of biomineral nucleation where curve 2 refers to the case of presence of an organic matrix, while curve 1 in the absence of organic matrix. (Mann 2001)**

## 2.6 Introduction to Bone

Bone, being the support of the body, is a strong, highly vascularized tissue. It consists of an organic framework in which mineral particles are dispersed. In particular, around 70%, consists of minerals and 30% organics, of which 95% is collagen, and the rest 5% non-collagenous proteins (glycoproteins, proteoglycans, and sialoproteins).

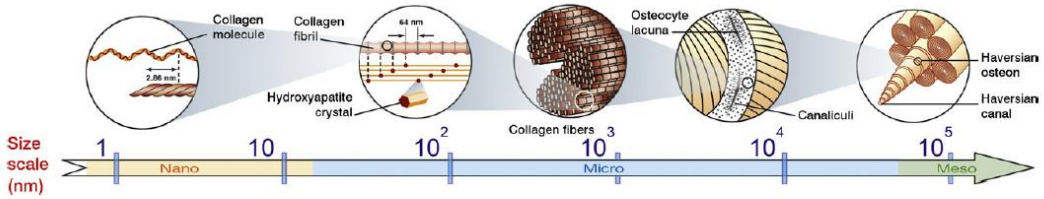


**Figure 7. Hierachical structure in human compact bone. The macro-scale arrangements of bones are either compact/cortical or spongy/cancellous.** (Lakes 1993), (Saiz, Zimmermann et al.)

Bone is strong but not brittle, rigid but flexible, lightweight but solid, mechanically strong but porous, and stable but capable of remodeling. Due to these contradictive properties the bone's structural hierarchy will be analyzed.

Two types of bone are being distinguished according to their morphology and their function: compact/cortical, which is the dense material found at the surface of all bones and spongy/cancellous, that looks like foam. Their structural difference is

depicted in the following figure and will be discussed in the following paragraph. Their difference in function is that while the cortical bone provides mechanical functions, the cancellous is involved mostly in maintaining calcium homeostasis of bone matrix. This difference lies on the kind of cells involved in the mineralized matrix. Cortical bone's main cellular component is osteocyte (mature osteoblast) that can synthesize bone as well as help between cell communication through signal transmission over long distances by extending their fillopodia between canals to reach other osteocytes. Cancellous bone on the other hand is covered by osteoblasts, which help in bone tissue formation by secreting components from the extracellular matrix.

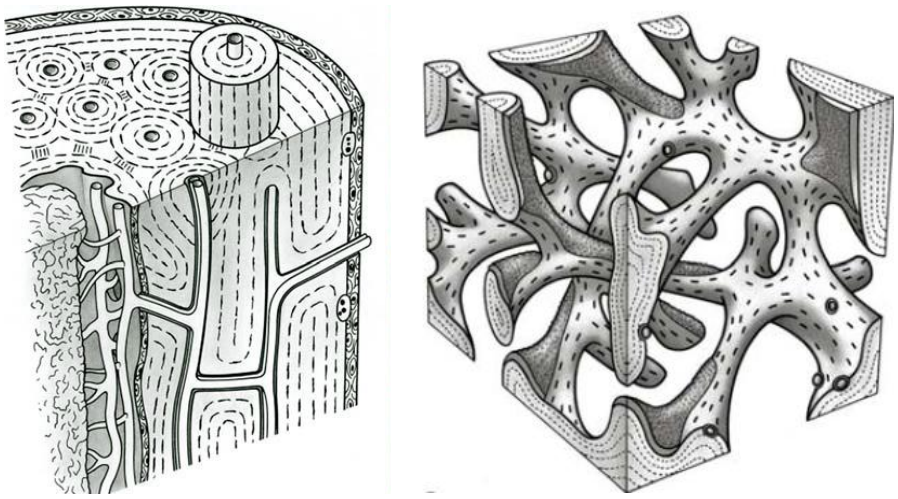

**Figure 8. Schematic structure of cortical (left) and cancellous bone (right) (Meyer 2006)**

(Mann 2001), (Palmer, Newcomb et al. 2008), (Wenk and Heidelbach 1999)

### 2.6.1 Structural hierarchy in bone

Mann (Mann 2001) as well as Weiner and Wagner (Wagner 1998) have identified a model of discrete levels of hierarchical organization in bone. According to the model, the mineralized collagen fiber is the primary building block for subsequent higher order architectures.

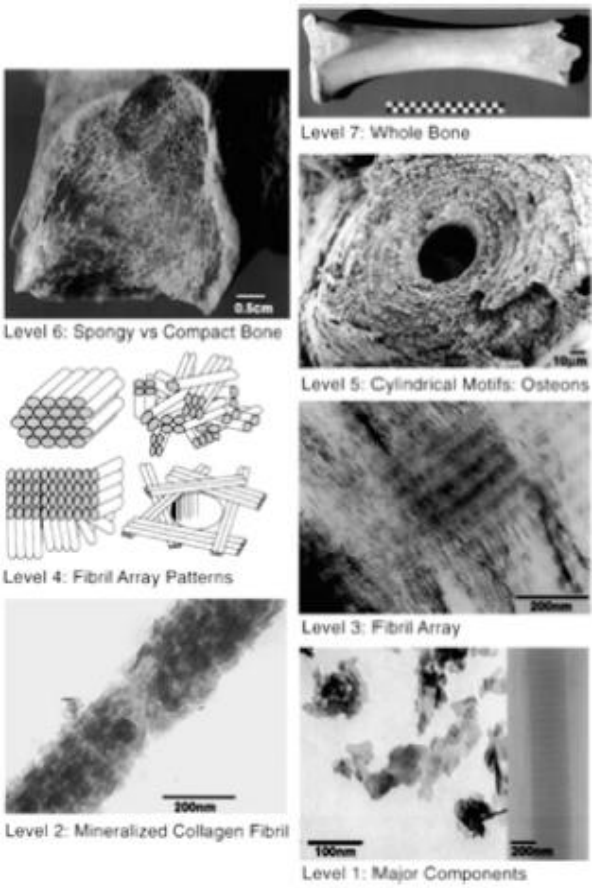


**Figure 9. Structural hierarchy in bone (Palmer, Newcomb et al. 2008), (Wagner 1998)**

As described by the above figure there are six discreet levels of bone structural hierarchy. At the first level in an aqueous environment there are collagenous and non-collagenous protein fibrils and hydroxyapatite crystals. At the second level collagen fibrils are getting mineralized, where the plate-like hydroxyapatite crystals are organized in parallel with their c-axis aligned with the long axis of the fibril. At level three the mineralized collagen fibrils are getting arranged in bundles and at fourth array patterns are formed (parallel arrays, woven arrangements, plywood-like structures or radial arrays). At the fifth level osteocytes, osteoblasts and collagen assemble in a concentric way (lamellae) and several of these bunches make up the osteon. In the middle of the osteon there is a hollow channel left where nerves and blood will pass through to supply the cells. Thus, at level six bone tissue is classified as either cancelous or cortical and finally, at the seventh level of bone organization the whole bone is formed. There are 206 different types of bone in human and each of them is defined during the formation of the embryo. (Palmer, Newcomb et al. 2008), (Wagner 1998)

### 2.6.2 Bone mineralization

**Collagen and Non-collagenous proteins**

Bone matrix is formed by macromolecules making a framework consisting mostly of collagen fibrils. Collagen type I, being the most dominant, is produced by osteoblasts. Its fiber starts to assemble inside the cell, proceeding extracellularly following specific steps: the polypeptide chains of collagen are synthesized in the cell, they self-assemble to form triple-stranded helix filaments and they secrete into the extracellular space. Outside the cell the collagen fibrils self-assemble and form cross-links being ready to biomineralize.

Non-collagenous proteins play the most important role for biomineralization. There are two basic categories: the acidic glycoproteins (where the most commonly found are bone osteocalcin, sialoprotein, sialoprotein II, osteonectin, and phosphoproteins) and the proteoglycans. The acidic glycoproteins are enriched in aspartic acid, glutamic acid (anionic residues) and phosphoserine. The proteoglycans are acidic polysaccharides, which contain even more carboxylic acids and sulfate groups. The more hydrophobic part of these proteins are adsorbed on a framework scaffold formed by hydrophobic macromolecules, like collagen type I, adopting a β-sheet conformation, leaving the acidic residues pointing towards the solution where calcium ions will nucleate.

Concluding, in the biomineralization process collagen acts as a framework used for mechanical support and for organization of the acidic proteins which are the ones who actually nucleate minerals above the collagen scaffold.

(Addadi and Weiner 1985), (Mann 2001; Palmer, Newcomb et al. 2008), (Meyer 2006)

### 2.6.3 Bone cells

Bone cells are being distinguished into two categories: the osteoclasts that resorb bone and the osteoblast family where osteoblasts, lining cells and osteocytes belong.

Osteoclasts are responsible for bone resorption (osteoid and minerals) by secretion of acids and enzymes that degrade the bone. They have many nucleus because they are formed from fusion of two or more cells. They come from bone marrow and they are related to white cells. The process of resorption initiates on the surface of the bone where underneath the osteoclast cell acidic environment is produced dissolving the mineral content. Afterwards enzymes released from osteoclasts remove the collagenous matrix. After finishing bone resorption they undergo apoptosis, where the cell disintegrates.

Osteoblasts are differentiated mesenchymal stem cells of the bone marrow. They are mononucleate cells found on the surface of bone and are responsible for producing the proteins that will form the organic matrix as well as for controlling the mineralization of bone. After bone resorption osteoblasts move into the resorbed place and start to produce osteoid, an organic matrix of collagenous and non-collagenous proteins, like

osteocalcin, osteopontin, and osteonectin. Collagen, being the most abundant, makes the scaffold where calcium and phosphate begin to crystallize. This process following bone resorption is called bone remodelling. There is also bone modelling where osteoblasts start bone formation without the action of osteoclasts for increasing bone mass to maintain bone strength. After a specific age the activity of osteoblasts compared with osteoclasts is being decreased resulting in loss in bone mass. Osteoblasts secrete factors to communicate with osteoclasts. RANK-ligand is a cytokine produced from osteoblasts that binds to RANK, a membrane protein receptor on the surface of osteoclasts. When these two proteins connect to each other the activation, differentiation and survival of osteoclasts is triggered. In this stage and in order to balance bone resorption osteoblasts secrete osteoprotegerin (OPG) which binds to RANK-ligand to prevent the interaction with RANK receptors. Hormones regulate the secretion of OPG and RANK-ligand.

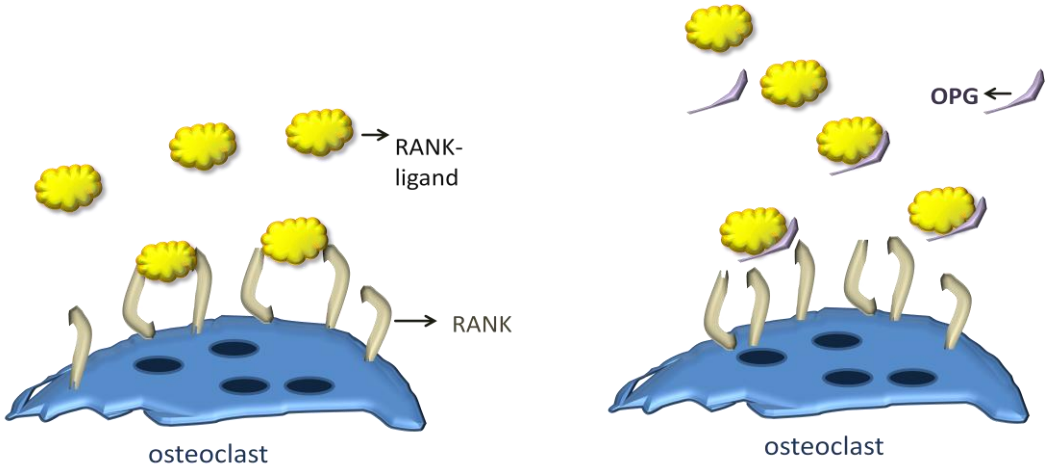


**Figure 10. (left) interaction of RANK-ligand and its receptor RANK leading to increased bone resorption, (right) with the secretion of OPG from osteoblasts the interaction of RANK-ligand and RANK is prevented**

When osteoblasts finish the bone formation they can follow three options: apoptosis, differentiation into osteocytes or to become flat lining the surface of bone, turning into lining cells.

Osteocytes are mature osteoblasts. They are long-branched cells located inside the bone that they sense mechanical strains on the bone. They synthesize sclerostin, a protein inhibitor for bone formation. Sclerostin binds on the surface of osteoblasts on receptors that regulate bone mass. When sclerostin binds on these receptors signaling is inhibited and thus osteoblastic activity gets reduced. When osteocytes sense major mechanical stress they transmit the signal to each other through their branches and they produce less sclerostin.

Bone cells produce growth factors and cytokines in order to communicate with other cells. The growth factor bone morphogenetic protein (BMP) is being produced in the bone marrow and binds to the receptors found on the mesenchymal cells to differentiate them into osteoblasts. This happens through a mechanism where after the connection of BMP with its receptor BMPR (on the surface of the mesenchymal cell) the cell produces the factor Cbfa1 which activates the DNA and thus osteocalcin is

being produced that differentiates the cell into osteoblast. This is happening with the help of SMADS, which are intracellular proteins that transduce the extracellular signals from the BMPRs to the nucleus where they activate gene transcription.

Another growth factor received by osteoblasts is insulin-like growth factor (IGF) produced by osteoclasts. IGF causes osteoblasts cell division and differentiation.

Cytokines are also molecules produced in cells for cell signaling, that can cause proliferation and differentiation of osteoblasts. Other functions that they have is to bind to bone marrow stem cells and differentiate them into osteoclasts and to inhibit osteoblasts apoptosis. Another important cytokine described previously is RANK-ligand.

(Meyer 2006), (D'Ippolito, Schiller et al. 1999)

### 2.7 Introduction to tooth and Structural hierarchy

The tooth of mammals proceeding from the outer to the inner layer consists of the enamel, the dentin, the pulp, and the cementum. Enamel, is the hardest substance of the body of vertebrates and this occurs due to the formation of interweaving crystals of hydroxyapatite, which is the 95% of enamel by weight and less than 1% of it is the organic material. It is formed with the help of amelogenin and enamelin, that with time they get removed. Enamel's high amount of mineral makes it susceptible to fracture. Dentin can prevent this fracture by absorbing stresses of the enamel due to the fact that contains more collagen, making it more similar to the bone. The pulp contains nerves and vessels, while the cementum is the connective tissue surrounding the tooth root where it connects to the jawbone through a fibrous connective tissue, the periodontal ligament.

Odontogenesis starts to occur during the first weeks of embryo in utero. In the future mandible of the embryo, the oral epithelium cells grow toward the layer of mesenchymal cells of the mandible forming the dental lamina, a condensed connective tissue. Ameloblasts secrete amelogenin protein. Ameloblasts induce adjacent cells to become odontoblasts. Odontoblasts start to move away from the ameloblast layer leaving behind enamel. Mineralization deposition starts with the deposition of hydroxyapatite in both enamel and dentin. Each of the ameloblasts produces one crystalline rod.

Odontoblasts form root dentin and then disintegrate allowing the surrounding cells to become cementoblats, which align next to dentin and will calcify forming the cementum. Tooth eruption starts after the first month of birth.

(Boskey 2007), (Palmer, Newcomb et al. 2008)

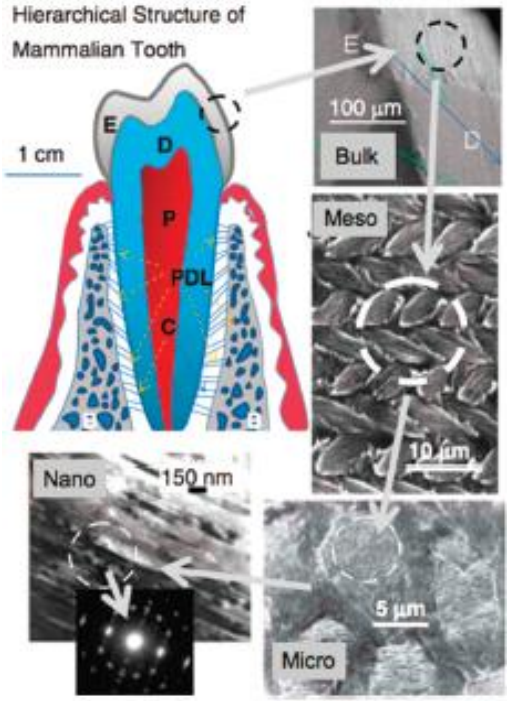


**Figure 11. Hierarchical architecture of mammalian enamel. Enamel (E) is the outer layer of the crown, beneath is dentin (D), the pulp (P) and the cementum (C) connecting to the jawbone through the periodontal ligament (PLD). The bulk image depicts the enamel organ, the transition across the dentino-enamel junction, and the dentin below. On the mesoscale level, the prismatic enamel can be seen consisting of interweaving rods. In the micrometer scale the composition of a single rod is depicted and at the nanometer scale highly organized array of hydroxyapatite crystallites are aligned along the c-axis.** (Palmer, Newcomb et al. 2008)

### 2.8 Epitaxy - Structural matching

The phenomenon epitaxy refers to matrix-mediated biomineralization. It is the structural matching between two different phases and it is mostly observed in the geological deposits, where the minerals of the substrate differ in structure and chemical composition to that of the overgrowth, but there is a common crystallographic orientation of these two phases. In epitaxial structural matching the interfacial energy of ion nucleation on an organic surface is being reduced.

The results of X-ray electron diffraction patterns of nacre surface are used from Mann (Mann 2001) to describe a model for structural matching, showing that the acidic amino acids of the proteins guide the nucleated crystal arrangement. In the figure that follows the a and b axes of the antiparallel β–pleated sheet of the matrix are aligned with the a and b crystallographic directions of the aragonite lattice. More specifically, the axis of the aragonite crystal (4.96 Å) is matching very well to the distance between two β-sheet strands (4.75 Å). Though, it is not the same happening for the b crystallographic plane (7.97 Å), which is different from the b axes of the β-sheet 6.9 Å). Over longer distances this distance difference can be lessened.

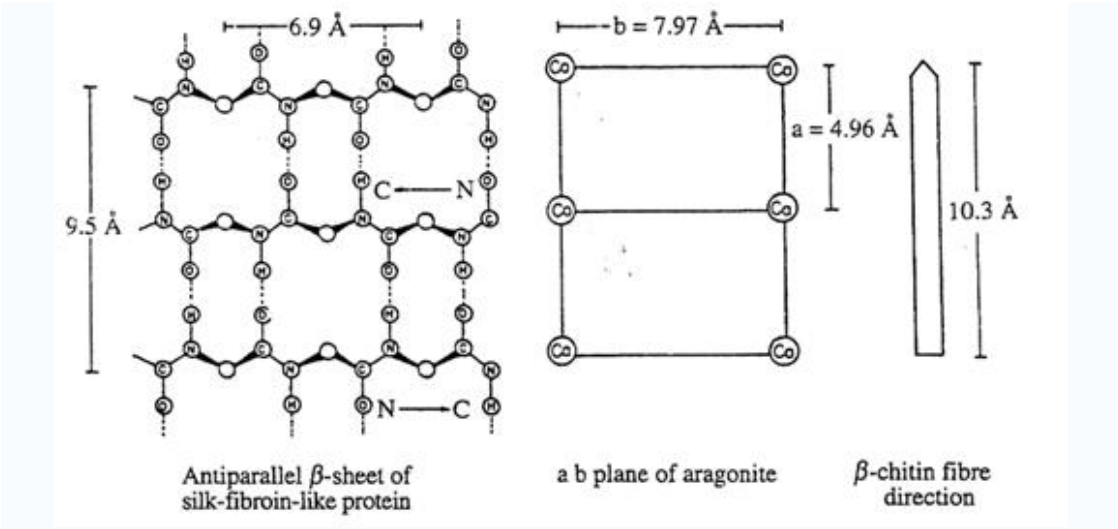


**Figure 12. Structural model for the geometric matching of shell nacre, where the length of an antiparallel β-sheet of the silk-fibroin-like protein (9.5 Å) and of the β-chitin fiber (10.3 Å) is very similar to the double a plane (9.92 Å) of the aragonite unit cell. (Mann 2001)**

It is found in nature that one $Ca^{2+}$ needs two aspartate ligants to balance the electrostatic interactions, and more specifically to alternate every second residue in the polypeptide chain (Weiner and Hood 1975). As it can be seen also at the figure below, if the acidic protein is arranged such that the repeated domains of aspartic acid in it (Asp) and a neutral amino acid (X) adopt a β–sheet conformation, then there is a strong correlation between the spacings of the carboxylate groups and the theoretical lattice arrangement of $Ca^{2+}$ in the (001) surface of the aragonite. According to the following figure one calcium ion can either get nucleated between the two aspartic ligands of the same strand (6.9 Å), or between aspartic acids of the anti-parallel strands (9 Å). It can be noted that in the latter case a parallel conformation would be more favorable because the interstrand distance between two aspartic acids is smaller.

(Mann 2001), (Addadi and Weiner 1992)

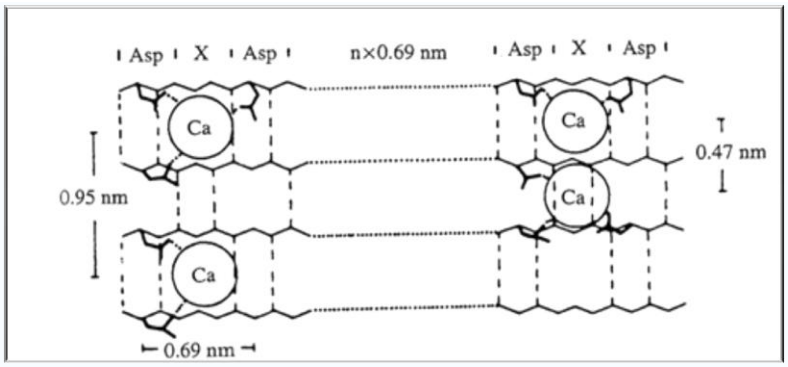


**Figure 13. Asp-X domains of an antiparallel β–pleated sheet and $Ca^{2+}$ binding in shell nacre (Mann 2001)**

# 3 Bone Tissue Engineering

## 3.1 The concept of tissue engineering

Tissue engineering is a rapidly expanding field of applied biology, biomedical engineering and nanotechnology, where therapies are implemented for the reparation or replacement of damaged tissues or organs. The need for biological materials of complex hierarchical patterns, for the reparation or substitution, introduced the use of biomimetic approaches of tissue engineering. Generally, there are three main approaches to tissue engineering: a) the use of isolated cells, b) the use of acellular biomaterials for induction of tissue regeneration, and c) the combination of both cells and materials. Each one of these approaches can be enhanced by in vitro microenvironmental factors before the use of the tissue substitute.

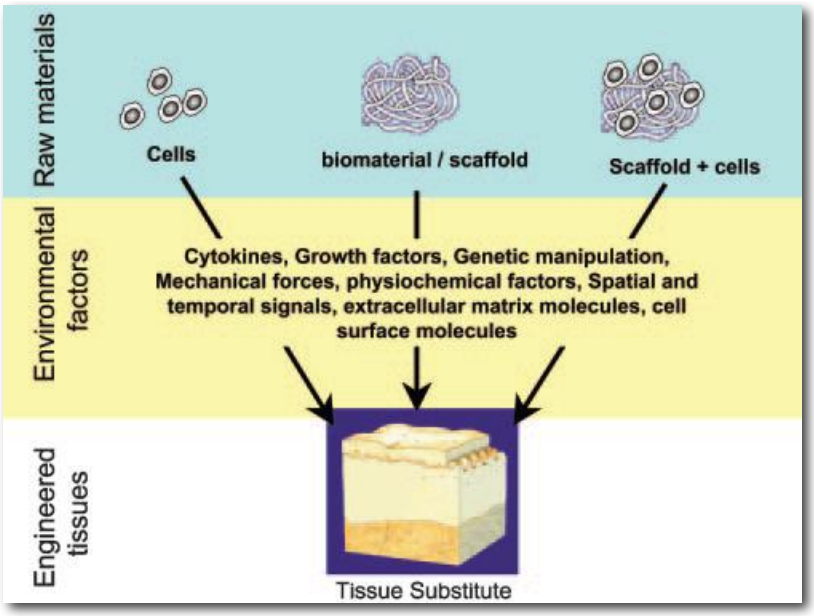


**Figure 14. Tissue engineering approaches. Tissue engineering approaches are classified into three categories: a) cells alone, b) cells with scaffolds, and c) scaffolds alone (Khademhosseini, Langer et al. 2006)**

Cells used for tissue engineering may come from cell lines from patients themselves (autogenous), from donors (allogenic), from a genetically identical donor (syngenic) and from animal sources (xenogenic). After the harvesting, the tissues are dissociated and placed in cell culture. There proliferation starts and after acquiring the right number of cells they are seeded on a scaffold, and cultured in vitro in a bioreactor or incubator. When the construct is matured enough, then it can be implanted in the area of defect in patient's body. Commercial examples of allografts are Infuse® Bone Graft, which is a collagen carrier sponge with bone morphogenetic protein 2 (BMP2) for the treatment of degenerative disc disease, and Trinity® Evolution™, a cancellous bone allograft containing viable adult stem cells, osteoprogenitor cells and a demineralized bone component, for the treatment of musculoskeletal defects.

Applications of tissue engineering allografts include ectodermal, endodermal and mesodermal derived tissues. In ectodermal tissues the nervous system, the cornea and skin epidermis are involved, while in endodermal the liver, pancreas and tubular

structures like bladder, ureter and kidney. In the mesoderm connective tissue, muscle, bone, and circulatory systems develop.

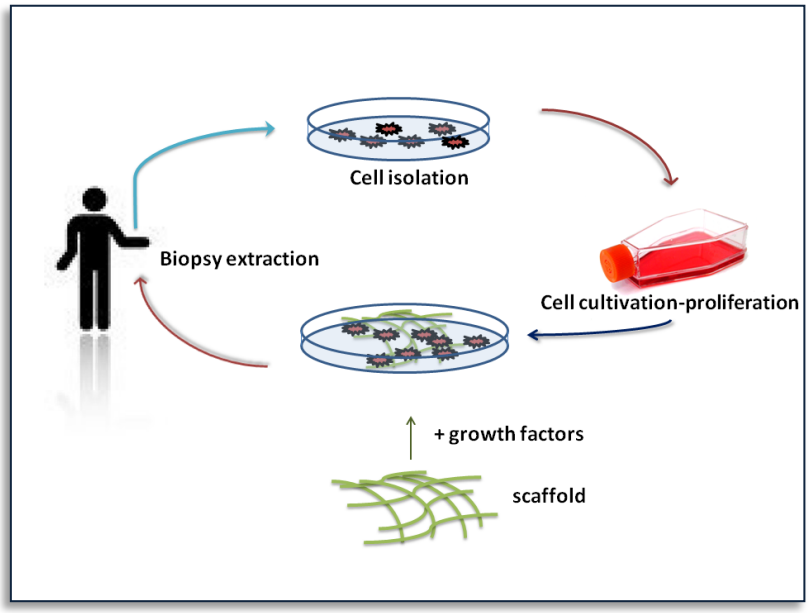


**Figure 15. The concept of tissue engineering** (RR. 2002), (Robert Lanza 2007), (Khan, Yaszemski et al. 2008), (Khademhosseini, Langer et al. 2006).

### 3.2 Bone tissue engineering

The approach of allograft bone repair has limitations, such as cost, variability in osteogenic capacity, and lot-to-lot variability. Although autogenous grafts are ideal for osteogenesis, there cannot be enough autogenous bone available, plus the fact that a second surgery to acquire the autograft is needed and harvesting increases patient's morbidity. On the other hand allogenic, syngenic and xenogenic tissues increase the fear of immunogenic rejection and disease transmission. Bone tissue engineering is the research field that aims to address these issues by applying the principles of chemistry, biology, and engineering. Being a dynamic process it initiates with recruitment of osteoprogenitor cells which proliferate, differentiate and eventually form a matrix that bone remodeling will follow.

In modern bone tissue engineering cells from the patient's own tissue are seeded onto a three-dimensional scaffold, allowing the bone to develop, and therefore eliminating traditional organ transplant problems such as donor shortage and immune system rejection. Bone formation is being aided by biomolecules to control osteogenesis, bone regeneration and extracellular matrix formation. Some of these biomolecules are the bone morphogenetic protein (BMP), transforming growth factor-b (TGF-b), insulin-like growth factor (IGF), fibroblast growth factor (FGF) and Vascular endothelial growth factor (VEGF) for inducing angiogenesis.

Since the presence of osteoblasts provides direct osteogenesis and the presence of growth factors permits osteoinduction, there is a need for investigation of alternatives

to allograft bone with the exploration of novel biomaterials. (Hutmacher 2000), (Nasr, Aichelmann-Reidy et al. 1999), (Robert Lanza 2007), (Bose, Roy et al. 2012).

### 3.3 Biomaterials

Since biomaterials are important in tissue engineering for their interaction with biomolecules, cells and tissues serving as mechanical scaffolds, they should meet some basic requirements:

1. their building blocks should be derived from biological sources
2. they should be osteoconductive and osteoinductive
3. their interconnective porosity should be more than 100μm for diffusion of nutrients and oxygen
4. they should be able to form blood vessels (angiogenesis)
5. their mechanical properties should match host bone properties
6. the scaffold production, purification, and processing should be reproducible
7. they should be economically affordable
8. they should be amenable to design and modification
9. they should not cause cytotoxicity or inflammation
10. they should be bioresorbable

(Gelain, Horii et al. 2007),(Bose, Roy et al. 2012)

Biomaterials can be either biologic or synthetic. Synthetic biomaterials can be metals, ceramics, composites and polymers. A typical dental composite used is Bis-GMA (Bis- Glycidyl methacrylate), which is photopolymerized after the application in the tooth cavity and contains barium or silica inclusions. Its optical properties are satisfying, but its thermal expansion and contraction behaviour is not enough satisfactory. Another problem is that dental composites are less stiff than enamel, since they cannot contain such a high amount of inorganic material that will impede the location of the paste to the cavity. (Park and Lakes 1992; 2007)

Homopolymers used in medicine include PMMA, PolyHEMA, PP, PE, PVC, PDMS. Between the co-polymers polylacticoglycolic-lactic acid (PLGA) is the most popular biodegradable used because it degrades to biochemical moieties. Its rigid mechanical properties and bulk degradation kinetics turned the interest towards synthetic polyesters, such as PGS (poly(glycerol sebacate)), that degrade to naturally occurring monomers. A commonly used biodegradable ester is polycaprolactone. It is slowly degraded by hydrolysis of its ester linkages in physiological conditions being an interesting option for the preparation of long term implantable devices (instead of the fast degradation rate of polylactide). A major disadvantage is that degradation of polymers such as Polylactic acid (PLA) and Polyglycolide acid (PGA) creates local acidic environment that can have adverse tissue responses. (Bernhard O. Palsson 2004),(Buddy D. Ratner 2004)

Bioactive ceramics have excellent biocompatibility and dexterity towards bone bonding. They support enzyme activity, vascularization and induction of differentiation of mesenchymal cells to osteoblasts. In 45S5 bioglass the dissolution

products can control osteogenesis and production of growth factors. Bioactive glasses though have low mechanical strength, especially in the porous form. Another disadvantage is that crystallization can render them bioinert.
Calcium phosphate based ceramic scaffolds are widely used in bone tissue engineering because they are totally biocompatible, osteoconductive and osteoinductive. Hydroxyapatite is the most popular scaffolding material in this group. However, their relatively poor biodegradability, their lack of strength and their high toughness impede their application in bone engineering.
Biologically derived materials can be natural, such as extracellular matrix which is harvested from allografts and xenografts and provides mechanical integrity and influences cell function (Benders, Weeren et al. 2013). Another kind of biologically derived materials are purified natural proteins and polysaccharites. Proteins like silk, fibrin, elastin, actin and collagen are mostly used as biomaterials. Collagen I provides the mechanical properties in ligaments, tendons and cartilage, while collagen II allows cartilage to entrap the proteoglycan aggregate as well as provide tensile strength to the tissue. These purified natural proteins can form water-swollen hydrogel matrices with unique 3D architecture, used to imitate the biochemical ambient of an extracellular matrix. However, the limited control over their physical properties and biodegradability impedes extensive use of these proteins.

The last category of biomaterials refers to self-assembling peptides. The discovery of a peptide category that spontaneously undergoes self-organization into well-ordered structures, such as fibrils, tapes and ribbons, opened a new avenue for molecular fabrication of biological materials. Short peptides have been invented with broad applications, including 3D tissue cell culture, reparative and regenerative medicine, tissue engineering, slow drug release and medical devices. An example of peptides used as biomaterials is amphiphilic oligopeptides, being synthesized in-vitro that self-assemble into beta-sheet scaffolds. These peptides have two distinctive sides, the hydrophobic side forms a double sheet inside of a fiber and the hydrophilic side forms the outside part that interacts with water molecules, forming an extremely high water content hydrogel. This kind of peptides can form 3D scaffolds to be used in 3D cell tissue cultures (Hauser and Zhang 2010).

## 4. Self-Assembly and Amyloid Fibers

Self-assembly is the way in which simple building blocks (atoms, molecules, colloids, micelles, etc) recognize and associate with each other spontaneously to form macroscopic objects with ordered and stable nano-scale order.
In the molecular level, it is the spontaneous organization of molecules under thermodynamic equilibrium conditions into structurally well-defined and stable arrangements through a number of noncovalent interactions (Whitesides et al., 1991; Lehn). The bonds taking part in these interactions are hydrogen bonds, ionic bonds and van der Waals' bonds (Zhang 2002).

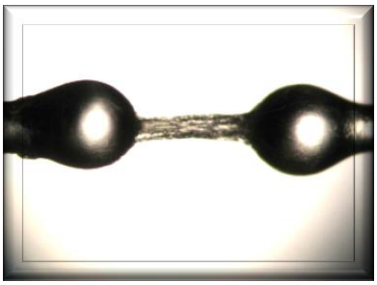

**Figure 16. Aligned self-assembled fibers between glass rods**

Molecular self-assembly is a new route to produce novel materials using peptides, phospholipid and DNA as building blocks to produce potential biological materials for a wide range of applications. (Zhang 2002)

### 4.1 Amyloid fibrous assemblies

Protein aggregation is a common feature of many neurodegenerative diseases. Amyloid forming proteins are often associated with them playing a central role in pathogenesis. In this process, one molecule (monomer) of a soluble protein interacts with other monomers of the same protein to form dimers, oligomers, and polymers. With the addition of several monomers the size of the aggregates increases and they precipitate as insoluble amyloid fibrils, in which the structure is stabilized by the β-strands interacting within a β-sheet.

There is a list of 16 proteins which can form amyloid fibrils causing various diseases, including Alzheimer, Parkinson, Creutzfelt-Jakob disease. All these amyloid forming proteins vary considerably in their primary structure, function, size and tertiary structure, but they appear to form fibrils which show very few structural differences. The Aβ peptide, which is normally having a physiological role not affecting humans, in patients suffering from Alzheimer's disease this peptide forms insoluble amyloid fibrils making ordered aggregates which are deposited extracellularly as amyloid plaques in the neuropil, and as vascular deposits. (Saido 2003), (Serpell 2000)

#### 4.1.1 Characteristics of amyloid fibers

Amyloid fibrils are proteinaceous deposits having some common features. The morphology of amyloid fibrils according to electron microscopy images is straight, unbranching with several microns length and tens of angstrom in diameter.
Another common characteristic of amyloid fibers is that they stain with Congo red dye or Thioflavin T giving a green birefringence when examined under cross-polarised light. The fibrils are composed of β-strands which are perpendicular to the axis of the fibril giving a unique X-ray diffraction pattern characteristic of the β-sheet type of the fibrils. The X-ray diffraction pattern shows a strong meridional reflection at 4.8Å which corresponds to the hydrogen bonding distance between beta-strands and an equatorial reflection at 10-11Å that corresponds to the stacking distance between the beta-sheets. (Saido 2003), (Serpell 2000)

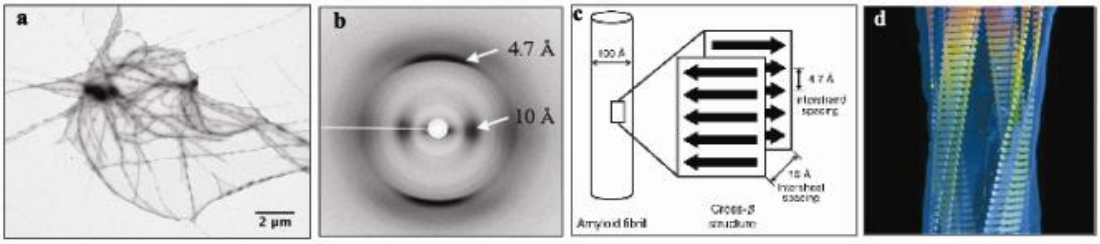


**Figure 17. Characteristics of self-assembled amyloid fibrils, a) morphology using TEM analysis, b) X-ray fiber diffraction pattern, c) Cross-beta structure and d) computational model**

Besides the diseases caused by amyloid formation, amyloid structures are also encountered in natural fibrous structures such as chrysopa egg stalks (K. D and K. M 1957) and silkmoth chorion proteins (Hamodrakas, Asher et al. 1982),(Hamodrakas, Etmektzoglou et al. 1985),(Iconomidou, Chryssikos et al. 2001), (Iconomidou 2010), (Hamodrakas 1992) attracting attention as biomaterials with remarkable mechanical and chemical properties.

### 4.2 Self-assembling peptides

The study of self assembling peptides was pioneered by Shuguang Zhang (Zhang, Holmes et al. 1993), where a 16-residue peptide [(Ala-Glu-Ala-Glu-Ala-Lys-Ala-Lys)2], a fragment of a yeast protein zuotin, having alternating hydrophilic and hydrophobic residues, where every other residue in the peptide is alanine. When salt is added, the peptide spontaneously assembles to form a macroscopic insoluble and stable membrane due to the combination of hydrophobic interactions and complementary ionic bonds between glutamic and lysine side chains. The alanines form the hydrophobic bonds and glutamic acids and lysines form complementary ionic bonds. The membrane is formed from interwoven filaments formed by peptide aggregates. Investigating the conditions that can affect the self-assembly can help the study of insoluble peptides responsible for several neurological disorders. (Zhang, Holmes et al. 1993)

Ehud Gazit's group investigated the Aβ (1-42) peptide involved in Alzheimer's disease:

D-A-E-F-R-H-D-S-G-Y-E-V-H-H-Q-K-L-V-F-F-A-E-D-V-G-S-N-K-G-A-I-I-G-L-M-V-G-G-V-V-I-A

where the aromatic interactions play a significant role in the process of amyloid fibrils formation. They discovered that the core recognition motif of the beta-amyloid polypeptide, the diphenylalanine element self-assembles into a novel class of peptide nanotubes.

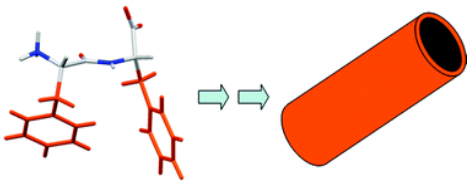

**Figure 18. Schematic illustration of the self-assembly mechanism of the diphenylalanine peptides into nanotubes (Gorbitz 2006)**

In general, the advantages of self-assembling peptides is that they can be formed under mild conditions, they are biocompatible-biodegradable, resistant to extreme conditions, they have controlled hydrophilic-hydrophobic interactions and there is a possibility of introducing site-specific changes at their sequence level. Furthermore following the 'top-down' approach structure resolution cannot arrive as low as in the 'bottom-up' approach using self-assembling peptides nanostructures, where fabrication can arrive to the nanoscale. A characteristic example is the 20 nm silver wires produced by casting metal within diphenylalanine peptide nanotubes (Reches and Gazit 2003).

### 4.3 Applications of biomolecular templates for nanowire fabrication

The wide interest for the use of biomolecules for nanowires is increasing due their following characteristics:

- biodegradability/biocompatibility
- easily formed under mild conditions
- possibility of introducing site-specific changes at the sequence level
- cost is reducing steadily

Self-assembled biomolecules, being insulators in their dry form (Waleed Shinwari, Jamal Deen et al. 2010), are not suitable for conducting electrical current. They have to get templated with inorganic compounds that act as electrical conductors.
Previous work on biomolecular templates includes DNA fibers templated with silver ions that a further electroless gold deposition, using the silver clusters as nucleation centers led to the production of DNA-templated gold nanowires (Braun, Eichen et al. 1998). Another work for templating DNA molecules with metals was based on the negatively charged phosphate groups and aromatic bases of DNA strand which could bind metallic cations electrostatically. Also the fact that various transition metal ions bind to the nitrogen atoms of the DNA bases resulted in the formation of metal–DNA complexes, which were palladium templated and exhibited ohmic behavior and indeed very close to bulk palladium's resistance (1kΩ). (Richter, Mertig et al. 2001)
Viral particles were also used for templating with cobalt oxides to make electrodes for advanced lithium batteries. The M13 virus, a filamentous bacteriophage, consists of approximately 2700 coat proteins helically wrapped around its single stranded DNA. Tetra-glutamate was fused to the N-terminus of each copy of the coat protein because glutamate's carboxylic acid, being negatively charged, interacts electrostatically with positively charged gold ions, which were connected to the cobalt oxides.
Tobacco mosaic virus (TMV) has also been used as a template for platinum cluster deposition by inserting on its surface additional cysteines that could bind covalently to the metal. (Lee SY 2006).
Collagen-like fibers have also been gold-decorated that were further metalized through electroless silver plating to achieve full coverage. The final diameter of a single metalized fiber exceeded 150nm. (Self-assembled collagen-like peptide fibers as templates for metallic Nanowires).

Another example of metal wires having small final diameters was reported by Scheibel et al. (Thomas Scheibel 2003). Self-assembling yeast prion amyloid proteins were used for the templating of metal nanowires in order to create metallic nanowires and measure their ohmic conductivity. The yeast protein was genetically engineered to contain a cysteine residue accessible on its surface that could bind colloidal gold particles covalently. The fiber metallization process used included initial covalent adhesion of colloidal gold nanoparticles to the fiber's cysteine residues. The following step included silver ion enhancement and finally the silver coated fibers were further enhanced with gold nanoparticles. They exhibited ohmic conductivity with low resistance ($R$ = 86 Ω).

After the several metallization step processes of the fibers, they had a final diameter of 100nm. The drawbacks being encountered of all the attempts to template biomolecule are more or less common. Some of them are: the instability of large molecules, the fact that there are not frequent binding sites, the metal particles are not attached effectively, several step processes (eg silver enhancement) in order to increase the fiber diameter.

Ehud Gazit's group focused also on applications by creating peptides of minor changes to the original building block in order to endow the structure with different functionalities. For creating metal nanowires the original building block used was diphenylalanine, a very short peptide fragment which is the core recognition motif of Alzheimer's β-amyloid polypeptide. It was proven that it can be used as a mold for casting metallic silver inside the peptide by reduction of ionic silver within the formed nanotubes, followed by enzymatic degradation of the peptide backbone, which resulted in the production of silver nanowires with dimensions of ~20nm. (Reches and Gazit 2003)

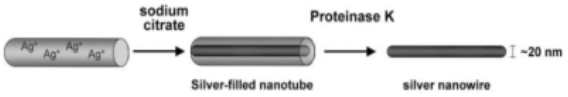


**Figure 19. Silver nanowire fabrication from the diphenylalanine peptide nanotubes (Reches and Gazit 2003)**

Moving one step further, they introduced a thiol linker peptide on the peptide nanotube surface, in order to be templated inside with silver nanoparticles and outside with gold nanoparticles that were attached to the thiol groups. The purpose was to make a devise of meta-insulator-metal coaxial nanocables, that can give rise to unique electromagnetic properties. (Carny, Shalev et al. 2006)

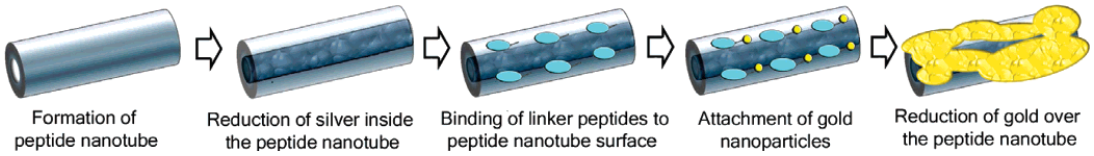


**Figure 20. Model for fabricating a trilayered (silver-peptide-gold) nanowire (Carny, Shalev et al. 2006)**

Another major disadvantage of the process was the positioning on the electrodes, as it can be seen in the following figure. (Thomas Scheibel 2003). It is quite difficult in measuring the electrical properties of a single nanowire, and after voltage increase the conducting nanowires were vaporized.

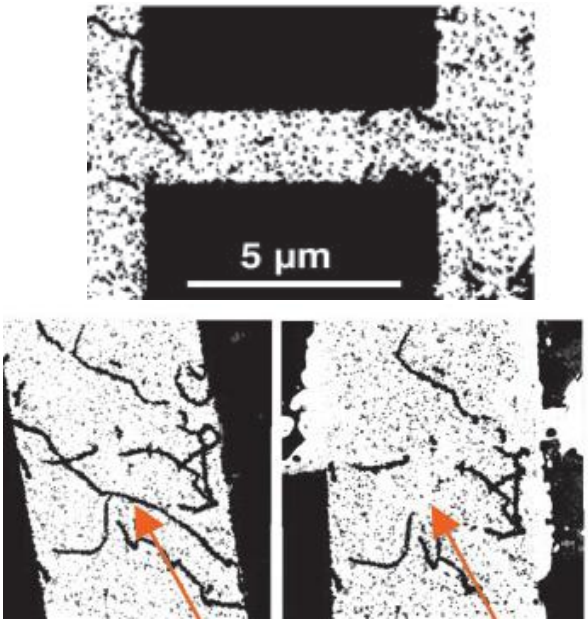


**Figure 21. Gold- and gold toned fibers randomly deposited on patterned electrodes for measuring ohmic conductivity. (Left ) Gold nanowires that did not bridge the gap between two electrodes. After inreasing the voltage the conducting nanowires were vaporized. Before (middle) and after (Right) conductivity measurement (Thomas Scheibel 2003)**

In the previous study paragraph peptide sequences that have the ability to self-assemble were metalized with gold, silver and platinum nanoparticles. Furthermore they will be oriented on 3D organic-inorganic hybrid structures forming bridges between them.

According to Scheibel et al (Thomas Scheibel 2003) self assembled amyloid fibrils were metalized but they encountered a difficulty in measuring their conductivity, due to failure of the fibrils to bridge the gap between two electrodes. This problem could be confronted by taking the following challenges:

- Positioning
- Controlled assembly

### 4.4 The adenovirus

The adenovirus fibers have been studied as model systems of self-assembly. Adenoviruses are double-stranded DNA viruses without a membrane envelope, infecting mammals and birds. They form icosahedral particles, with a trimeric fibre at each of the 12 vertices, which has an N-terminal domain attaching the viral capsid, a central shaft, and a C-terminal domain that binds to the cell receptor. Inside the capsid they include the double-stranded DNA genome. Extracellular proteins like the

adenovirus fiber are extensively studied due to their ability to survive in harsh environments, thus being extremely resistant to proteases, denaturants like urea, temperature, and detergents. (Retsos, Papanikolopoulou et al. 2005)

The human adenovirus fiber trimer consists of 582 residues per monomer, where the head domain causes the trimerization. In the shaft there is a repeating sequence motif with hydrophobic amino acids alternating with hydrophilic amino acids and glycine (G) or proline (P) hold conserved positions. The basic repeat fold contains a beta-strand, which is almost parallel to the axis of the fiber, followed by a beta turn and another beta strand, tilted at $45^{o}$ relative to the fiber axis. Hydrogen bonds are established between the strand-loop-strand motif, which can be considered as the basic building unit at the structural level (van Raaij and Mitraki 2004), (van Raaij, Mitraki et al. 1999).

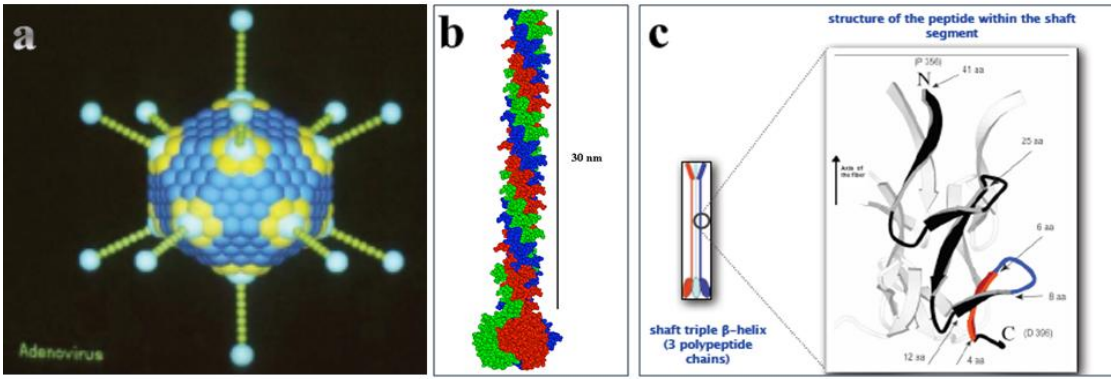


**Figure 22. a) The adenovirus capsid, b) model containing the triple beta helix motif of the adenovirus fiber shaft. It contains residues 321–582 of chains (the different colours symbolize the three polypeptide chains), c) structure of the peptides within the native shaft segment (residue numbers correspond to positions in the full-length fiber sequence). One of the strands of the trimeric shaft is shown in black and the other two in gray. The head domain starts after residue 396. The first amino acid residue of each peptide is shown with arrows. The 41- and 25-amino acid peptides include the last four amino acids (residues 393 to 395, NKND), whereas the 12-, 8-, and 6-aa peptides stop at residue 392 (van Raaij, Mitraki et al. 1999; Papanikolopoulou, Schoehn et al. 2005)**

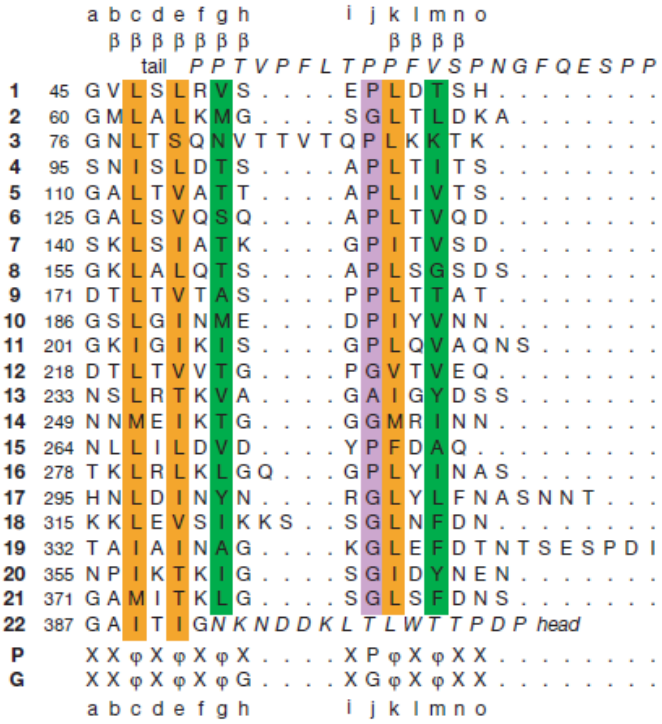

**Figure 23. The shaft sequence (van Raaij and Mitraki 1999)**

Papanikolopoulou et al. (2005) studied the folding of the adenovirus fiber shaft when peptides lack the head part of the shaft. The peptides studied (41-, 25-, 12-, 8-, and 6-aa peptides) correspond to specific repetitive sequences from the adenovirus fiber shaft and form amyloid fibrils (Papanikolopoulou, Schoehn et al. 2005). The peptide studied mostly by Kasotakis et.al. is the octapeptide N-S-G-A-I-T-I-G (residues 385-392, Asparagine- Serine-Glycine-Alanine-Isoleucine-Threonine-Isoleucine-Glycine), which involves a loop and a β-strand and it self-assembles into amyloid-type fibrils with dimensions of 10nm in width and some microns in length. With the help of Molecular Dynamics Simulations (MDS) the conformations of the 3 stranded peptide sheets can be observed in the following figure.

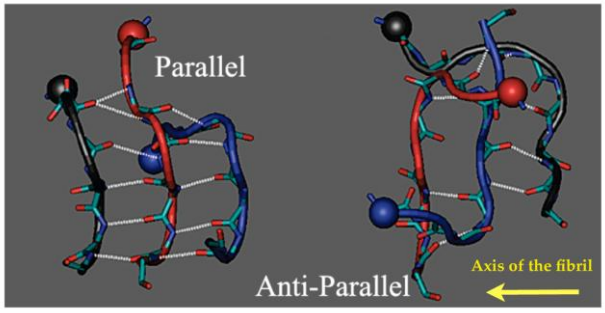


**Figure 24. Parallel (left) and antiparallel (right) conformation of the 3 stranded peptide sheets. Hydrogen bonds are shown in white dashed lines. (Tamamis, Kasotakis et al. 2009)**

In the present thesis templating of peptides with inorganic molecules (metal nanoparticles and calcium phosphate) will be described as well as the sol-gel method

utilized for producing an interconnected, rigid network from a colloid where the dominating interactions are short-range forces, such as Van der Waals and surface charges. The materials designed will be used as scaffolds for tissue regeneration. A major challenge is the combination of the bottom-up and top-down approach using the self-assembly process and multiphoton polymerization technique with short-pulse lasers respectively.

## B. HYBRID MATERIAL PROCESSES

### 1. Scaffold fabrication techniques

For scaffold fabrication there are several techniques being used, using heat, adhesives, molding fabrication and light. The most commonly used techniques are being described below.

Techniques using heat involve the application of heat energy to fuse layers of material to each other by raising the glass transition temperature. One of them is Selective Laser Sintering (SLS), which is a technology that uses a laser beam to raise the local surface temperature, causing fusion of the powder beds of a polymer into desired shapes. The disadvantages of this technique is that the material must be in a powder form, high temperature is needed, and in the final processed material there is a powdery surface finish.

Fused deposition modeling (FDM) is also a heat-based manufacturing technique, where a three-dimensional scaffold is being formed while molten plastics or ceramics are extruded through a nozzle depositing layer by layer. The range of materials used is limited by the melting points and processing conditions involved. Another limitation is that this method allows high control in the xy plane, but not in the z-direction due to the fact that the height of the pores is predetermined by the size of the polymer filament that is coming out from the nozzle. Concluding, materials used for heat-based fabrication techniques are limited in synthetic polymers that can withstand high temperatures.

Another approach for scaffold fabrication is using solvents or adhesives instead of heat to bind polymers eliminating biomaterial limitations such as temperature. Three-dimensional printing (3DP) is an example where a binder solution is deposited onto a biomaterial powder bed using an ink jet printer. The fabricated 3D structures have microposity, but low mechanical strength, there are limits of scaffold architecture, the surface finish is powdery, and thus it might require post processing. Pressure assisted microsyringe (PAM) fabrication technique also involves layer by layer deposition with the solvent acting as a binding agent, where the deposition of polymer dissolved in solvent is made through a syringe fitted with a 10–20 μm glass capillary needle. The limitation of this method is that the micropores cannot be incorporated using particulate leaching due to the syringe dimensions.

Molding is an indirect fabrication method for scaffolds. Prototypes as molds are being used that were for example previously fabricated using stereolithography or three-dimensional ink-jet printing by depositing wax or other low melting point compounds which can be removed by melting and washing with solvents. The limitation of this technique is the great number of steps involved until the fabrication of the final product. Replica molding is a lithographic technique, where elastomeric stamps are used fabricated from patterned silicon wafers. Originally such scaffolds are fabricated from poly(dimethylsiloxane) (PDMS), a transparent, biocompatible elastomer. It allows duplication of three-dimensional topologies in a single step enabling highly

complex structures in the master to be duplicated into multiple copies replication of sub-10nm features. The limitation of this method lies on the difficulty to obtain reproducibly over large areas because of lateral collapse of the features in the polymeric replica.

The most modern method having the highest accuracy for the production of 3D structures involves the use of light energy to initiate a chain reaction, resulting in the solidification or polymeric chain break of polymer which is initially added in a liquid form (photopolymerization). There are also cases that polymeric chain break occurs in a polymer when irradiated with light, depending on the photosensitive material used each time. Stereolithography refers to this manufacturing technology that uses laser UV light to polymerize a photosensitive material.

(Liu Tsang and Bhatia 2004; Yeong, Chua et al. 2004; Khademhosseini, Langer et al. 2006)

## 2. Stereolithography

The growth of computer memories, allowing the design of three-dimensional models which can be rotated and visualized slicing the model, in combination with the invention of lasers and methods for accurately guiding the focused beam, resulted in the growth of a new sector in rapid construction of models, prototypes or manufactured parts within few working hours, fully automatically using a powerful computer, a flexible fabrication system and some after-treatment techniques.

Commercial rapid prototyping machines have a fabrication precision of several millimeters not being able to satisfy the modern requirements for device multifunctionalization and miniaturization that demand sub-micron feature size. The emergence of a new technology in 1997, two-photon photopolymerization (2PP), has introduced light curable resins into the new field of nanofabrication. Thus, during the last few years a vast need raised for rapid progresses in high-performance ultraviolet curable systems with increasing requirements of monomers and oligomers, active photoinitiators, and efficient photosensitizers.

(Maruo, Nakamura et al. 1997; Sun and Kawata 2005) , (Fouassier), (Steen 2003)

### 2.1 Stereolithography with Femtosecond Lasers

Stereolithography is the manufacturing technology for producing three-dimensional solid objects from CAD patterns by the exposure of a photopolymerizable resin in a laser beam. Its inventor, Charles W. Hull, (US Patent 4,575,330, entitled "Apparatus for Production of Three-Dimensional Objects by Stereolithography") defined stereolithography as a method and apparatus for making solid objects by successively "printing" thin layers of the curable material, one on top of the other.

The lasers used as an irradiation source range from extreme UV (XUV) to NIR wavelengths, operating at continuous wave (CW) to pulsed mode at nanosecond (ns), picosecond (ps) and femtosecond (fs) widths. 3D patterns are created using either multi-beam interference or direct laser writing. (Sun and Kawata 2005)

## 2.2 Photopolymerization - Multi-Photon polymerization technique

When light interacts with matter, the matter responds in a proportionate way, where the optical effects are considered to be linear. The effects of reflection, refraction, scattering and absorption, all of which occur at the same frequency, the frequency of the light are not altered by the process. Nowadays many electro-optic devices of practical importance depend upon nonlinear optical effects, including two-photon absorption (TPA).

When the resins used so far for fabrication got exposed to UV lasers, following the single-photon photopolymerization process, the resulting precision was greater than 10 mm. In 1997 a new technology for high precision three-dimensional nanofabrication emerged, two-photon photopolymerization (Maruo, Nakamura et al. 1997), where non-linear processes were taking place. Three-dimensional micrometer structures with sub-100nm resolution can be fabricated. When focusing tightly a beam of an ultra-fast infrared (IR) laser into the volume of a photosensitive material, the polymerization process can be initiated by non-linear absorption within the focal volume. By moving the laser focus three-dimensionally through the resin, 3D structures can be fabricated. The photosensitive materials used include a variety of acrylate (Maruo, Nakamura et al. 1997), (Satoshi Kawata 2001), and epoxy (Markus Deubel 2004) materials. Several components and devices have been fabricated such as photonic crystals, mechanical devices, plasmonic structures (Kiyan, Reinhardt et al. 2007), (Reinhardt, Passinger et al. 2006), biomolecule scaffolds (Claeyssens, Hasan et al. 2009), and microscopic models (Sun, Tanaka et al. 2001), (Steen 2003), (Sun and Kawata 2005), (Fouassier), (Haske, Chen et al. 2007),(Lee, Yang et al. 2006)

In photopolymerization unsaturated molecules being in the liquid state can convert to solid macromolecules through polymerization reactions using light (UV, visible to IR range). Upon light excitation, the monomers or oligomers get solidified by polymerization and cross-linking reactions. During the polymerization a chain reaction produces macromolecules, while in cross-linking there is formation of crosslinks with chemical bonds. The first and most important step in photopolymerization is photoinitiation, where small low-weight molecules sensitive to light irradiation (photoinitiators) are added. Each photoinitiator, which usually absorbs one UV photon, absorbs two near-IR photons at the same time and becomes a radical when the spatial density of the near-IR photons is high. The resultant radicals cut the double bonds of carbons in the acrylyl groups contained in the monomers and oligomers and successively create new radicals at the ends of the monomers and oligomers. The radical combines with other monomers and thus, the process becomes a chain reaction until a radical meets another radical, where the reaction terminates.

The speed of the above reaction in the case of the two-photon absorption is proportional to the square of the photon density at each position in the resin, while in the case of single-photon absorption it is proportional to the density itself.

*Photoinitiation* :

$$I \xrightarrow{h\nu} I^* \rightarrow R\cdot$$

*Chain − propagation* :

$$R\cdot + M \rightarrow RM\cdot \xrightarrow{M} RMM\cdot \cdots \rightarrow RM_n\cdot$$

*Termination* :

$$RM_n\cdot + RM_m\cdot \rightarrow RM_{m+n}R$$

$$RM_n\cdot + RM_m\cdot \rightarrow RM_n + RM_m$$

In many cases the energy collection is accomblished with the sensitizer, a molecule absorbing light that transferrs it to the photoinitiator:

$$S \xrightarrow{h\nu} S^* \cdots \xrightarrow{I} I^* \rightarrow R\cdot$$

where S is the photosensitizer, I the photoinitiator, R the radical and M the monomer S* and I* are the excited states of the photosensitizer and photoinitiator respectively after absorbing the photon energy. (Maruo, Nakamura et al. 1997; Lee, Yang et al. 2006)

### 2.3 **The mechanism of Two-Photon Absorption**

The distinction between two-photon polymerization (2PP) and common stereolithography is that in case of 2PP, near-infrared (IR) laser pulses are used for polymerizing the photosensitive materials, while in the case of conventional stereolithography ultraviolet (UV) laser radiation is being used.

The photosensitive materials that polymerize under UV (λ) exposure can undergo similar reactions when two photons (2λ) are absorbed simultaneously (two-photon photopolymerization), only if the light intensity is large enough. 2PP polymerization can occur using IR laser pulses within the volume of the material since photosensitive materials are usually transparent in the IR region and are highly absorptive in the UV range. Thus, high resolution 3D structures can be fabricated, whereas with UV laser radiation, due to single photon absorption, polymerization also occurs at the surface of the material.

Two-photon absorption can occur either by stepwise/sequential absorption, or by simultaneous absorption. Stepwise absorption doesn't require coherence of the incident light, and may be considered as two sequential single photon absorptions. The absorbing species are excited to a real intermediate energy state. This first excited state becomes populated by the first absorbed photon and has a well-defined lifetime, this state then absorbs a second photon. The presence of this intermediate state means that the material absorbs at this specific wavelength, making the absorption a surface effect.

In the case of simultaneous two-photon absorption mechanism there is no real intermediate state, but a virtual intermediate state is created by the interaction of the absorbing species with the first photon. If the second photon arrives within the virtual state lifetime, which is in the pico/femtosecond range, then can it be absorbed. Each of the two photons has half the energy of the energy gap between the two levels. Ti: sapphire lasers are widely used for inducing TPA because they produce ultrahigh peak power with a very short pulse width in the picoseconds and femtosecond regime.

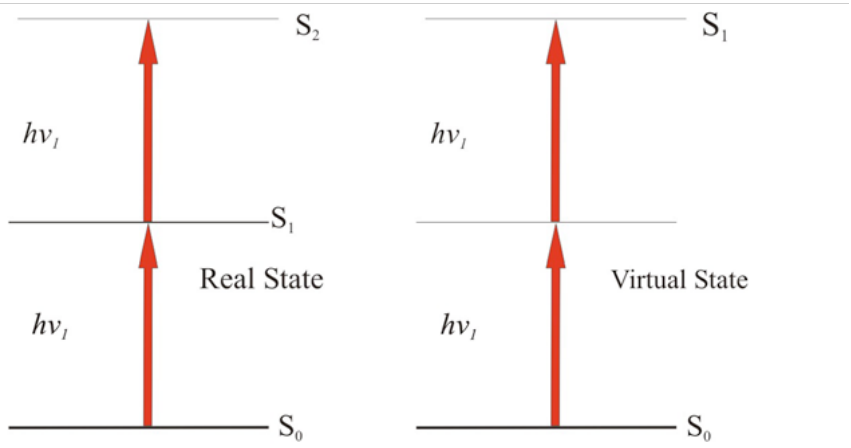


**Figure 25. (left) stepwise TPA with an actual intermediate energy level, and (right) simultaneous TPA with a virtual energy level (Maria Farsari 2010)**

The intensity distribution of the laser beam, assumed to be Gaussian, can be expressed with the following relation:

$$I(r_0,0) = I_0 \exp(-2r_0^2/\omega_0^2)$$

where $r_0$ is the radius of the beam, $I_0$ its intensity at the central axis in the focus plane, and $\omega_0$ the radius of the focused beam spot. (Ovsianikov, Passinger et al. 2007),(Sun and Kawata 2005),(Steen 2003),(Maria Farsari 2010)

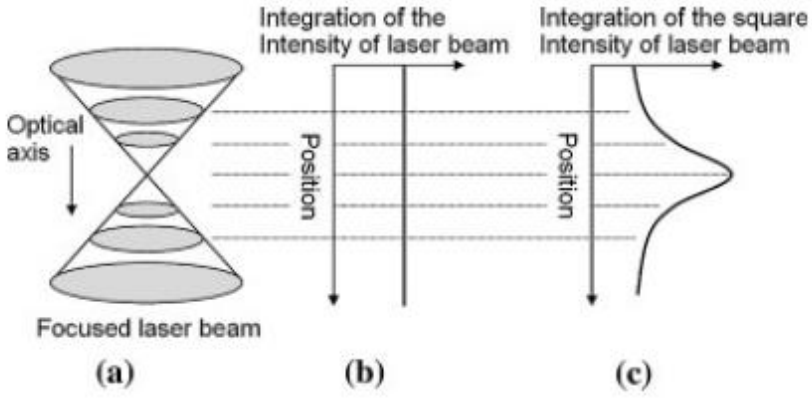


**Figure 26. Comparison of TPA with single-photon absorption generated: (a) schematic diagram of a focused laser beam; (b) single-photon absorption per transverse plane; (c) two-photon absorption per transverse plane, calculated by integrating the square intensity over the plane with respect to the optical axis (Lee, Yang et al. 2006)**

### 2.4 The diffraction limit

Optical diffraction of a focusing light microscope was revealed by Abbe's work on image formation. Due to the non-linearity of multi-photon polymerization technique, ultra short pulsed lasers can overcome the diffraction limit and produce sub-wavelength resolution 3D structures.

Besides the importance of the material and laser characteristics for achieving high resolution, the laser wavelength and the numerical aperture (N.A.) of the focusing objective used can define the resolution limit according to Abbe's diffraction limit:

$$\mathbf{cd}=\frac{\mathbf{k1\lambda}}{\sqrt{qNA}}, \boldsymbol{dof} = \frac{\mathbf{k2n\lambda}}{\sqrt{qNA^2}}$$

where cd is the critical dimension of the printed structure, dof is the depth of focus, $\lambda$ the wavelength of the laser, q the order of the multiphoton process, $k_1$ and $k_2$ are factors depending on the photostructurable material and n is the immersion oil refractive index.

N.A.= n•sinθ ~ *r*/*f* , where n is the refractive index of the medium (which is 1.0 for air and up to 1.56 for immersion oils), θ is the half-angle of the maximum cone of light that can enter or exit the lens, r is the radius of the lens and f is the focal length.

To produce 3D structures with in-volume patterning and lower resolution than that can be defined by the diffraction limit, materials with well defined photopolymerization threshold need to be used.

### 2.5 Advantages of MPP

Two-photon polymerization technique compared with other micro/nanofabrication schemes has the following unique advantages:

- the intrinsic ability to produce 3D structures due to the long wavelength chosen for TPA, which has less peripheral absorption and less scattering, giving rise to the deep penetration of light
- the use of ultrashort pulses can start intense nonlinear processes at relatively low average power, without thermally damaging the material
- it is compatible with many photosensitive resins, which are widely available and may be obtained at low cost
- the system is easy to operate and maintain
- immediacy of the technique where no mask, mold, or stamp is needed for fabrication. It directly converts computer- designed patterns into matter structure, where if needed the design can be quickly iterated and modified
- while even the most conventional stereolithographic fabrication techniques require the use of vacuum condition for operation as well as clean room facilities, where the energy consumption of clean room facilities may run as high as 10,200 $kW/m^2$, MPP can be performed in conventional facilities, like in clinical environment (e.g., an outpatient medical office) for fabrication of patient-specific drug delivery devices. (Sun and Kawata 2005; Shaun D. Gittard 2010)

### 2.6 Materials for MPP

The materials used for conventional lithographic applications are negative and positive photoresists. When negative photoresists get exposed to multi-photon or UV light, there is a direct writing of the structures in the sample. The polymer chains get cross-linked, making the exposed area insoluble to the solvent used to remove the unpolymerized material. The opposite result occurs in the case of positive photoresists, where multi-photon absorption causes the polymeric chains to break and thus the irradiated regions get dissolved to the development solvent.

The negative tone photoresists are subdivided to epoxy and acrylate based photoresists. The most well-known commercial materials are the epoxy based SU-8 and ORMOCER®. ORMOCER® is an organic-inorganic hybrid polymer in a liquid form, which combines properties of organic polymers (toughness, functionalization, and processing at low temperatures) with those of glassy materials (hardness, chemical and thermal stability, and transparency). It finds applications from magnification lenses to dentistry.

The positive photoresists are chosen instead of negative photoresists for the simplicity of making structures by fabricating their replicas. Examples of these materials are the AZ and S1800.

All of the above commercial photosensitive materials suffer shrinkage distortion, the fabricated structures cannot arrive to very high resolution, and they lack the ability for 'fine tuning' of their properties for specific applications. Thus, the need rose for a new technique for fabrication of photosensitive materials with tuned properties.

(Maria Farsari 2010), (Ovsianikov, Passinger et al. 2007)

## 3. Hybrid materials

### 3.1 The Sol-Gel method

Sol-gel process is a versatile solution process for making advanced materials, including ceramics and organic-inorganic hybrids. In general, the sol-gel process involves the transition of a solution system from a liquid "sol" (mostly colloidal) into a solid "gel" phase. The advantages of the sol-gel processing against other traditional glass melting or ceramic powder methods is the potentially higher purity and homogeneity and the lower processing temperatures.

With sol-gel processing the surfaces and interfaces of materials during the earliest stages of production can be controlled. The chemical variability can be limited and controlled by the production of uniquely homogeneous structures or producing extremely fine-scale second phases achieving long-term reliability of a material. By combining inorganic and organic materials with this method, unique physical properties can be achieved.

Colloid is called the suspension of dispersed nanoparticles, of which the gravitational forces are negligible and interactions occurring are by short-range forces, such as Van der Waals and surface charges. A sol is a colloidal suspension of solid particles in a

liquid and can be used to generate polymers or particles from which ceramic materials can be made. Other colloidal suspensions that can be used for generating polymers are the aerosol, which is a colloidal suspension of particles in a gas and the emulsion, a suspension of liquid droplets in another liquid. A ceramic is a nonmetallic and inorganic material. In the sol-gel process the precursors for preparation of a colloid consist of a metal or a metalloid element surrounded by various ligands. Metal alkoxides are precursors that are most widely used in the sol-gel process, which have an organic ligand attached to a metal or metalloid atom. They are popular precursors because they react readily with water during hydrolysis.

When a molecule reaches macroscopic dimensions so that it extends throughout the solution, the substance is defined as a gel. Gel is the interconnected, solid network with pores of submicrometer dimensions and polymeric chains whose average length is greater than a micrometer. Most gels are amorphous, even after drying, but they usually crystallize when heated.

Concluding, with sol–gel technology materials can benefit from straightforward preparation, modification and processing. Photosensitive materials are usually prepared with this method and, in combination with post-processing, chemical and electrochemical inertness, good mechanical and chemical stability can be achieved. (West ; Scherer 1990)

### 3.2 Hybrid material fabrication with the sol-gel method

Silicon, being the most abundant metal in earth, can undergo in the form of silicate hydrolysis and condensation to form polysilicate gels and particles. A characteristic example in nature is the case of precious opal, which is composed of amorphous silica particles glued together by a lower-density silicate gel. Repeated hydrolysis and condensation steps involving the soluble silica lead to aqueous polysilicate species that under appropriate chemical conditions evolve into spherical particles of anhydrous $SiO_2$. The different colors observed in opal are attributed to the transparent silica spheres that are tightly packed and the spaces between them containing air or water, acting as a diffraction grating, breaking visible white light into separate colors. (Scherer 1990)

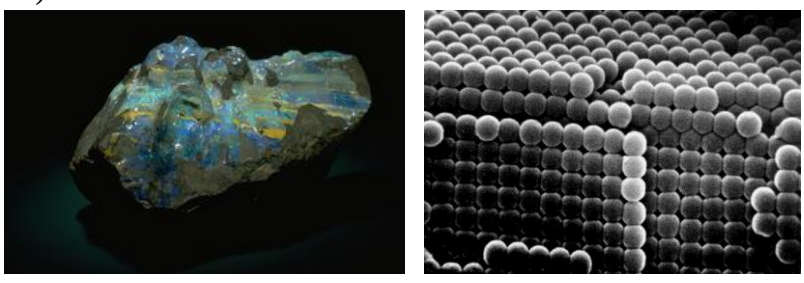

**Figure 27. Opal stone (left), Cross-sectional SEM image of a thin planar opal silica (right) (http://www.mnh.si.edu/earth), (Stewart, Chadderton et al. 2010)**

The sol-gel materials are formed through the following 4 steps:

- hydrolysis and condensation
- gelation

- aging
- drying

### 3.2.1 Hydrolysis and condensation

Transition metal oxide gels are successfully used in the sol-gel technology, with more emphasis on silicates due to their greater chemical reactivity. Silicate gels are usually synthesized by hydrolyzing monomeric, tetrafunctional alkoxide precursors employing a mineral acid (e.g. HCl) or base (e.g.$NH_3$) as a catalyst. Hydrolysis occurs by the nucleophilic attack of the oxygen contained in water on the silicon atom according to the following reaction:

hydrolysis

$$-Si-OR+\ H_2O \rightleftharpoons -Si-OH+ROH$$

esterification

Subsequent condensation reactions involving the silanol groups produce siloxane bonds plus any by-products alcohol or water. Usually it starts before hydrolysis completes:

alcohol condensation

$$-Si-OR+HO-Si- \rightleftharpoons -Si-O-Si- +ROH$$

alcoholysis

Two partially hydrolyzed molecules can link together in a condensation reaction resulting in an oxygen bridge between two metal centers (oxolation).

water condensation

$$-Si-OH+HO-Si- \rightleftharpoons -Si-O-Si- +H_2O$$

hydrolysis

Alcohol can be used as a solvent because water and alkoxysilanes are immiscible. However, gels can be prepared from silicon alcoxide-water mixtures without added solvent since the by-product of the hydrolysis reaction is alcohol and it is sufficient to homogenize the phase separated system.

### 3.2.2 Gelation

As the sol particles grow and collide to each other, a three-dimensional network of sub-micrometer particles is being formed and viscosity increases sharply. The sol becomes a gel when it can support a load elastically. The change is gradual as more and more particles become interconnected. The sharp increase in viscosity that accompanies gelation freezes in a particular polymer structure at the gel point. At this

point gelation is considered to be a rapid solidification process. This "frozen-in'' structure may change with time, depending on the temperature, solvent, and pH conditions or upon removal of solvent.

### 3.2.3 Aging

The chemical reaction that caused gelation continues long after the gel point. Polycondensation continues and reprecipitation of the gel network, which increases the thickness of interparticle necks and decreases the porosity, causing strengthening, stiffening and, inevitably, shrinkage of the formed network.

### 3.2.4 Drying

During the drying step the gel decreases in volume because of evaporation of the liquid resulting in differential shrinkage of the network and thus the formation of tensile stresses that can cause fracture. The decrease in volume is equal to the amount of liquid evaporated. As drying proceeds the network becomes increasingly stiff due to the formation of new bonds, porosity decreases and the tension in the liquid rises. Formation of concave menisci is being observed between the liquid and the solid phase till a point that the tension of the liquid cannot overcome further stiffening and the meniscus recedes into the pores leaving air-filled pores near the outside of the gel. For these reasons ageing a gel before drying helps to strengthen the network and reduce the risk of fracture. (Scherer 1990), (West)

## C. THESIS RATIONALE

The present PhD thesis focuses on the use of natural biological fibers as models for the design of novel materials and their positioning and integration into devices using femtosecond laser technologies. This approach aims at the combination of the advantages of top-down laser fabrication with the bottom-up design possibilities of the self-assembling peptides, for the development of biocompatible high-precision scaffolds with complex architectures for applications in the field of biomaterials and photonics.

More precisely, after introducing natural bottom-up processes as well as hybrid material processes, the combination of these two strategies on the 3D patterning of self-assembled peptides on hybrid structures was investigated separated into two parts: firstly the fabrication of metallized structures for biosensing and secondly the fabrication of scaffolds for hard tissue engineering.

- **Part 1: Metallized structures for biosensing**

The precise positioning of peptide-based nanostructures is an essential part of their use in technological applications. Thus, the challenges that had to be investigated were:

a. the design of novel photosensitive hybrid materials with metal-binding sites
b. the investigation over material structurability, 3D structure resolution and metallization quality
c. the positioning of self-assembled peptide fibrils and their controlled assembly
d. the integration of self-assembled peptide fibrils into microsystems.

The orientation of conductive peptide fibrils between 3D structures can be proposed for conductivity measurements of self-assembled peptide fibrils as well as could set the basis for the fabrication of a biosensor where the peptide plays both the role of the sensing and the recognition element.

- **Part 2: Scaffolds for hard tissue engineering**

The scaffold topography is crucial for cell life, where the cell shape can be affected resulting in switching from cell growth to apoptosis. Thus, the importance of 3D scaffolds with microscale features had to be investigated on their role for assisting tissue regeneration and influencing prominent cellular functions. For bone tissue engineering there is a requirement of biocompatible scaffolds that require the investigation of:

a) Biomaterials (fibrous protein supports with acidic amino acids for calcium nucleation)
b) Fabrication processes that can convey:
    - mechanical properties

- porosity
- 3D micro/nano topography

The fabrication and selection of an optimal scaffold was investigated over its mechanical properties and tested for biocompatibility with pre-osteoblastic cells.

Aiming at a novel approach to hard tissue regeneration inspired by nature based on "scaffold-on-scaffold" biofabrication, the primary 3D scaffolds were functionalized with attached secondary peptide scaffolds that could be used as a support for the directed growth of cells into biomineralized units.

Bi-functional peptide sequences (metal and calcium binding) forming amyloid fibrils were designed which would act as secondary scaffolds for the deposition of calcium phosphate, after immobilization on the primary scaffolds fabricated with DLW.

Moreover, the femtosecond laser system used for the fabrication of 3D structures was investigated over its ability to retain the bioactivity of proteins during the exposure to high laser intensities. For this purpose uniform protein micropatterns of avidin, bovine serum albumin (BSA) and biotinylated bovine serum albumin were fabricated by varying the system's power and scanning speed as well as the material's concentration. The photocrosslinked microscale protein topographies can be used for the guidance and the precise control of cellular architectures.

## D. EXPERIMENTAL PART

### 1. TECHNIQUES

#### 1.1 Transmission electron microscopy (TEM)

Transmission electron microscopes (TEM) operate on the same basic principles as the optical microscopes but instead of photons (light rays) it uses electrons making it possible to get a resolution a thousand times better than with a light microscope. TEMs consist of an electron source, a thermionic gun, an electron beam, electromagnetic lenses, a vacuum chamber, condensers, a sample stage, and the results are visualized on a phosphor or fluorescent screen.

The electrons are generated through thermionic emission from a tungsten filament and they are accelerated by using high voltage. The electromagnetic lenses focus the electrons into a very thin beam. Depending on the density of the material under observation, some of the electrons are scattered and disappear. The unscattered electrons arrive on a fluorescent screen, displaying the different parts of the specimen in varied darkness according to their density. The image can be studied directly by the operator or photographed with a camera. The resolution that can be achieved is up to 0.1 nm at magnifications of 50 million times.

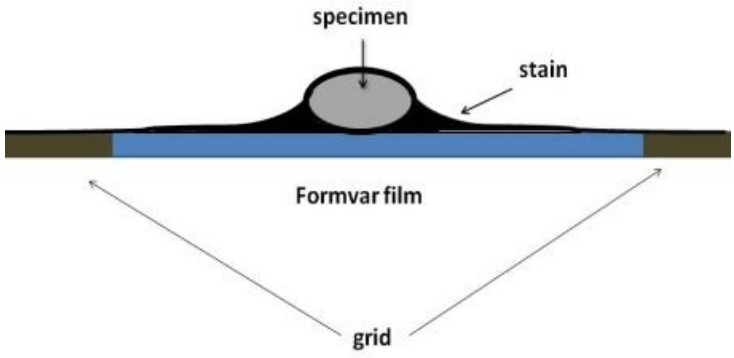


**Figure 28. Negative staining for TEM observation**

The samples are placed on a copper or nickel grid covered with a thin film of formvar membrane in order to keep the sample on its surface. The grid has 300 areas of observation of approximately 60x60 μm area. The biological samples, being transparent, need to be stained negatively in order to improve the contrast. The staining method needs a heavy metal solution such as uranyl acetate embedded on the grid with the sample, which is deposited around the molecule and provides contrast for better visualization.

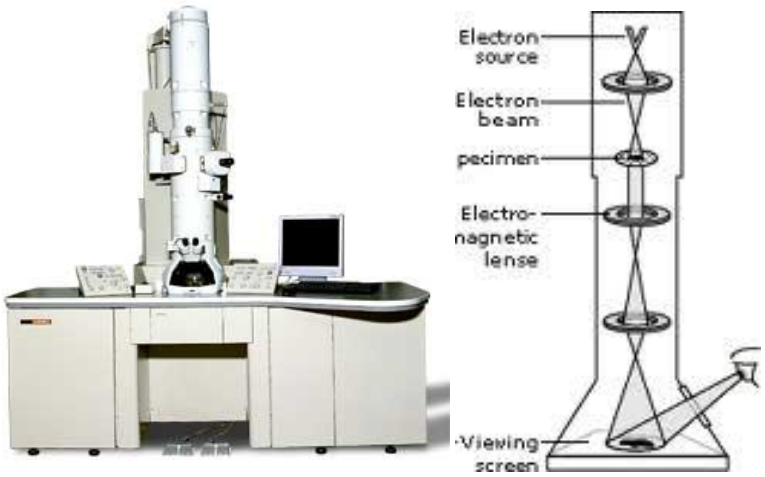


**Figure 29. JEOL JEM-2100 Transmission Electron Microscope (http://www.jeol.com/, http://www.nobelprize.org/)**

### 1.2 Scanning Electron Microscopy (SEM)

The SEM microscope gives information about the topology of a sample and it works using the same principle of the TEM microscope previously described. Electrons are generated through thermionic emission as well, they get accelerated having energies up to 100kV and electromagnetic lenses focus the beam. The electron beam interacts with the specimen and the scattered electrons are further detected and analyzed. The difference is that the information is analyzed from the detector of the instrument.

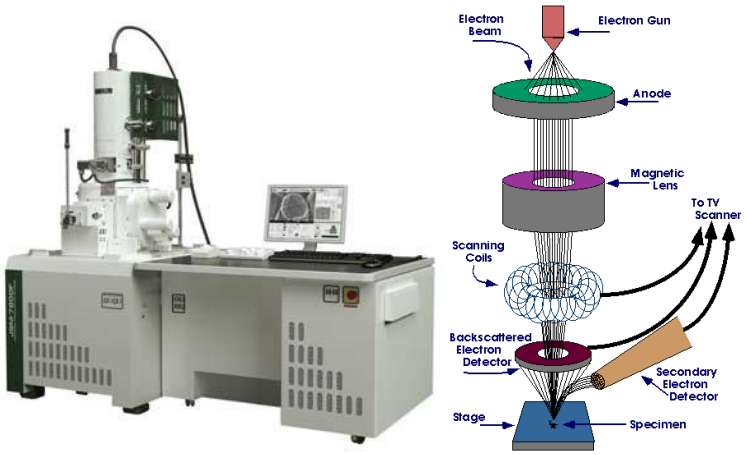


**Figure 30. Field Emission JEOL JSM 7000F SEM (http://www.jeol.com, http://www.purdue.edu)**

Some basic requirements for SEM observation is that the material should be dry, since the specimen chamber is at high vacuum and it should be electrically conductive at least at the surface and grounded in order to prevent the accumulation of electrostatic charge at the surface (charging effect).

**Sputter coater**

Nonconductive samples require coverage with a thin metallic layer using a sputter coater. This instrument has two metallic surfaces in inert gas environment, where high

voltage difference is being produced. At the cathode there is a metal target and at the anode the specimen is being placed. The existence of a free electron in the gas atmosphere can cause ionization of an atom of the gas. The positive ion speeds up towards the cathode where it hits the target.There an atom of the target gets detached and moves to the opposite direction on the specimen. The target is made of a metal, which can be gold, gold/palladium, platinum, nickel, copper or tungsten.
The resolution of this technique is a few nanometers depending on the quality of the sputtering, the metal used, its thickness and the details of the specimen. For achieving higher resolution Field Emission SEM produces clearer, less electrostatically distorted images with spatial resolution down to 0.8nm at 15kV.

### 1.3 Energy-Dispersive X-ray Spectroscopy (EDS)

For the elemental analysis of the specimen Energy-Dispersive X-ray Spectroscopy is used where an X-ray beam interacts with the unique atomic structure of each element giving unique peaks on its X-ray spectrum. The X-ray beam excitation is used in scanning and transmission electron microscopes.

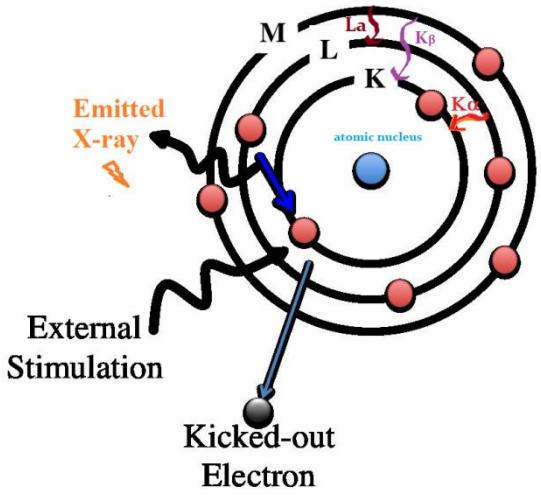


**Figure 31. Schematic diagram of Energy Dispersive X-ray spectroscopy (EDX)**

The incident beam excites an electron in an inner shell of the element, ejecting it from the shell and creating an electron hole in this place. An electron from a higher-energy shell fills the hole and the difference in energy between the higher and the lower energy shell may be released in the form of an X-ray. The number and energy of the X-rays emitted from a specimen are being detected by the energy dispersive X-ray spectroscopy (EDS) detector and measured by an analyzer which is connected to a computer for real time measurement. The X-ray beam can penetrate from around 300 nanometers to 4 micrometers depending on the sample and instrument settings.

### 1.4 Optical microscopy

The optical microscope uses visible light and a system of lenses to magnify images of the specimen. It consists of a light source, the ocular lens, the objectives, a moving stage to focus to the specimen, a diaphragm, a condenser lens and a stage where the

specimen is being placed. As it can be deduced from the following figure the working principle is very similar to the TEM `s.

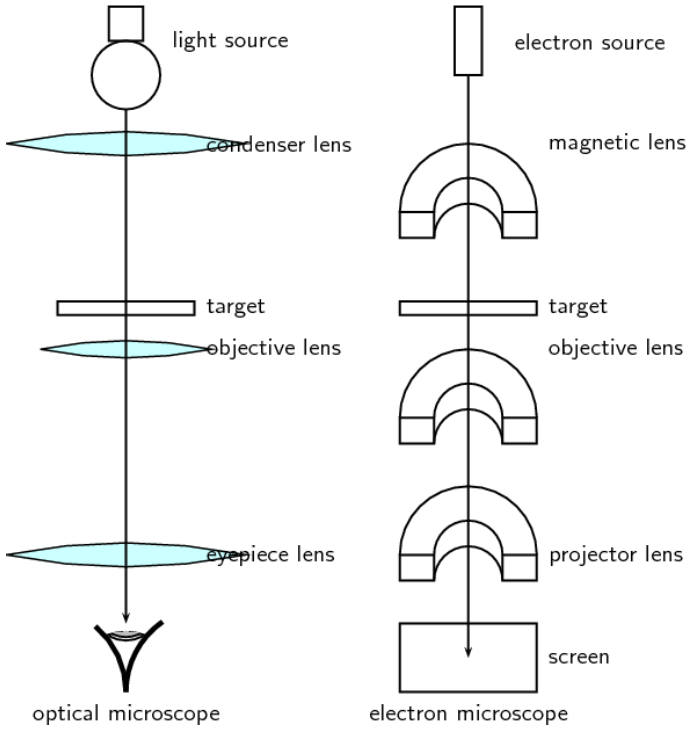


**Figure 32. Schematic diagram of the optical micrograph and a transmission electron microscope (https://everythingscience.co.za)**

### 1.5 Atomic Force Microscopy (AFM)

The AFM is a technique for observation of the 3D profile of the surface characteristics of a specimen by measuring the forces between a sharp probe and the surface.

It has the advantage of imaging almost any type of surface, including polymers, ceramics, composites, glass, and biological samples without pretreatment.

A cantilever, which is made of Si or $Si_3N_4$, gets in contact with the surface of the specimen through a tip, having a radius of some nanometers. Usually, cantilevers oscillate on the surface on a tapping mode having frequency of hundreds of kHz, getting in contact with the surface for a very small fraction of its oscillation period. When the tip touches the surface it records the small force between the probe and the surface by a laser beam deflection system used to detect the exact position of the tip, where a laser is reflected from the back of the cantilever and onto a position-sensitive detector. The force is being measured by Hook's law:

$$F = -kx,$$

where F is the force, k is the stiffness of the cantilever, and x is the distance between the tip and the surface.

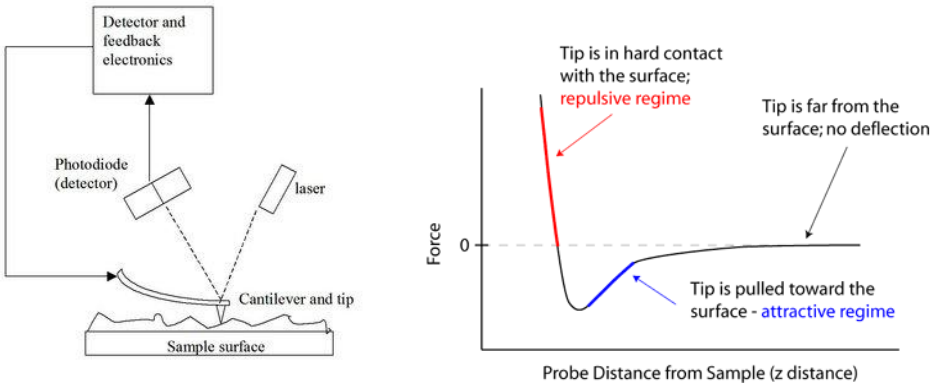


**Figure 33. (left) AFM imaging principle, (right) plot of force as a function of probe-sample separation**

The disadvantage of this technique is that the scanning area is limited to only 150 by 150μm and the sample has to be moved to scan a larger area losing the previous position.

### 1.6 X-Ray Fiber Diffraction

In order to examine the repeating structure of amyloid fibrils along the fiber axis, X-ray fiber diffraction reveals a specific diffraction pattern known as the cross-β pattern, that arises from hydrogen-bonded β-strands running perpendicular to the fiber axis to form a series of β-sheet ribbons that extend along the fiber axis.

A sample having a high degree of alignment and order will give more information in the diffraction pattern. The diffraction pattern of a sample with no alignment will produce reflection rings instead of reflection arcs that are oriented on each axis of the pattern.

A typical cross-β diffraction pattern shows the characteristic 4.7–8 Å diffraction signal on the meridian of the pattern, corresponding to the distance between hydrogen-bonded β-strands. A more diffuse signal on the equator at a variable distance of 10–12 Å arises from the intersheet spacing and is dependent on the size of side chains.

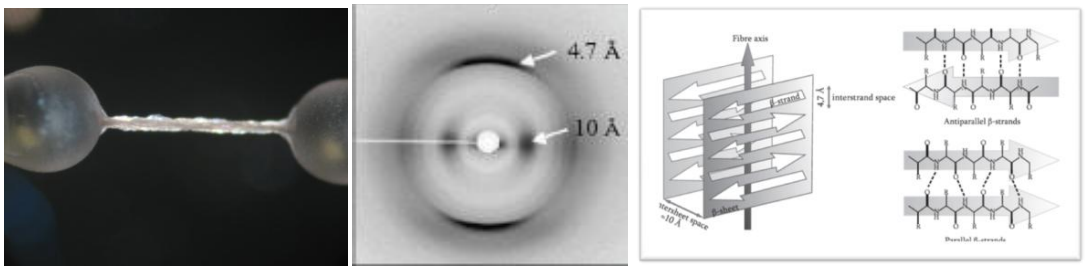


**Figure 34. (left) Orientation of the fibrous solution between glass rods, (middle) a typical amyloid X-ray diffraction pattern and its correlation to the β– sheet structure (right)**

### 1.7 Selected – Area – Diffraction technique (SAED)

Selected area diffraction is a crystallographic technique for the study of the mineralization phase of peptide fibrils and is being performed inside a transmission

electron microscope (TEM). When a focused electron beam hits the sample the atoms of the mineral phase act as a diffraction grating to the electrons due to the size difference. Some electrons are scattered to particular angles, determined by the crystal structure of the sample, while others pass through the sample. The selected area diffraction patter is the image observed by this diffraction where each spot corresponds to a diffraction condition of the sample's crystal structure. Tilting the sample different diffraction spots will appear or disappear.

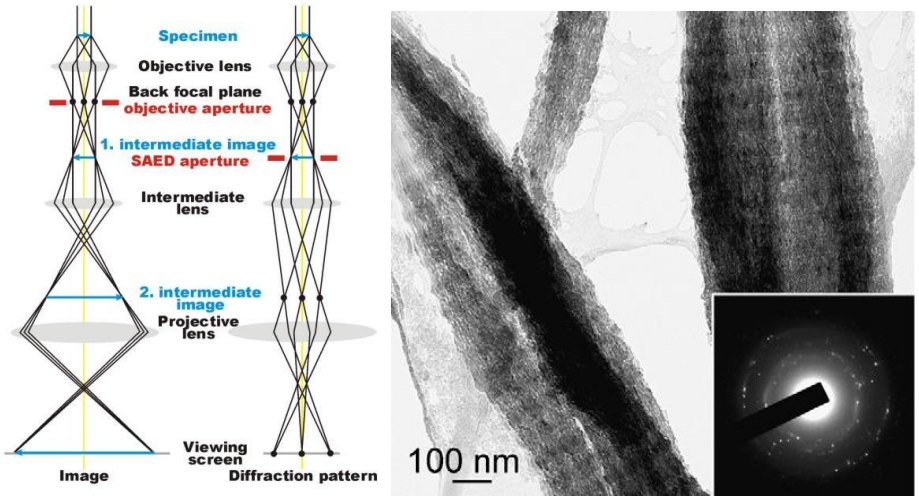


**Figure 35. TEM figure of unstained collagen fibrils showing the crystalline stage of mineralization. The SAED pattern indicates a crystalline phase that is characteristic of apatite (Liu, Kim et al. 2011).**

Below the TEM's sample there is an aperture, which can be inserted into the beam path to block the beam. It contains different sized holes, and can be moved by the user. The beam can be blocked except from a fraction passing through one of the holes. The user moves the aperture hole to the section of the sample that wants to examine, and only this part will contribute to the SAED on the screen.

### 1.8 Nanoindentation test

The nanoindentation is a method used to characterize material mechanical properties on a very small scale which are deformed at the sub-micron scale. The method was developed by Oliver and Pharr and allows determining the hardness (H) and the reduced modulus (Er) from the nanoindentation load-displacement data. The evaluation of the elastic properties of the coatings is based on the precise measurement of the penetration depth of an indenter into the coating. In order to characterize the coatings' mechanical properties, the indenter must have a well-defined geometry and avoid substrate effects.

The hardness is calculated by the maximum load placed on the indenter tip, $P_{max}$, divided by the residual projected area, $A_r$, which is calculated with the use of AFM.

The reduced Young's modulus (Er) is indicative of the stiffness of the material and is affected by both the material and the indenter used.

$$H = \frac{P_{max}}{A_r} \quad , \quad \frac{1}{E_r} = \frac{(1-\nu^2)}{E} + \frac{(1-\nu_i^2)}{E_i}$$

where E and v are Young's modulus and Poisson's ratio for the specimen and Ei and vi are the same parameters for the indenter.

For indentation, the probe is forced into the surface at a selected rate and to a selected maximum force. Imaging is performed in situ using the probe in intermittent contact (tapping mode) AFM. The depth of the indentation is measured from the AFM image to evaluate the hardness of the material. The investigated penetration depths should not exceed 10% of the overall thickness of the coating.

## 2. MATERIALS AND METHODS

### 2.1 Proteins and FMN

Bovine serum albumin (BSA), biotinylated bovine serum albumin (bBSA), biotinamidohexanoyl-6-aminohexanoic acid N-hydroxysuccinimide ester and flavin mononucleotide (FMN) were purchased from SigmaAldrich Finland Oy, Finland.
Avidin was purchased from Belovo Chemicals, Belgium.
FMN, as a cofactor of vitamin B2, was used as a nontoxic photosensitizer in protein crosslinking.

#### Sample preparation

BSA reagent solution contained 200 mg/ml of protein and 4 mM FMN in phosphate buffered saline (PBS, pH ~7.4). BSA was biotinylated via reaction with biotinamidohexanoyl-6-aminohexanoic acid N-hydroxysuccinimide ester in a buffer consisting of 50 mM sodium phosphate and 100 mM NaCl (pH ~ 7). bBSA was used as a solution containing 100 mg/ml of the protein with 04 mM FMN or together with BSA as a solution of 100 mg/ml bBSA and 100 mg/ml BSA with 04 mM FMN. Plain BSA was added to the solution to provide increased mechanical stability. Avidin was studied as solutions containing 50, 100, 200 or 400 mg/ml protein and 04mM FMN in PBS.

#### Photofabrication of protein microstructures

The protein microstructures were fabricated in a chamber between a microscope slide and a coverslip with a 150 μm thick spacer. The chamber was filled with a protein solution and the structures were crosslinked either downwards from the top cover glass or upwards from the bottom microscope slide depending on the fabrication setup in question. The average laser power for the Ti:Sapphire laser setup was varied from 38 mW to 123 mW and the samples were scanned with speeds of 10, 20, 30, 40 and 50 μm/s.
The fabrication of 3D structures was also attempted with the Nd:YAG system by crosslinking simple woodpile structures from BSA. The overall size of the woodpile was 40 × 40 × 10 μm, the distance between the lines in the x-y direction was 5 μm and the inter-layer distance in the z direction was 1 μm. The scanning speed used for the woodpile fabrication was 10 μm/s and the average laser power was 5.67 mW. After crosslinking, all the fabricated structures were rinsed with ion-exchanged water to remove the excess protein solution and the photosensitizer.

### 2.2 Peptides

The peptides used had the following sequences (free amino termini, amidated C-termini): NSGAITIG (Asparagine-Serine-Glycine-Alanine-Isoleucine-Threonine-Isoleucine-Glycine), CSGAITIG (Cysteine-Serine-Glycine-Alanine-Isoleucine-Threonine-Isoleucine-Glycine), DSGAITIG (Aspartic acid-Serine-Glycine-Alanine-Isoleucine-Threonine-Isoleucine-Glycine), DDSGAITIG (Aspartic acid-Aspartic acid-Serine-Glycine-Alanine-Isoleucine-Threonine-Isoleucine-Glycine), DDGAITIG

(Aspartic acid-Aspartic acid -Glycine-Alanine-Isoleucine-Threonine-Isoleucine-Glycine), NAGAITIG (Asparagine-Alanine-Glycine-Alanine-Isoleucine-Threonine-Isoleucine-Glycine) and ASGAITIG (Alanine-Serine-Glycine-Alanine-Isoleucine-Threonine-Isoleucine-Glycine). The peptides were purchased from Eurogentec (Belgium) and had a degree of purity higher than 95%. The lyophilized peptide powders were dissolved in deionized water at various concentrations.

### 2.3 Hybrid materials

Novel, organic/inorganic hybrid materials were specifically designed for Multi Photon Polymerization (MPP) to compensate the disadvantages of the commercial photopolymers, with high optical quality materials, having post-processing chemical and electrochemical inertness, good mechanical and chemical stability. The preparation is straight-forward using the sol–gel technology.

The condensation of a silicon alkoxide with a zirconium alkoxide has been shown to enhance the material's mechanical stability and allow the modification of its refractive index (Ovsianikov, Viertl et al. 2008; Ovsianikov, Shizhou et al. 2009). In addition, hybrid materials provide the possibility of the incorporation of various functional groups using a guest–host or a sidechain– main chain strategy. In a silicon-zirconium hybrid material a 2(dimethylamino) ethyl methacrylate (DMAEMA) monomer was added, which is a photopolymerizable methacrylate moiety, in order to incorporate covalently bound metal binding groups in the 3D structures, being capable of participating in the photopolymerization step. The procedure followed for the preparation of the zirconium - DMAEMA sol-gel is described by the following reactions:

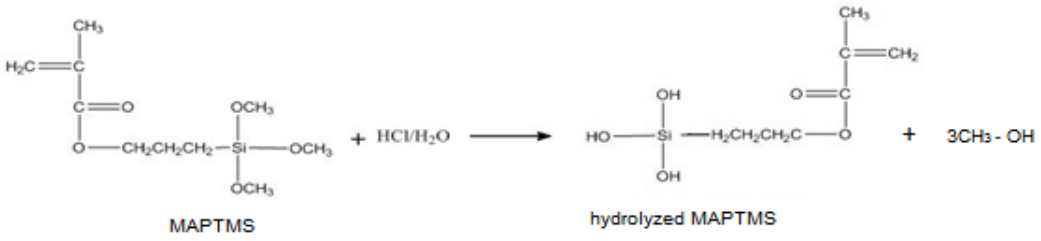


**Figure 36. MAPTMS hydrolysis**

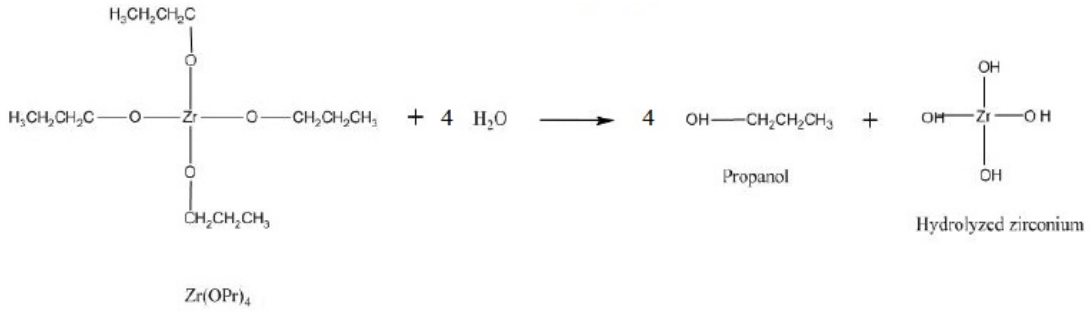


**Figure 37. ZPO hydrolysis**

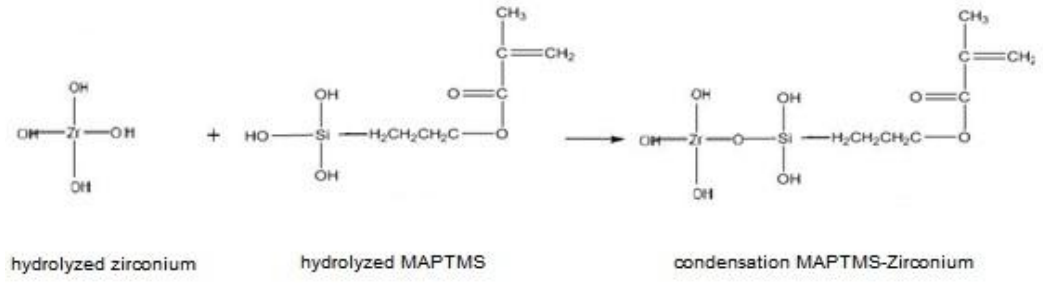


**Figure 38. Condensation MAPTMS-Zirconium**

Firstly for hydrolyzing MAPTMS dilute HCl (0.1M) was added at a 1:0.1 ratio and the mixture was stirred for 5 minutes. Zirconium propoxide (ZPO), Zr (OPr)4, (70% solution in 1-propanol, Sigma-Aldrich), added slowly, was used as an inorganic network former. The molar ratio of ZPO:MAPTMS was 3:7. Afterwards double distilled water was added that provoked the hydrolysis of Zr propoxide groups leading to Zr-OH groups, after 15 minutes of stirring the solution. By mixing the two monomer solutions strong covalent Si-O-Si, Zr-O-Zr, and Si-O-Zr bonds are being formed.

In the end, DMAEMA was added having a molar ratio of (MAPTMS+ZPO):DMAEMA that varied between 5:5 and 9.5:0.5. DMAEMA molecules will be incorporated into the final network after polymerization.

Finally, the photoinitiator (PI) at a 1 % w/w concentration was added to the mixture. The photoinitiator used was 4,4'-bis(diethylamino)benzophenone (Sigma-Aldrich) having miximum absorption at 365 nm. After stirring for a further 15 minutes, the composite were filtered using a 0.22 μm syringe filter.

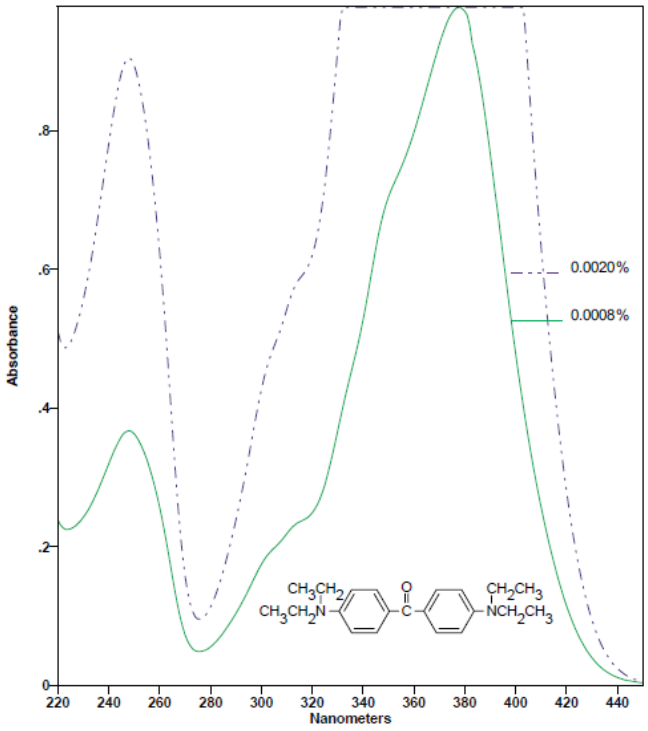


**Figure 39. Absorption spectrum of photoinitiator 4,4'-bis(diethylamino)benzophenone expressed in two different concentrations as % weight of solute in volume of solvent**

The organic groups attached to the inorganic backbone are polymerized with the aid of the photoinitiator using multi photon polymerization and they convert from small unsaturated molecules in the liquid state to irreversible and fully saturated solid macromolecules having aliphatic C-C covalent bonds that further increase the connectivity of the material.

The combination of the sol-gel condensation and the effect of irradiation produce a non-shrinkable material of an organic skeleton rigidified by strong mineral bonds.

### 2.4 3D hybrid structure fabrication with DLW

A Ti:Sapphire femtosecond laser was used operating at 800nm (Femtolasers Fusion). This source is a compact diode-pumped femtosecond laser oscillator with integrated dispersive mirrors that pre-compensate the beam delivery and focusing optics to achieve sub-20 fs duration pulses into the sample. The average power is 400 mW and its repetition rate is 75 MHz.

The beam was focused into the photopolymerisable composite. The structure was generated using an x-y galvanometric mirror digital scanner (Scanlabs Hurryscan II), controlled by SAMLight (SCAPS) software. The scanner was adapted to accommodate high numerical aperture focusing microscope objective lenses (20X, N.A. = 0.65, 40x, N.A. = 0.95, 100x, N.A. = 1.4, Zeiss, Plan Apochromat). To achieve better focusing, the laser beam was expanded 2x using a telescope lens arrangement. Movement on the z-axis and large-scale movement on the x-y plane was achieved with a three-axes linear encoder stage (Physik Instrumente). Beam control was achieved using a mechanical shutter (Uniblitz). The beam intensity was controlled using a motorized attenuator (Altechna). The stages, the shutter and the attenuator were computer-controlled via a National Instruments LabVIEW program. A CCD camera was mounted behind a dichroic mirror for online monitoring of the polymerization process. The platform where the resin is placed drops down and the laser polymerizes the next layer with the last layer on the surface of the coverslip. This process repeats, layer by layer, until the 3D model is complete.

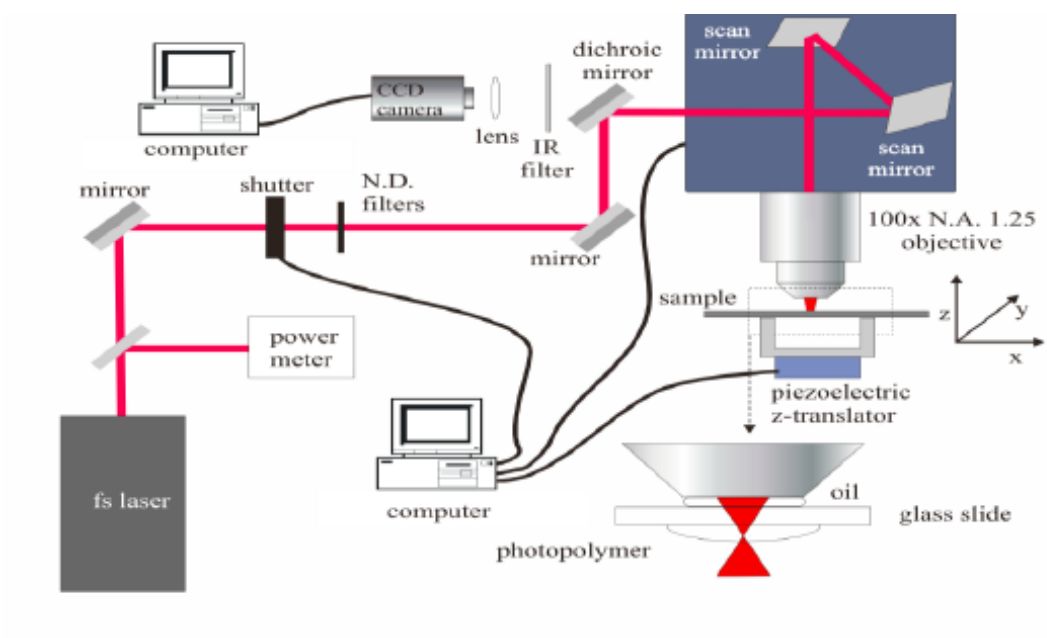


**Figure 40. Optical set-up for MPP**

The samples were prepared by dropcasting above 100 μm thick silanized glass substrates, and were left to dry on a hotplate at 50 °C for 10 minutes. The heating process led to the condensation of the alkoxide groups and the formation of the inorganic matrix. Next, the organic moieties got attached to the inorganic backbone using multi photon polymerization, resulting in the formation of irreversible and fully

saturated aliphatic C-C covalent bonds. After the completion of polymerization, the samples were developed for 20 minutes in a solution of 1propanol and isopropanol, and were further rinsed with isopropanol. The amount of isopropanol added relates to the percentage of DMAEMA used in the hybrid.

### 2.5 Polymeric thin film preparation

For the film preparation the samples were prepared by spin-coating onto 100 micron-thick silanized glass substrates. The films formed were dried in air leading to the condensation of the alkoxide groups and the formation of the inorganic matrix. Next, the organic moieties attached to the inorganic backbone were polymerized using a KrF excimer laser, operating at 248 nm, resulting in the formation of irreversible and fully saturated aliphatic C-C covalent bonds that further increased the connectivity of the material. The samples were subsequently developed for 20 min in a 70:30 1-propanol:isopropanol solution, and were further rinsed with isopropanol.

### 2.6 Mineralization protocol of amyloid peptide fibrils with calcium phosphate on a holley grid

On a microscopy copper grid covered by holley carbon film (300mesh) 8μl of the aqueous solution containing the peptide fibrils were deposited for 2 minutes on the shiny side of the holley grid. The excess fluid was removed with the edge of an absorptive paper. Right away, an 8μl droplet of a 10mM $CaCl_2$ solution dissolved in 25 mM Tris buffer (pH7.4) was deposited on the one side of the grid, while on the opposite side of the grid 8μl of $Na_2HPO_4$ in water in 6mM concentration (pH 9-9.5) were placed. The two solutions diffused instantaneously interacting with the peptide fibrils. The droplet was left for incubation for 30min and afterward was washed off by adding an 8μl droplet of ultrapure water to remove the non-attached particles to the fibrils. With an absorptive paper the material excess was removed. This washing process was repeated for four times.

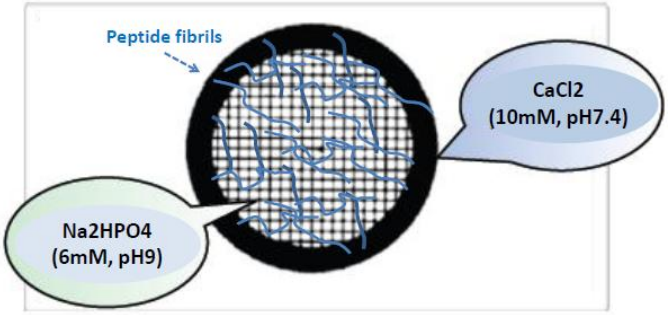


**Figure 41. Cartoon of the protocol followed for amyloid fibril mineralization by deposition of $Na_2HPO_4$ solution on one side and $CaCl_2$ solution on the other side.**

### 2.7 Mineralization of amyloid peptides with calcium phosphate in solution

In an eppendorf tube 20μl of a 1mg/ml peptide solution was agitated for 1h with 20μl of $CaCl_2$ (3.5mM) in Tris buffer solution (pH7.4). Another 20μl droplet was added of $Na_2HPO_4$ (pH8-9) in water (2.1mM) and the total solution was agitated overnight. For observation of the mineralized fibers in the TEM an 8ul droplet of the solution was deposited on a formvar carbon grid.

### 2.8 Scaffold mineralization with calcium phosphate

The steps that took place after the fabrication of the structures are described in the schematic design below:

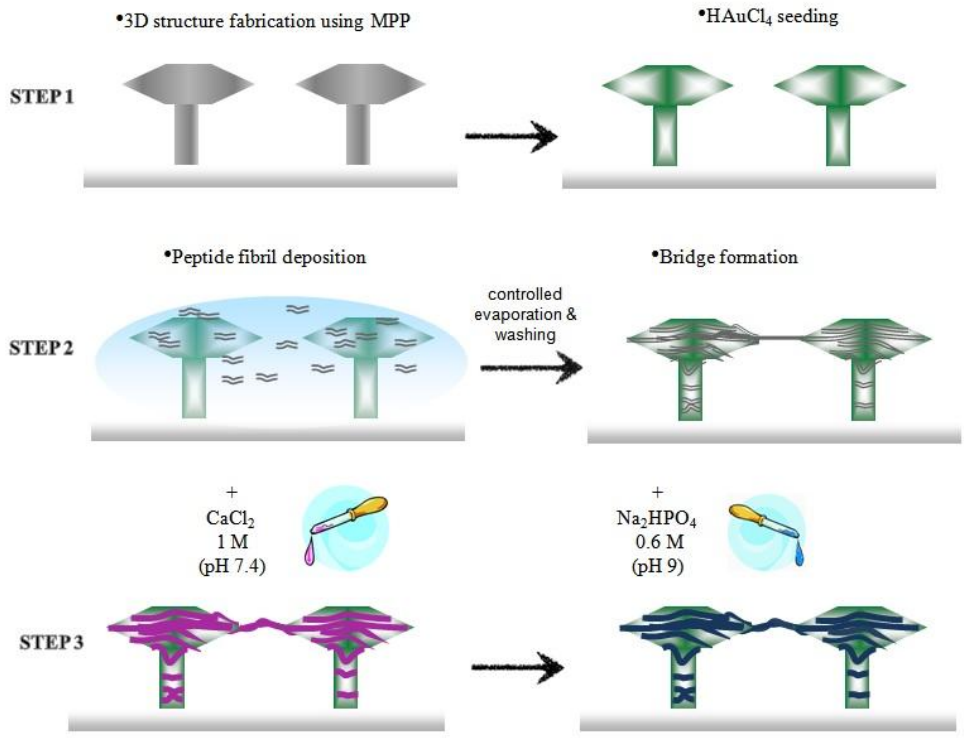


**Figure 42. Scheme illustrating the principle of "scaffold-on-scaffold" for the deposition of aspartic acid containing peptide fibrils on laser photofabricated 3D polymeric scaffolds. Between each step of the process the functionalized structures were washed and rinsed with deionized water.**

#### Gold-ion coating of the scaffold

The 3D structures were initially decorated with gold ions by treating with a 0,63 M aqueous gold chloride trihydrate ($HAuCl_4.3H_2O$) solution for 45 minutes and then washed thrice with deionized water. During this step, the amine groups of the hybrid material became protonated and positively charged and thus bound electrostatically the anionic metal species ($[AuCl_4]^-$). (Christodoulakis, Palioura et al. 2010)

### 3D structure functionalization with the peptide fibrils

Peptide solutions in ultrapure water having 1 mg/ml concentration and being aged for several days were used for the positioning experiments. The peptides used are: DSGAITIG (Aspartic acid-Serine-Glycine-Alanine-Isoleucine-Threonine-Isoleucine-Glycine), DDSGAITIG (Aspartic acid-Aspartic acid-Serine-Glycine-Alanine-Isoleucine-Threonine-Isoleucine-Glycine) and ASGAITIG (Alanine-Serine-Glycine-Alanine-Isoleucine-Threonine-Isoleucine-Glycine). The peptide solutions were incubated on the gold covered 3D structures for 50 minutes at room temperature. They were subsequently washed three times by leaving a water droplet to run on the surface of the sample.

### Mineralization of 3D structures

On the peptide covered structures a droplet of 1M $CaCl_2$ solution dissolved in Tris buffer (pH7.4) was deposited for 50 minutes and was removed by washing the samples by immersion initially and after rinsing with double distilled water. Afterward, another droplet was placed on the calcium coated surface of $Na_2HPO_4$ dissolved in water in a concentration of 0,6M and 0,06M (pH 9.0-9.5) for 30min. Finally the samples were washed off by immersion and rinsed with water to remove the non-attached particles to the fibrils.

### Mineralized film preparation for the cell culture experiments

The cell culture experiments were carried out on polymerized films of the hybrid organic-inorganic material. This was done in order to allow cell counting and statistical analysis that followed. The spin-coated films reacted with gold ions and functionalized with the peptide fibrils, following the process described previously.

For the mineralization of the films a droplet of 1M $CaCl_2$ was deposited over the films in order to cover the whole surface. After 45 minutes it was removed by washing the samples in ultrapure water. Another droplet was placed on the calcium coated surface of $Na_2HPO_4$ dissolved in water at a concentration of 0,06M (pH 9.0-9.5) for 30 minutes. Finally the samples were washed by immersion in water to remove the non attached particles.

## 2.9 Metallization protocol of amyloid peptide fibrils

The fibrils were tested for binding gold, silver and platinum nanoparticles, using previously described protocols (Kasotakis, Mossou et al. 2009), in order to prove the bifunctionality of the designed peptide sequences.

- **Metallization of peptides with gold nanoparticles**

The process followed for gold metalization was according to the Turkevich method for gold nanoparticle synthesis (Kimling, Maier et al. 2006), a protocol followed also by Kasotakis et al. (Kasotakis, Mossou et al. 2009). 20 μl of $HAuCl_4$ $3H_2O$ aqueous

solution in 5 mM concentration were heated for 5 min at 100$^{o}$C and subsequently added to 80 μl of peptide fibrils being in a concentration of 0.6mg/ml in ultrapure water. After 45 min incubation in a vortex, 4 μl of reducing agent (sodium citrate 1%) was added in the solution and was left overnight for incubation.

- **Metallization of peptides with silver nanoparticles**

For the synthesis of silver nanoparticles 20 μl of $AgNO_3$ aqueous solution (1 M) was heated for 5 min at 100$^{o}$C and subsequently added to 80 μl of peptide fibril solution in ultrapure water (2mg/ml). After 18 min incubation in vortex, 8 μl of reducing agent (sodium citrate 1%) was added to the solution and left for incubation overnight.

- **Metallization of peptides with platinum nanoparticles**

For the synthesis of platinum nanoparticles 0.15 M aqueous solution of ascorbic acid was mixed with 0.02 M aqueous solution of $H_2PtCl_6$ $H_2O$ and 60 μl of the peptide solution (1mg/ml). The solution was mixed overnight in vortex.

### 2.10 Scaffold functionalization with metal-binding amyloid peptides

The 3D structures were coated with aqueous gold chloride trihydrate ($HAuCl_4.3H_2O$) and some of them were further immersed in a 6,6 M aqueous NaBH4 solution for 35 minutes in order to reduce the gold ions and form gold nanoparticles. Finally, the samples were rinsed with copious amount of deionized water and dried in air.

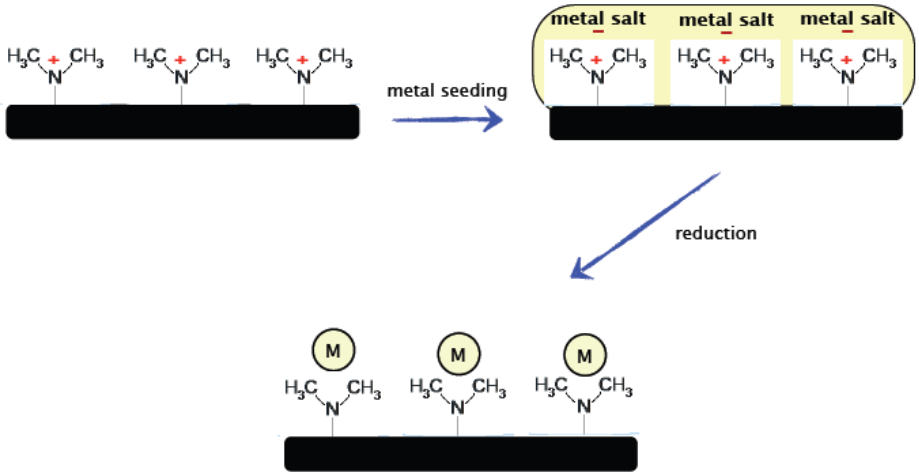


**Figure 43. Metallization of organic-inorganic material with metal-binding sites**

Peptide fibrils that were aged in ultrapure water were incubated on the gold decorated 3D structures for 50 minutes at room temperature. They were subsequently washed three times by leaving a water droplet to run on the surface of the sample.

The peptides used were the previously studied peptide sequences NSGAITIG (Asparagine-Serine-Glycine-Alanine-Isoleucine-Threonine-Isoleucine-Glycine), CSGAITIG (Cysteine-Serine-Glycine-Alanine-Isoleucine-Threonine-Isoleucine-

Glycine), and NAGAITIG (Asparagine-Alanine-Glycine-Alanine-Isoleucine-Threonine-Isoleucine-Glycine).

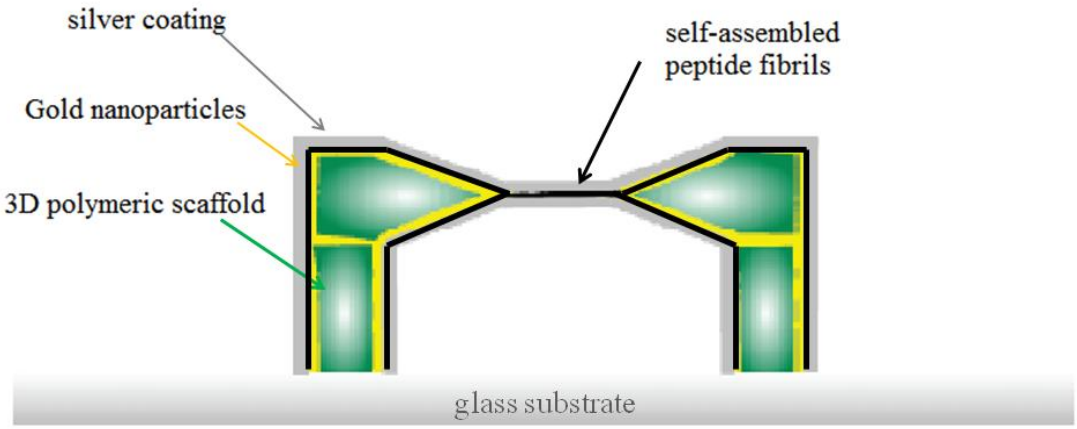


**Figure 44. Cartoon representation of silver metallization on the deposited peptide fibrils over 3D polymeric structures**

For further metallization of the peptide covered 3D structures the following process was followed. For gold decoration the system was incubated in $HAuCl_4$ aq. solution (100mM) for 1 hour, washed with copious double distilled water and reduced with 10% sodium citrate reducing agent for 50 minutes. The samples were finally washed by immersion in double distilled water.

For silver decoration of the peptide covered structures the system was incubated in $AgNO_3$ aq. solution (100mM) for 2 hours and washed with copious double distilled water. Further reduction followed with 1% sodium citrate for 50 minutes and the samples were finally washed by immersing them in ultrapure water.

## 2.11 Electroless plating protocols for 3D conducting nanostructures

Two different protocols were investigated for the metallization of 3D microstructures fabricated with DLW that were first tested on spincoated films. The main steps followed are:

1. treatment of the surface with a metal ion precursor which allowed the binding of the metal species onto the 3D structures
2. metal reduction to form the metal nanoparticle seeds on the nanostructures
3. silver bath/plating process to obtain the metal coated structures.

Metallization Protocol 1 (MP1)

The surface of the hybrid structures were initially seeded with gold particles (5.5 x10–4 M $HAuCl_4.3H_2O$) for 35 minutes and then washed by immersion twice in deionized water for 10 minutes. Next, the structures were immersed in a 6.6 M aqueous $NaBH_4$

solution for 35 minutes in order to reduce the gold ions and form the seed gold nanoparticles. The $NaBH_4$ was added slowly to the water with slow agitation because it is an exothermic reaction. The immersion time in the NaBH4 solution was determined by the change in the color of the material from yellow to dark red, which is attributed to the light refraction by size of the metal particles. Finally, the film was rinsed with copious amount of deionized water.

A colloidal dispersion of arabic gum was used in order to control decomposition since the silvering bath is highly unstable and decomposes as soon as the silvering process starts. The solution prepared comprised of 12 mL of a 33 wt % prefiltered aqueous gum Arabic solution, 2 mL of an aqueous citrate buffer (1.5 M citric acid and 0.5 M trisodium citrate, pH 3.5), 3 mL of a 37 mM aqueous silver lactate solution, and 3 mL of a 0.52 M aqueous hydroquinone solution. (Chen, Tal et al. 2006). The above solutions were mixed at room temperature and were stirred until a homogeneous solution was obtained. Next, the structures activated with gold nanoparticles were immersed into the silver bath for various time periods without agitation. After the silver plating process the samples were removed from the bath and were rinsed several times with copious amount of deionized water in order to remove any materials that were not attached to the structures. Finally, the silver coated structures were dried in air before being measured.

Metallization Protocol 2 (MP2)

The second protocol followed is a modification of the method reported by Kawata et al. (Takeyasu, Tanaka et al. 2008), where for the seeding step the samples were first immersed in a 0.05 mol/L $AgNO_3$ solution at room temperature for 38 hours, and after thorough rinsing with double distilled water, they were subsequently dipped into an aqueous $NaBH_4$ solution (6.6 M) to reduce the silver ions and form silver nanoparticles. During this step the material surface gets fully covered with densely packed silver nanoparticles allowing the selective silver plating of the structures in the following step. The amount of silver plating onto the structures was found to be proportional to the immersion time in the $AgNO_3$ solution and the sodium borohydride solution. The films turned out to be "mirror-like" when seeded and reduced for longer times.

For the silver plating a 0.2 M $AgNO_3$ aqueous solution was mixed with 5.6 % $NH_3$ and 1.9 M glucose ($C_6H_{12}O_6$ > 98%) as a reducing agent, at a volumetric ratio of 5:3:8. The samples were immersed in the solution for less than 5 minutes because after this time the solution started to degrade and extensive silver reduction was observed in solution, besides the silver particles deposited on the nanostructures. The plating process was repeated by immersing the sample in a fresh silver plating solution. Finally, the samples were extensively rinsed with acetone and deionized water and were dried in air at room temperature before being analyzed.

The silver bath being a very unstable solution an alternative method was also employed to improve the solution's stability. It involved the use of a 33 wt% colloidal dispersion of arabic gum added to a 1:10 volume ratio in the above silver plating solution. The samples were immersed in the arabic gum containing silver plating solution for 18 minutes. After that time the colour of the silver bath started changing

again, signaling the degradation of the solution. Finally, the samples were removed from the silver bath and were washed thoroughly in acetone and double distilled water.

### 2.12 Functionalization of conductive 3D structures with amyloid peptides and further metallization

A 10ul droplet of a peptide aqueous solution being aged for several days was used for the positioning experiments containing the metal-binding peptide CSGAITIG in a concentration of 3mg/ml. It was deposited on large 3D conducting structures for 65 minutes and after bridging the gap between the structures it was washed with distilled water. The whole structure was further metalized with aqueous chloroauric acid ($HAuCl_4$) for 1 hour in a concentration of 0.1M and after washing with ultrapure water the gold ions were reduced to nanoparticles with the addition of 10% sodium citrate for 50 minutes. The samples were washed with copious water several times.

### 2.13 Conductivity measurements

The equipment used for analyzing the current-voltage characteristics of the metallized structures was a Tektronix 370 curve tracer. Voltage was applied through needles deposited on the samples and the resistance value was calculated by the reciprocal of the slope of the line of the VI curve. The graphs were linear fits to the plots acquired by the curve tracer at low currents.

### 2.14 X-ray Diffraction (XRD)

Drop casted thin films onto 100 micron thick glass substrates were prepared and dried at 50 °C for 10 minutes before being polymerized. They were subsequently metalized as described above. A Rigaku RINT 2000 Series wide angle diffractometer was used to determine the crystallinity of the metal coating. Measurements were made from 2θ = 5΄ to 120΄ in steps of 2θ = 0.02΄ using the following operating conditions: I = 178 mA and V = 40 kV.

### 2.15 Transmission measurements for photonic crystals

For the transmission measurements a white light source pumped at 1064 nm (Fianium) was used. The light beam was focused normally to the sample surface using a 7.5 cm focal length lens, while the transmitted light was collected using an optical spectrometer (Ocean Optics S2000). The diameter of the focused beam in the sample was 24 μm.

### 2.16 Nanoindentation test

The mechanical behavior of the material thin films were performed using a Hysitron riboLabVR nanomechanical test instrument. The transducer used to perform the nanoindentation tests can apply loads in the range of 1–10,000 μN with a high load resolution of 1 nN, while the maximum penetration depth that can be recorded is 3000 nm having resolution of 0.04 nm. A three-sided pyramidal Berkovich diamond

indenter (120 nm radius of curvature) was used for the measurement of hardness, stiffness and elastic modulus. The tip radius was calculated prior to the experimental procedure, by calibration on fused quartz. Experiments were performed in a clean area environment with about 45% humidity and 23$^{o}$C ambient temperature. The instrument used was equipped with a Scanning Probe Microscope (SPM), in which the mounted Berkovich probe tip was moved in a raster scan pattern across a sample surface using a three-axis piezo positioner.

Indentation tests were performed on a 100 μm silanized glass substrate where the hardness (H) and the reduced modulus (Er) of the substrate were measured. Additionally, films with thicknesses in the order of a few micrometers were deposited onto silanized glass substrates by spin coating and were tested at several applied loads (from 10 to 6000 μN) before and after submersion into the cell culture medium (MEM alpha modification) for 2 hours and following rinsing with water.

Repeatable tests at each applied load were performed at the center of the samples and at four different points across the samples diameter. The distance between neighboring indentation sites was larger than 6 μm in order to avoid the lateral size of the plastic zone around the largest indents and exclude the mutual influence of individual indents.

## 2.17 Transmission electron microscopy (TEM)

The Transmission Electron Microscopes used were a JEOL JEM – 100C microscope operating at 80kVolts and a JEOL JEM – 2100/High Resolution operating at 80kVolts or 200kVolts, depending on the resolution we wanted to achieve. The negative staining used to create contrast to the specimen is a solution of uranyl acetate 1% of which 8μl were deposited on one side of our sample for 2 minutes removing the excess of the fluid with a filter paper.

## 2.18 Scanning Electron Microscopy (SEM) – Field Emission SEM (FESEM)

For the Scanning Electron Microscopy (SEM) measurements a JEOL JSM-6390LV microscope was used, whereas high resolution SEM images were obtained on a Field Emission JEOL JSM 7000F SEM. The samples were gold sputtered with 10nm gold and the observation was made at 15 kVolts.

### Sample preparation for SEM imaging of photocross-linked protein microstructures

The protein samples were fixed in 5 % (v/v) glutaraldehyde for 15 min, then dehydrated by sequential wash for 15 min in ion-exchanged water, 1:1 ethanol/H2O, 100 % (v/v) ethanol, 1:1 ethanol/methanol and 100 % (v/v) methanol (twice). After overnight drying in a desiccator, the samples were sputter coated with gold in argon atmosphere to a nominal thickness of 75 nm or 15 nm (S 150 Sputter Coater, Edwards

Ltd., UK or SCD 050 Sputter Coater, BAL-TEC AG, Liechtenstein). The samples were imaged using either a Philips XL-30 (Philips Electron Optics, the Netherlands) or a JEOL JSM – 6390 LV (JEOL Ltd., Japan) scanning electron microscope with an acceleration voltage of 5 kV or 10 kV.

### 2.19 Energy – Dispersive X – ray Spectroscopy (EDS)

The elemental composition of the samples was identified using the SEM instrument.

### 2.20 Optical microscopy (for 'Pre-osteoblastic cell response on three-dimensional, organic-inorganic hybrid material scaffolds for bone tissue engineering')

A suspension of 2 x $10^4$ cells in alpha-MEM with 1% FBS were seeded on specimens and placed in the cell culture incubator at 37 $^{o}$C. Cells on the specimens were examined daily for 7 days and visualized by optical microscopy by means of a Zeiss Axiovert 200 microscope. Images were taken by a ProgResVR CFscan Jenoptik camera (Jena, Germany) using the ProgResVR CapturePro 2.0 software and objective lenses for 10 and 20-fold magnifications.

**Optical microscopy (**for 'Cell response on mineralized amyloid peptides on top of a hybrid scaffold: A new route in 'scaffold on scaffold' bone tissue engineering')

The process described previously was followed but the cell adhesion on the specimens was visualized from the first hour and up to 24 hours.

### 2.21 AFM imaging

The AFM model used was a MULTIMODE with a NANOSCOPE IIIA controller of DIGITAL INSTRUMENTS (BRUKER) working at the tapping mode. The maximum frequency is at 300 kHz and the typical spike radius is 1 nm.

**AFM imaging of photocross-linked protein microstructures**

Avidin, BSA and bBSA were studied by non-contact mode atomic force (AFM) microscopy (XE-100, Park Systems Inc., USA). All measurements were performed using silicon probes (ACTa-910M, Applied NanoStructures Inc., USA) with a nominal resonance frequency of 300 kHz, spring constant of 4 N/m, a pyramidal shaped tip (radius < 10 nm) and an aluminium reflective coating. Images were acquired with a scan speed of 0.15 or 0.40 Hz.

### 2.22 X-ray Fiber Diffraction

A droplet of a fibril containing solution is placed between two glass rods mounted on a substrate with plasticine. During drying the fibrils stay aligned parallel to the rod axis. The X – rays are focused on the aligned fibers at right angles and the diffraction pattern is recorded (Luckey, Hernandez et al. 2000).

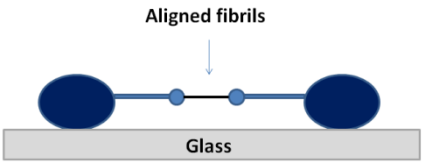


**Figure 45. Cartoon of the sample preparation for X-ray fiber diffraction**

X-ray fiber diffraction experiments were performed at the European Synchrotron Radiation Facility (ESRF) in Grenoble (beamlines ID14-1 and ID14-2). The beam size was 400×600 μm with wavelength 0.933 Å. This experimental arrangement was showed to be optimal for thin amyloid fibrils (Papanikolopoulou, Schoehn et al. 2005). Exposure times were typically of the order of 50 seconds. Data measurements were made using FIT2D (Hammersley 1998) and CCP13 software (Squire 2003)

## 2.23 Selected – Area – Diffraction technique (SAED)

In order to study the mineralization phase on the peptides the Selected Area Diffraction (SAD) technique was used. The technique was performed by a Transmission electron microscope, FEI Tecnai 10 electron microscope (FEI company, Eindhoven, Netherlands) with a LaB6-source at 100 kV acceleration voltage was used.

# E. RESULTS AND DISCUSSION

## 4. Applications in 3D patterning of self-assembled peptides on hybrid structures – Part 1: Metallized structures for biosensing

### 4.1 Fabrication of 3D conducting structures

Negative photoresists were used previously for the production of high resolution 3D structures with DLW and subsequent metallization with electroless plating (Duan, Sun et al. 2004; Kaneko, Yamamoto et al. 2008; Sun, Dong et al. 2008). The disadvantages of the methods used was the fact that in order to activate the photosensitive material surface for electroless plating, additional processing for surface functionalization is required (Chen, Tal et al. 2006), but still the density of the metal binding sites on the structure could not be controlled, resulting in variable metallization quality. In another approach, the material was doped with metal binding tertiary amine moieties (Takeyasu, Tanaka et al. 2008). The density of the binding sites could be controlled but, the metal deposition proved not to be selective.

In this work, the three-dimensional hybrid organic-inorganic structures were fabricated with a novel photosensitive material containing metal-binding tertiary amine moieties. The problem of additional surface processing and reduced selectivity was solved with the introduction of photopolymerizable methacrylate moieties in the silicon-zirconium hybrid material that were added with the incorporation of 2-(dimethylamino) ethyl methacrylate (DMAEMA) monomer. Electroless plating technique was used for metallizing the structures with silver and the technique was compared with the metal bath techniques.
The structurability and resolution of the DMAEMA content was investigated, as well as the influence of the exposed amine groups for the metallization quality of the structures. The silver plating technique is optimized by investigating initially the effect of the amine content, and after the metal seeding and reduction parameters, for acquiring high resolution 3D structures selectively metallized exhibiting ohmic conductivity.

#### Effect of the DMAEMA content of the material

The influence of the DMAEMA content of the material on its structurability, structure resolution and metallization quality of the microstructures was examined.

- Structurability and resolution

Different concentrations ranging from 5 to 60 mole% of the metal-binding monomer DMAEMA were added in the zirconium-containing organic-inorganic photosensitive material in order to investigate the structurability of the final material. 3D structures were fabricated using the process described in the Materials and Methods chapter. SEM images of the fabricated structures are shown in the figure below.

It was found that it is possible to produce 3D structures using up to 60% DMAEMA in the hybrid composite, however as it can be seen the highest resolution is achieved for 5% DMAEMA. As the amount of DMAEMA increases, the material's stiffness reduces due to the increase of the organic content of the material, and the structures lose mainly their mechanical stability, but also their resolution. However, at the high organic loadings, the increased elasticity of the material allows the fabrication of larger structures without cracking. Thus, the 30% DMAEMA composite was chosen for small, high resolution structures, whereas the 50% DMAEMA composite was selected for larger structures, when the structure resolution is not the main issue.

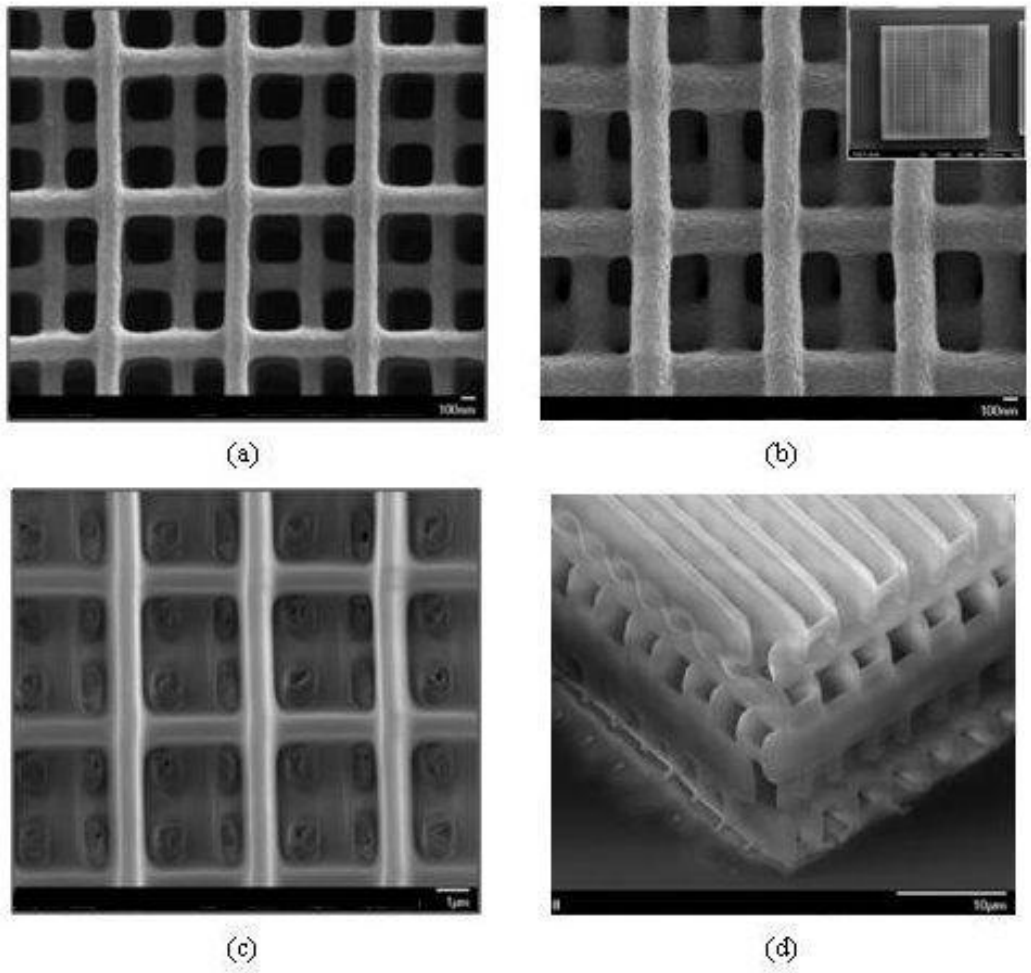


**Figure 46. Details of 3D structures fabricated using DMAEMA (a) 5%, (b) 10% (c) 30% and (d) 50%. (b) insert: a view of the full structure. (Terzaki, Gaidukeviciute et al. 2011)**

- Metallization quality

In order to investigate the metallization quality vs. the material composition, structures were fabricated by DLW using materials with different DMAEMA contents. The following picture shows metallated woodpile structures made from materials with different DMAEMA content after 25 minutes silver plating.

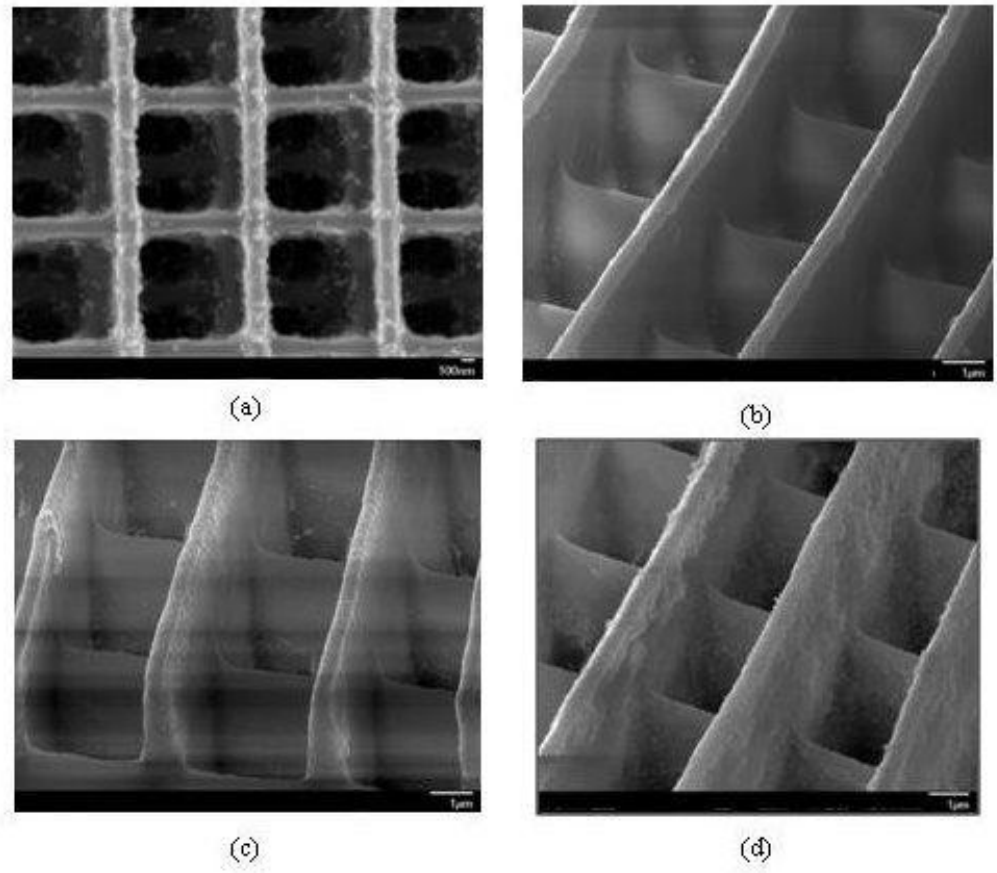


**Figure 47. Metalated 3D structures fabricated using a composite material containing (a) 5%, (b) 10%, (c) 30% and (d) 50% DMAEMA. (Terzaki, Gaidukeviciute et al. 2011)**

In figure (a) a woodpile structure is shown fabricated using a material with 5% DMAEMA. As discussed earlier, this composition gave the highest resolution structures. However, after metallization, it was clear that this low DMAEMA content did not provide enough metal binding sites on the surface of the structures, and instead of a uniform metal coverage, the structures were covered by scattered nanoparticles which grew bigger as the plating time increased. This is more obvious when films instead of structures were used for the metalization process. Similar results were obtained for the structures fabricated using 10% DMAEMA (Figure (b)). On the other hand, as the percentage of DMAEMA increased to 50%, there were sufficient binding sites to provide uniform metal coverage during the plating process however, the quality of the structures deteriorated, because the organic content increased and the mechanical stability of the structures decreased (Figure (d)). As a compromise of the structure resolution and the metallization efficiency the 30% DMAEMA composite was chosen for small, high resolution and high metalization quality structures (Figure (c)).

**Influence of the seeding parameters on the metallization quality**

The XRD pattern below was obtained from a film that was seeded with the gold nanoparticles. The broad peak at around 20° is assigned to the hybrid material while

the appearance of the peaks at 38°, 44°, 64°, 78° and 82° are characteristic of the crystalline structure of the gold particles and verify the formation of the gold seeds on the film.

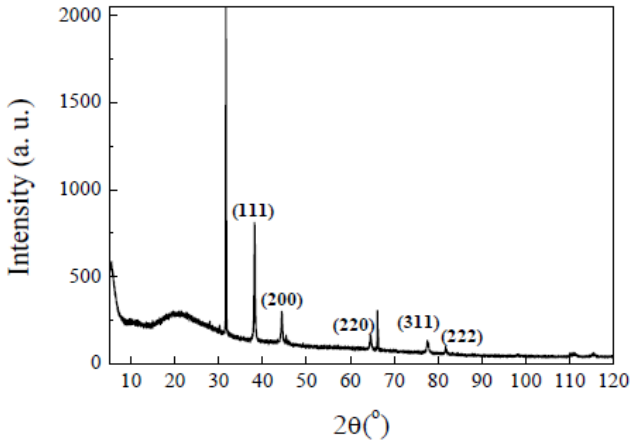


**Figure 48. X-ray Diffraction pattern of a hybrid film seeded with gold nanoparticles. (Terzaki, Gaidukeviciute et al. 2011)**

The film was subsequently covered with silver using the Metallization Protocol 1 (MP1), it was observed that by varying the immersion time in the metal bath, layers of different thickness covered the structures affecting their optical properties as it can be seen in the following reflectance graph. The hybrid material used was the one containing 10% DMAEMA, which gave the highest structurability resolution with DLW.

Besides the good optical results that this technique gives, the metalized structures gave no conductivity results.

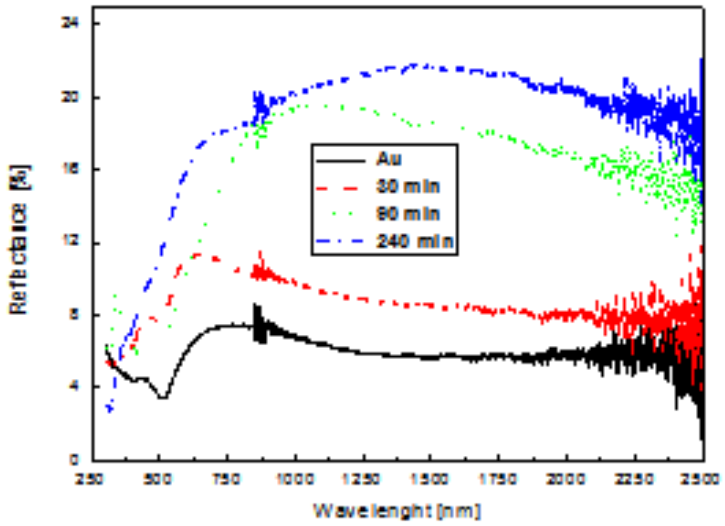


**Figure 49. Reflectance dependence on immersion time in the Ag bath of a 10% DMAEMA containing hybrid material (Terzaki, Gaidukeviciute et al. 2011)**

Another metallization protocol was investigated as described in the Materials and Methods chapter (MP2), the electroless plating technique. Conductivity measurements, discussed below, were used to assess the silver coating quality. In

order to obtain a smooth metallized surface, it is important to control both the size and density of the seed nanoparticles and for this the seeding process was varied by immersion of the films in 0.05 mol/L AgNO3 aqueous solution at room temperature for a variation of time between 24 and 38 hrs. The most densely packed Ag nanoparticles on the structures' surface were observed at the maximum time of immersion, determining the seeding time at 38h for the following experiments. The DMAEMA content of the material and the silver reduction time were also varied and their effect on the density and size of the silver particles were investigated.

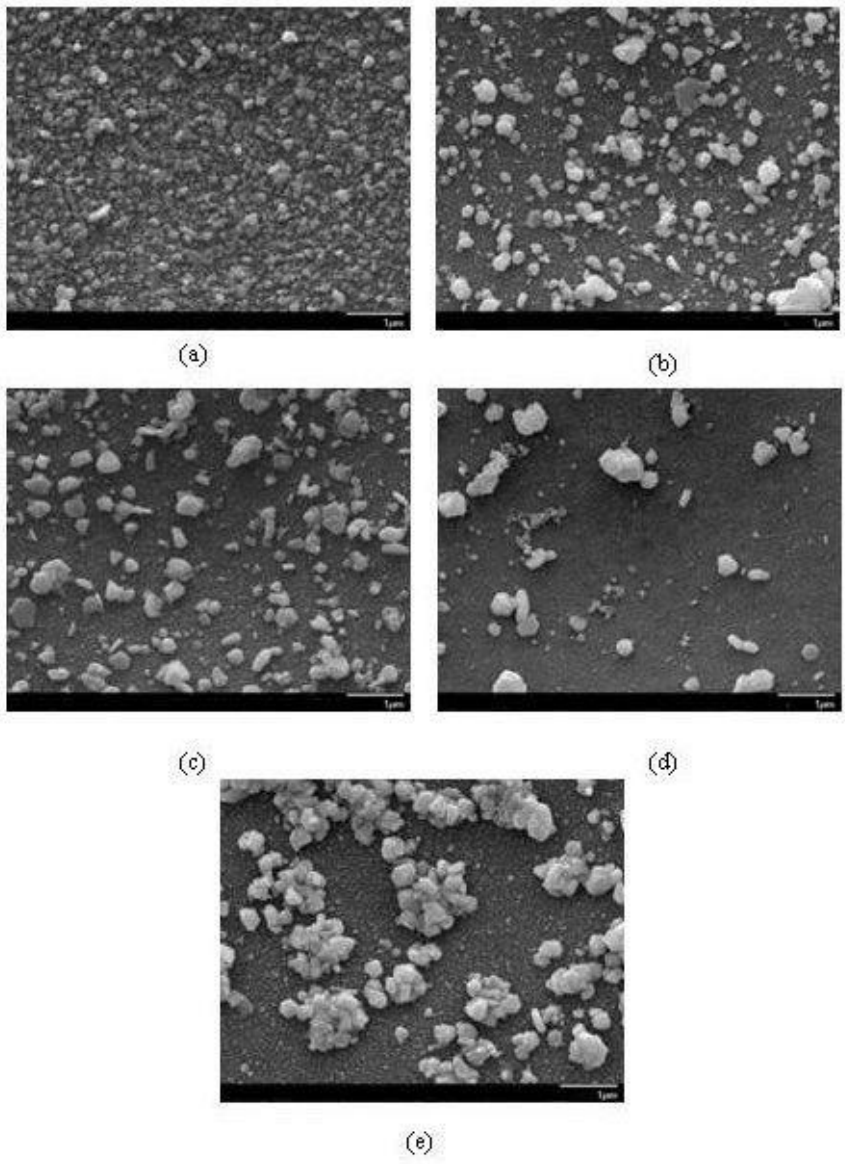


**Figure 50. Effect of reduction time (a) 2 hrs, (b) 6 hrs, (c) 8 hrs, (d) 10 hrs and (e) 12 hrs on particle size. (Terzaki, Gaidukeviciute et al. 2011)**

In the above pictures the influence of reduction time on the size and density of the seed nanoparticles was investigated. The immersion time in the reducing agent solution was varied between 2 and 12 hours and afterwards the samples were plated with silver. After 2 hours of reduction the silver particles on the film surface are

sparsely dispersed, while upon increasing the reduction time the particles start to grow larger in size and form a more dense metal coating on the surface, until they start forming big clusters for very long reduction times.

**Conductivity Measurements**

For conductivity measurements a 50% DMAEMA-containing material was used for making larger structures, where resolution is not as important as the material flexibility, as well as a 30% DMAEMA-containing material. The conductivity of the metallated structures for both DMAEMA concentrations was investigated, using the MP1 and the two variations of MP2 (with and without arabic gum) metallization protocols described earlier, and structures similar to the ones shown in the following figure.

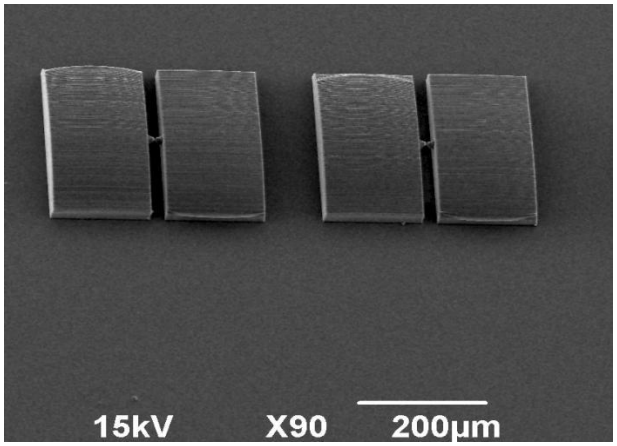


**Figure 51. Large 3D structures for conductivity measurements fabricated using a composite that contains 50% DMAEMA. (Terzaki, Gaidukeviciute et al. 2011)**

It was found that the structures metallized using MP1, did not exhibit conductivity, while the ones metallized using MP2 in the presence of arabic gum were found to have diode conductivity when seeded for 38 hours and reduced for more than 8 hours. Structures metallized using MP2 without arabic gum were measured to have ohmic behavior.

Different seeding and reduction times using MP2 were also investigated for a 50% DMAEMA film. The results are shown in the table that follows. It can be seen that the structures that have been seeded and reduced for longer times exhibit lower resistance.

**Table 3. The effect of seeding and reduction on resistance (Terzaki, Gaidukeviciute et al. 2011)**

| Sample | Ag seeding (hours) | $NaBH_4$ reduction (hours) | Resistance (Ohms) |
|---|---|---|---|
| A | 42 | 22.5 | 44.6 |
| B | 42 | 22.5 | 53.3 |
| C | 42 | 4 | 729 |
| D | 23 | 4 | Not conductive |

According to the below graph, samples that have been seeded and reduced for longer times exhibit higher conductivity. The samples A and B that were metallized under the same conditions have a measured resistance of the same range. In sample D the seeded nanoparticles were not enough in order to have total coverage of the polymeric surface during the plating process.

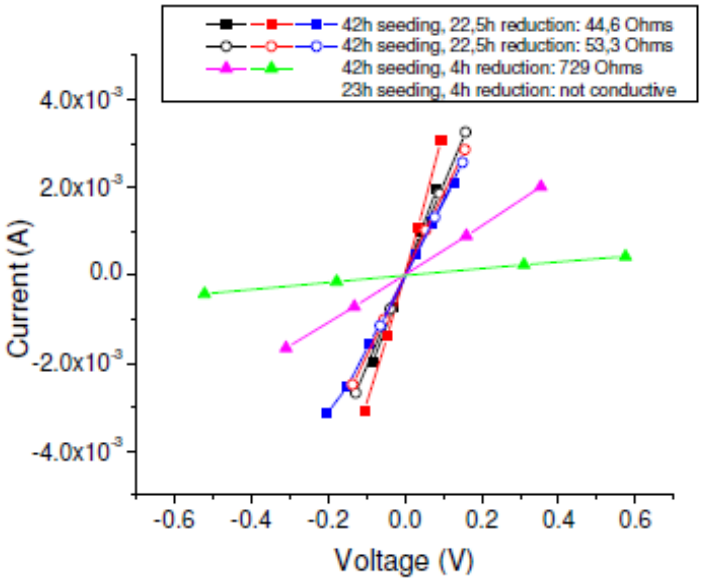


**Figure 52. Current applied to voltage measured on the surface of the metallized structures, (Terzaki, Gaidukeviciute et al. 2011)**

Metal deposition is selective and occurs only on the pretreated area of the hybrid material. The seeding step as well as the reduction of the seeded ions influences silver layer quality and thickness.

Using the optimum seeding and reduction parameters for each material, the resistance of the structures for the two different DMAEMA compositions, 30% and 50%, was measured. The results are shown below. The ohmic response of typical structures for both DMAEMA concentrations is shown in the figure that follows.

**Table 4. Effect of the DMAEMA Content on the resistance of the structures (Terzaki, Gaidukeviciute et al. 2011)**

| DMAEMA | Ag seeding (hrs) | $NaBH_4$ reduction (hrs) | Resistance (Ohms) |
|---|---|---|---|
| 30% | 43 | 22.5 | 3.5 ± 0.2 |
| 50% | 43 | 22.5 | 1.6 ± 0.1 |

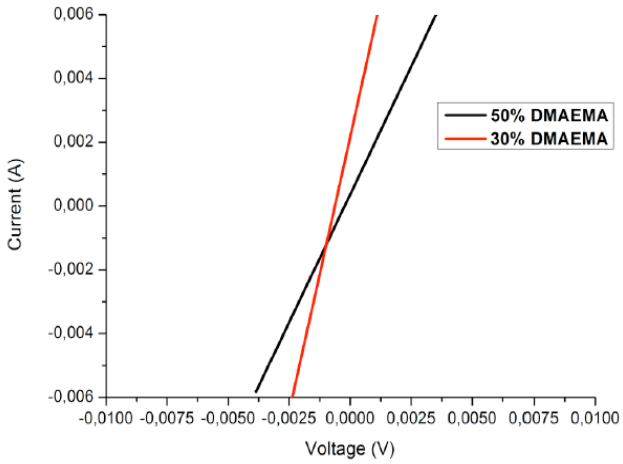


**Figure 53. Ohmic response of structures containing 30% and 50% DMAEMA. (Terzaki, Gaidukeviciute et al. 2011)**

These results suggest that the resistance increases with the decrease in DMAEMA content and this is attributed to the lower density of metal binding sites which results in smaller and less dense nanoparticles during the seeding process, and thus in a less uniform silver film after plating.

**Conclusions**

3D structuring and metallization of a novel metal-binding organic-inorganic hybrid material was investigated over the influence of the concentration of metal binding moieties (DMAEMA) on the 3D structure resolution, the material structurability and the metallization quality. A silver plating technique was optimized by investigating the metal seeding and reduction parameters. Three different metal plating protocols have been compared, and it was found that only one provides metallated structures exhibiting ohmic conductivity.

A good compromise for resolution and conductivity would be the addition of 30% DMAEMA in the hybrid photostructurable material which has 3.5 ± 0.2 Ohms resistance, accounting to conductivity $\sigma = (5.71 \pm 3.01) \cdot 10^{6}\ \Omega^{-1} \cdot m^{-1}$, only one order of magnitude far from the conductivity of pure silver ($\sigma = 6.3 \cdot 10^{7}\ \Omega^{-1} \cdot m^{-1}$). (Vasilantonakis, Terzaki et al. 2012), (Terzaki, Vasilantonakis et al. 2011)

One of the applications of the 3D conducting structures is the fabrication of three-dimensional photonic crystals with optical bandgaps. 3D metallic photonic crystals were fabricated and characterized at the near IR to optical region, with 600 nm periodicity and resolution below 100 nm and it was the first time 3D metallic structures having bandgap in the visible range are fabricated. Some of the applications that they can be used are in anti-reflection coatings and efficiency improvement filters for imaging and photovoltaics. (Vasilantonakis, Terzaki et al. 2012)

## 4.2 Directed 3D patterning of self-assembled peptides on hybrid microstructures and further metallization

As previously mentioned, Scheibel et al (Thomas Scheibel 2003) encountered a difficulty in measuring the conductivity of metallized self-assembled amyloid fibrils, due to failure of the fibrils to bridge the gap between two electrodes. This problem could be confronted by taking the following challenges:

- Positioning
- Controlled assembly

Thus, the strategy followed was a combination of self-assembly and laser technology. Metal-binding amyloid peptides that have the ability to self-assemble were oriented over 3D polymeric structures fabricated with DLW.
Since it was shown that the previously studied NSGAITIG peptide fibrils as well as CSGAITIG can bind to gold ions, they were used for integration on the primary 3D scaffolds that were previously covered with a gold tetrachloroaurate salt layer. NAGAITIG, was used as a control peptide due to insertion of a neutral amino acid, alanine in the position of the nucleophilic serine, keeping the rest of the sequence the same. (Tamamis, Kasotakis et al. 2009), (Kasotakis, Mossou et al. 2009).

The hybrid organic-inorganic material used for Direct Laser Writing had molar ratios 7:3 for MAPTMS/ZPO and 3:7 for DMAEMA/MAPTMS. The photoinitiator used was 4,4-bis(diethylamino) benzophenone at a 1% w/w concentration. After DLW processing, the sample was developed and the material not exposed to the laser radiation was removed by immersion in a 7:3 isopropanol/1-propanol solution.

**Results - Discussion**

**Structure functionalization with peptide fibrils**

The 3D structures were initially decorated with gold ions ($HAuCl_4.3H_2O$). Fibrils of NSGAITIG (aged for 2 and 10 days), of CSGAITIG as well as NAGAITIG control peptide fibrils (both aged for 1 month) were incubated on the anionic gold coated 3D polymeric structures in 3mg/ml concentration.

The structures were covered with self assembled NSGAITIG and CSGAITIG fibrils connecting the 5μm distance between them, while in the case of the control peptide there was no evidence of fibril attachment on the structures' surface. Even if the peptide fiber incubation time was 50 minutes for all the samples, in the case of the less mature solution of NSGAITIG the connections were fine and wire-like while where the more mature solution was used the connections seemed to form sheets.

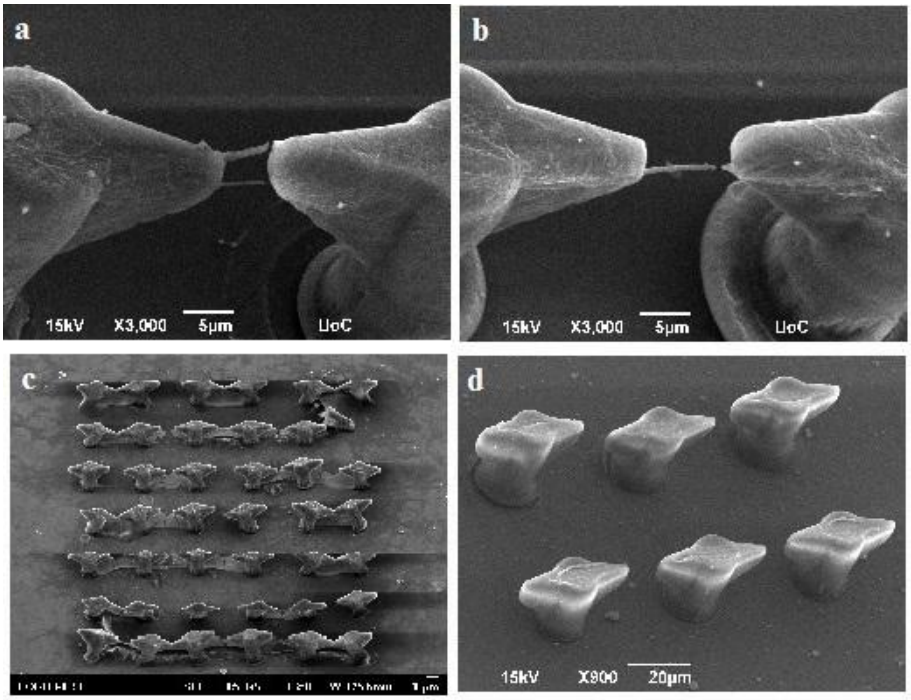


**Figure 54. 3D polymeric structure functionalized with 2 days aged NSGAITIG (a and b), 10 days aged NSGAITIG (c) and the non-covered sample of NAGAITIG peptide fibrils aged for one month (d)**

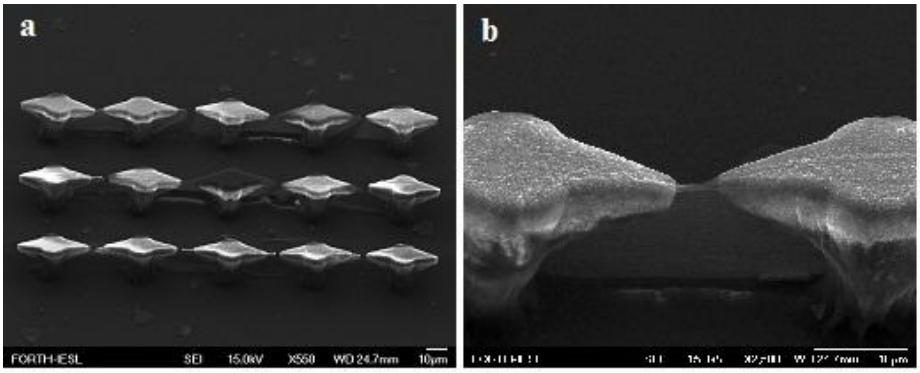


**Figure 55. SEM figures of 3D polymeric structure functionalized with CSGAITIG peptide fibrils**

### Structure functionalization with gold templated peptides

The peptide fibrils used were the NSGAITIG and CSGAITIG which were initially gold templated. In an eppendorf 20 μl of $HAuCl_4$ $3H_2O$ aqueous solution in 10 mM concentration were added with 10 μl of the peptide fibrils (1mg/ml) and incubated for 50 minutes in vortex. Afterwards 23 μl of the solution were incubated over the 3D structures for 35 minutes. A 10μl droplet of sodium citrate (74.8mM) was added for 45 minutes without removing the droplet of gold solution. Finally the samples were copiously washed with distilled water.

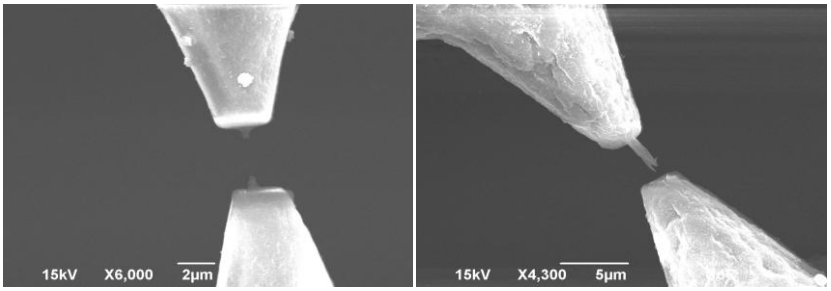


**Figure 56. SEM figures of NSGAITIG (left) and CSGAITIG (right) functionalized 3D structures**

According to the above SEM figure the gold metalized peptide fibrils formed bridges connecting the 3 μm gap between the structure's branches. Focusing the SEM's electron beam on the fibril connections provoked melting appearing as discontinuities of the bridges.

**Structure decoration with peptide fibrils and further metallization with silver**

3D structures were covered with NSGAITIG and CSGAITIG (3mg/ml) fibrils forming bridges between the branches and further metalized with silver nanoparticles. EDS analysis on the fibril connections proves the binding of silver by the peptide. The connection was broken while focusing the electron beam on the peptide fibers in order to acquire the EDS diagram.

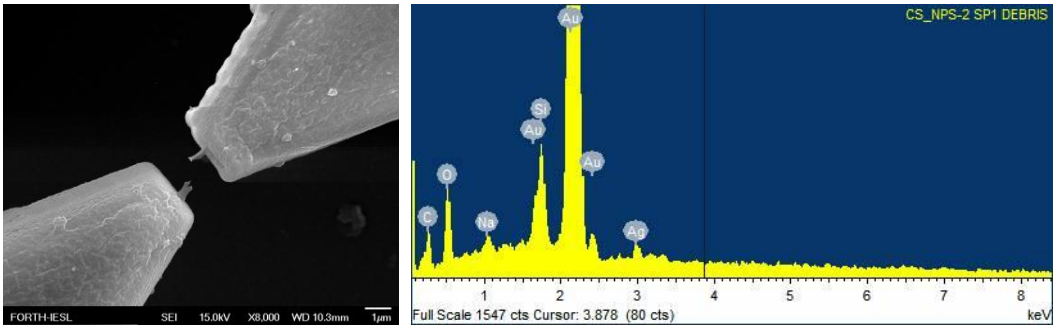


**Figure 57. TEM figure of CSGAITIG functionalized 3D structures and EDS diagram on the fibril connection**

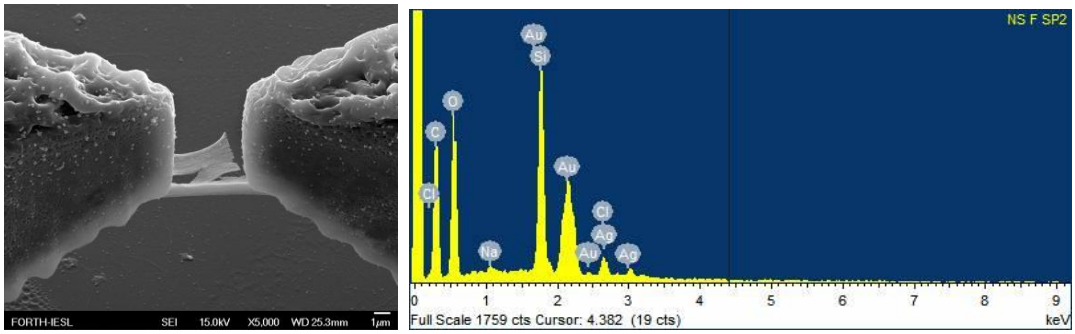


**Figure 58. TEM figure of NSGAITIG functionalized 3D structures and EDS diagram on the fibril connection**

### Conductivity measurements of metal-binding amyloid peptide fibrils

For measuring the conductivity of metal-binding peptide fibrils an arrangement illustrated by the following scheme was used.

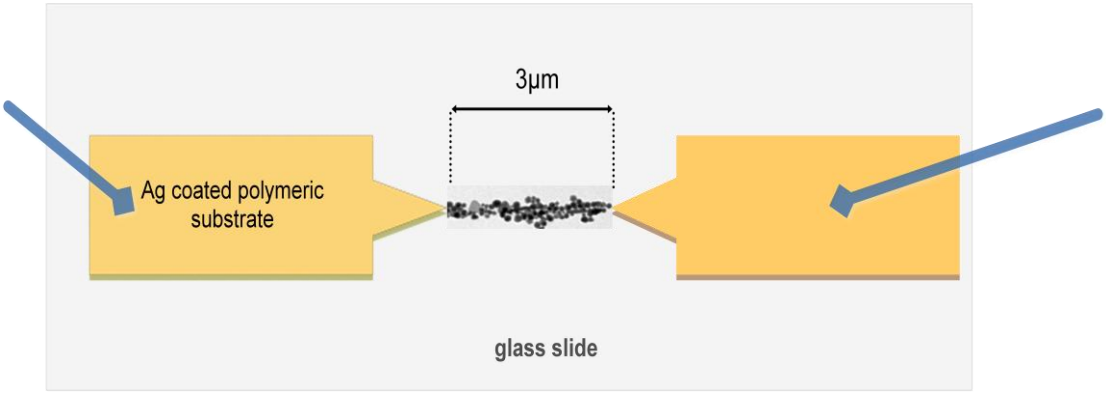


**Figure 59. Cartoon for conductivity measurements of metal binding peptide fibrils**

A droplet of the metal-binding peptide CSGAITIG in a concentration of 3mg/ml being aged for several days was deposited on large 3D conducting structures, which were produced with electroless plating technique described in the following chapter. After the amyloid fibrils bridged the gap between the structures, the structure was further metalized with gold ions which were further reduced to nanoparticles. The needles of the equipment used for conductivity measurements caused a slight dislocation of the structures resulting in breaking the fibril connections between the structures. Conductivity measurements of the system has to be further investigated.

### Conclusions

Combining self-assembly and laser technology, metal-binding amyloid peptides having the ability to self-assemble were oriented over 3D polymeric structures fabricated with DLW. In the range of 3mg/ml concentrations and deposition times of approximately 1 hour wire-like connections between structures were observed. For more concentrated peptide solutions or for longer incubation times sheet-like

connections were observed. Bridges of gold - metalized peptide fibrils can be fabricated between the polymeric structures; moreover, we have proved that gold-nanoparticle covered 3D structures can be decorated with peptide fibrils and be subsequently metallized with silver ions.

The orientation of conductive peptide fibrils between 3D structures could set the basis for the fabrication of a biosensor where the peptide plays both the role of the sensing and the recognition element. This could be achieved by depositing the sensing element on the fibril functionalized structure and after following the metallization process the voltage difference could be measured between the structures. However, the achievement of this set-up goes beyond the scope of the present thesis and has to be studied in the future.

## 5. Applications in 3D patterning of self-assembled peptides on hybrid structures – Part 2: Scaffolds for hard tissue engineering

### 5.1 Novel material fabrication and characterization of their mechanical properties and biological response

The following work focuses on the investigation of the mechanical properties of three novel materials of different chemical compositions and the evaluation of the biological response of pre-osteoblastic cells on them, aiming to bone-tissue regeneration. As discussed previously, autograft and allograft bone repair have some limitations including the high cost, the variability in osteogenic capacity, the morbidity (in the case of autografts) and the risk of immunogenic rejection and disease transmission (in the case of allografts). To overcome these limitations synthetic bone-graft substitutes have been developed as an alternative (Khan, Yaszemski et al. 2008), focusing on the parameters that can influence the cellular response on a fabricated scaffold. These are the material chemistry, the interconnectivity, its mechanical properties, the cell seeding density, the various growth factors, material porosity and pore size. (Kim, Dean et al. 2011). According to previous studies, continuous pore geometry in scaffolds has shown a higher cell ingrowth depth compared to scaffolds with random pore architecture. (Lee, Wang et al. 2010). This is attributed to the fact that pores are not only necessary for allowing migration and proliferation of osteoblasts, mesenchymal cells and vascularization, but also for improving the mechanical interlocking between the implant biomaterial and the surrounding natural bone. (Karageorgiou and Kaplan 2005). Thus, muti-photon polymerization technique was used allowing the fabrication of scaffolds with controlled geometry in three dimensions.

- **Material characterization for their mechanical properties**

The mechanical and chemical characteristics of the primary scaffold are important in a way that cells seeded on scaffolds can recognize differences related to the materials' properties and subsequently change their response and functions. Thus, the suitability of materials of different chemical composition that can be structured in complex, 3D geometries using DLW for bone tissue scaffolds was investigated. First, the synthesis and characterization of chemical and mechanical properties was described of three different hybrid materials:

a) poly(2-(dimethylamino)ethyl methacrylate) (PDMAEMA)
b) methacryloxypropyl trimethoxysilane (MAPTMS) + Zirconium propoxide (ZPO)
c) 50 mol% MAPTMS + ZPO + 50 mol% DMAEMA

Nanoindentation tests were performed by Prof. C.Charitidis group (School of Chemical Engineering, National Technical University of Athens) in order to estimate the hardness and the elastic modulus of the materials.

The hardness and the reduced modulus of the hybrid samples and how they are affected by humidity when submerged into the cell culture medium was investigated, resulting in sample softening in the case of the hybrid containing only MAPTMS and ZPO, which means that it gets affected by water absorption. A totally different behavior is observed for 50% DMAEMA composite, which exhibits the best

mechanical properties after submersion of the sample into the cell culture medium, having a hardness of 0.64 GPa and reduced modulus 7.98 GPa, values which are very close to the ones measured in the previous experiments with nanoidentation technique. The observed hardening results indicate sufficient plastic behavior of the material. (Terzaki, Kissamitaki et al. 2013)

According to previous studies, typical values of nanoindentation tests on bovine cortical bone are: H = 0.5GPa, E = 16 Gpa (Lau, Lau et al. 2010). While nanoindentation tests on human bone specimens (Hengsberger, Kulik et al. 2002) of compact and trabeculae femoral bone dried and under physiological conditions had the following range of values:

Dry conditions: H = 0.48 – 1.25 Gpa , E = 11.06 - 31.6 GPa

Physiological conditions: H = 0.29 - 0.95 Gpa , E = 7.4 - 18.5 Gpa

Amounts that are related to the mechanical properties measured for the 50% DMAEMA-composite material.

- **Material characterization for their biological response**

Next, 2D films of the above materials were fabricated for the investigation of cell viability and proliferation of MC3T3 pre-osteoblastic cells on them. Additionally, the influence of the materials' chemical composition on cell proliferation was explored. The exhibited strong pre-osteoblastic cell adhesion of all the three hybrid materials investigated and mostly of the 50% DMAEMA scaffolds, together with the observed spread cell morphology from the first hour of observation and the proliferation increase after 3 and 7 days, reflected the biocompatibility of the hybrid scaffolds proving that they could be used for bone-tissue regeneration. **(Terzaki, Kissamitaki et al. 2013)**

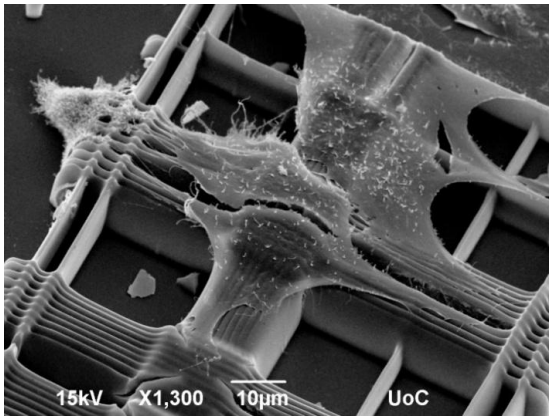


**Figure 60. SEM images of MC3T3 pre-osteoblastic cells on 3D hybrid structures 2 hours after seeding, where already extended protrusions can be observed.**

## Conclusions

Fabrication and selection of an optimal scaffold was achieved, where 50% DMAEMA hybrid material exhibited good mechanical properties, close to the ones of human cortical bone and strong biological response. Therefore this material can be used as a novel material for 3D scaffold fabrication in bone tissue engineering applications. More details over the results can be acquired in: Terzaki, K., Kissamitaki, M., et al.

(2013). "Pre-osteoblastic cell response on three-dimensional, organic-inorganic hybrid material scaffolds for bone tissue engineering." Journal of Biomedical Materials Research Part A.

## 5.2 Mineralized self-assembled peptides on 3D laser-made scaffolds: A new route towards 'scaffold on scaffold' hard tissue engineering

A study in hard tissue regeneration engineering is being presented where a new approach based on the mineralization of 3D scaffolds is being proposed. Acidic amino acid containing self-assembling peptides were designed having the ability to bind calcium, as it happens in nature, (the epitaxial growth of aragonite crystals between the organic matrix of nacre). The ability of these peptides to support cell attachment and proliferation when coupled on a hybrid organic-inorganic structurable material and subsequently mineralized with calcium phosphate was further investigated.

### 5.2.1 Design of bi-functional peptides for bone tissue engineering scaffolds

Initially, the need for amyloid fibrils that can have bi-functional properties led to the design of amyloid peptides containing aspartic acids on their sequence. The idea was based on the well-studied octapeptide NSGAITIG that is able to self-assemble into amyloid-type fibrils and to nucleate metal nanoparticles (Papanikolopoulou, Schoehn et al. 2005; Kasotakis, Mossou et al. 2009), as well as to maintain its amyloidogenic properties when the asparagine residue (N) is substituted with another amino acid (Tamamis, Kasotakis et al. 2009). Aspartate residues serve in nature as nucleation sites for calcium ions on the proteins, where two aspartate ligands (being acidic) are needed per one calcium ion, which has an electric charge of +2 (Mann 2001). In these proteins serine residues are also found next to the aspartate residues. Keeping in mind the above facts asparagine was substituted with aspartate (D) resulting in the peptide sequence: DSGAITIG and another peptide sequence was designed targeted to calcium binding containing 2 aspartic acids: DDGAITIG. The peptide sequence ASGAITIG including alanine, which is a small hydrophobic amino acid, was used as control sample for the following experiments.

Moreover a nonapeptide was designed adding one more aspartic acid in the sequence: DDSGAITIG and its detailed structural characterization, (cf. "Biofabrication" paper below) proved that retained amyloid-forming ability. The designed peptide sequences including serine residues and aspartic acids formed fibrils that could bind to the metal ions located on the surface of the hybrid scaffolds and could subsequently nucleate the deposition of calcium phosphate.

**Table 5. Calcium binding peptides for use as scaffolds for hard tissue regeneration**

| | | |
|---|---|---|
| **DS** | D-S-G-A-I-T-I-G | $H_2N$-Asp-Ser-Gly-Ala-Ile-Thr-Ile-Gly-$CONH_2$ |
| **DD** | D-D-G-A-I-T-I-G | $H_2N$-Asp-Ser-Gly-Ala-Ile-Thr-Ile-Gly-$CONH_2$ |
| **DDS** | D-D-S-G-A-I-T-I-G | $H_2N$-Asp-Asp-Ser-Gly-Ala-Ile-Thr-Ile-Gly-$CONH_2$ |
| **AS** (Control | A-S-G-A-I-T-I-G | $H_2N$-Ala-Ser-Gly-Ala-Ile-Thr-Ile-Gly-$CONH_2$ |

| | | |
|---|---|---|
| peptide) | | |

**a) Amyloid-Forming Ability**

To determine whether the designed peptides conserved their ability to form amyloid fibrils, the peptide-lyophilized powders were dissolved in ultrapure water and followed by TEM over time. Each sample was also visually examined for an increase in viscosity, gel formation, or the appearance of a precipitate. Once a change was observed, aligned fibrils were prepared between two glass rods and examined by X-ray fiber diffraction.

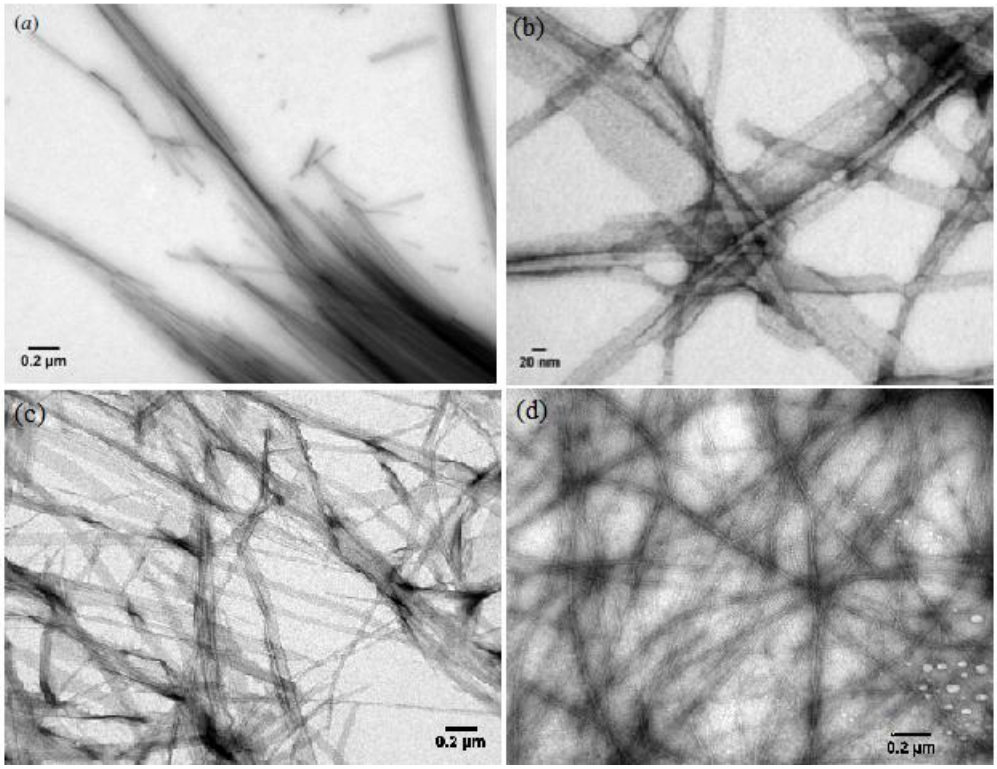


**Figure 61. TEM micrographs of 3mg/ml (a) DDSGAITIG, (b) DDGAITIG, (c) DSGAITIG and (*d*) ASGAITIG peptides aged for four days. The samples were stained with 1% uranyl acetate prior to imaging**

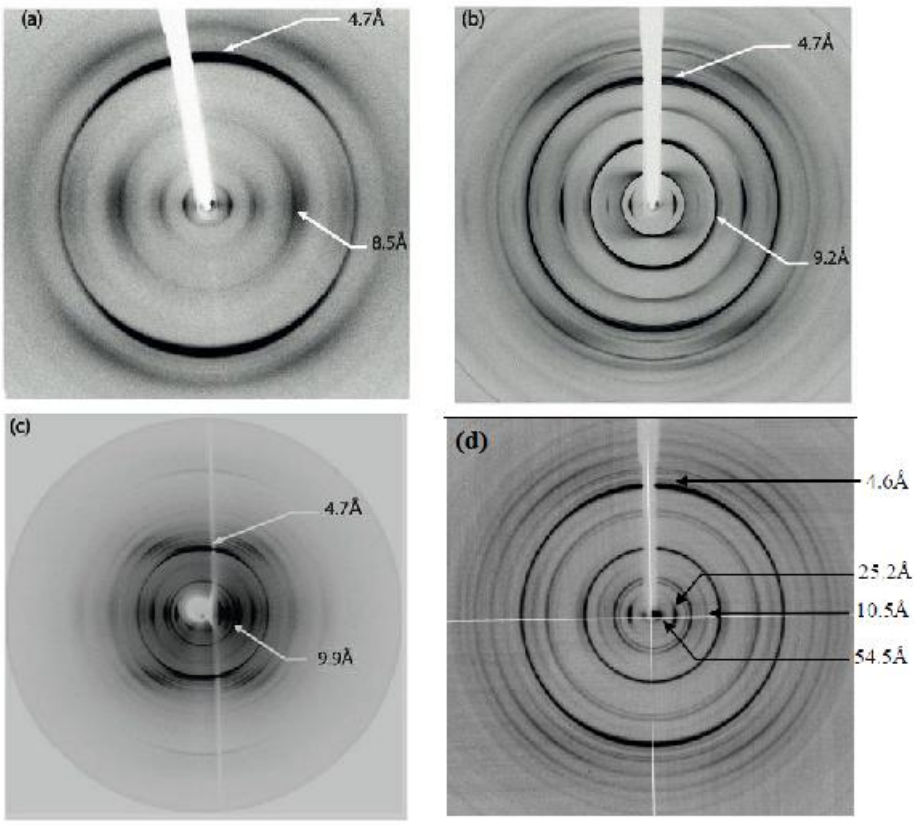


**Figure 62. X-ray diffraction patterns of a) DDSGAITIG, b) ASGAITIG, c) DSGAITIG, and d) DDGAITIG**

In the figures above TEM micrographs of the DDSGAITIG, DSGAITIG, DDGAITIG and ASGAITIG peptides after negative staining can be seen, where DSGAITIG and DDGAITIG form tapes with widths ranging from 15–75 nm. The peptide DDSGAITIG, which includes one extra amino acid in the octapeptide sequence, was found to retain the propensity to form straight aligned fibers with widths of around 50 nm arranged into bundles. A mixture of straight and twisted fibrils was observed for the ASGAITIG peptide having a diameter around 10 nm. The amyloid fibrils formed from all the peptides show the characteristic cross-beta x-ray diffraction
pattern having a 4.7 °A reflection corresponding to the hydrogen bonding distance between beta-strands and a ∼10 °A reflection corresponding to the intersheet packing distance. The DDSGAITIG fiber pattern is consistent with a tighter intersheet packing of 8.5 ° A. both the TEM and x-ray fiber diffraction data confirm that the designed peptides maintain the ability to self-assemble into amyloid-type fibers. The result is particularly significant for the DDSGAITIG peptide, since it proves that an extra aspartate residue can be accommodated at the N-terminus of the peptide building block.

**b) Templating of bi-functional peptide fibrils with metal nanoparticles**

- **Metallization of peptides with gold nanoparticles**

To assert the eventual metal-binding ability of the DDSGAITIG and DDGAITIG peptide sequences, the amyloid fibrils were metalized with gold, silver and platinum nanoparticles. The following figures show DDSGAITIG and DDGAITIG peptide fibrils templated with gold nanoparticles. No negative stain was used, thus the contrast comes solely from the metal particles.

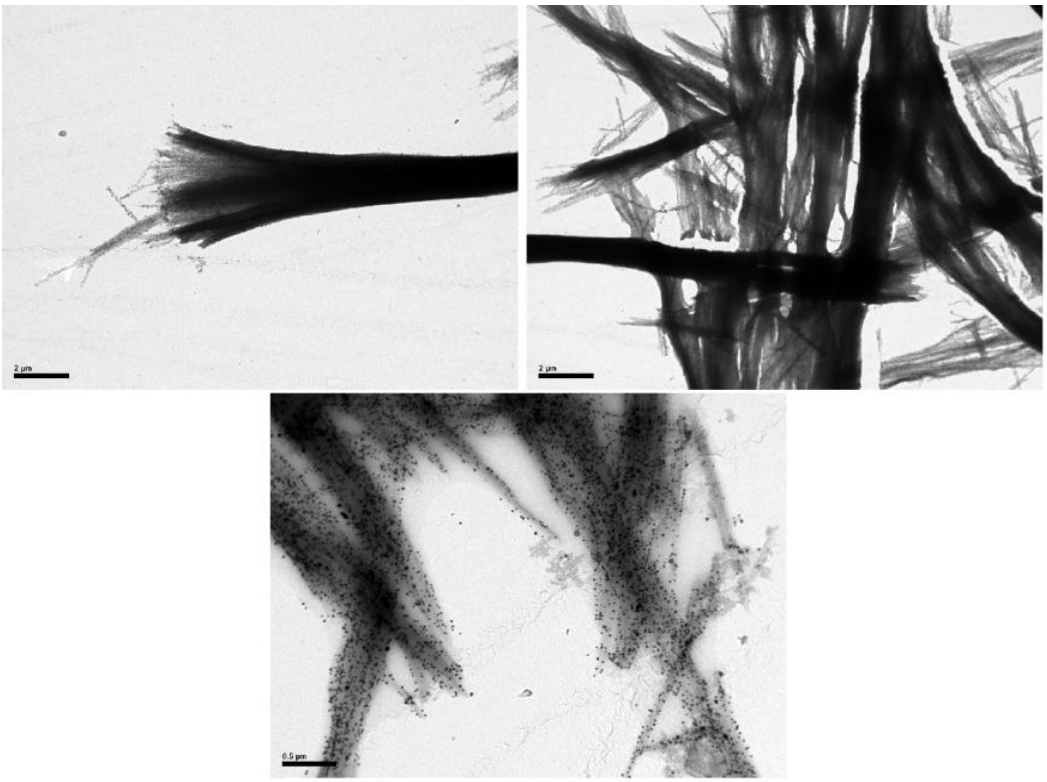

**Figure 63. TEM micrographs of DDSGAITIG peptide fibrils (0.6mg/ml) after incubating with a gold solution and reduction with 1% sodium citrate.**

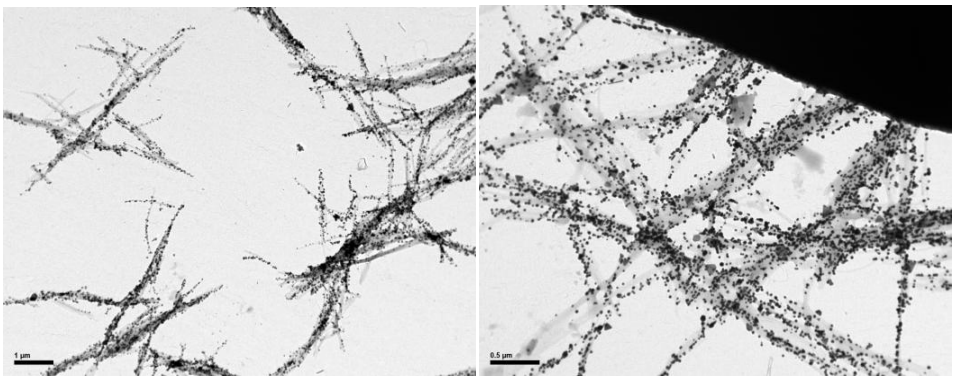

**Figure 64. TEM micrographs of DDGAITIG peptide fibrils (0.6mg/ml) after incubating with a gold solution and reduction with 1% sodium citrate.**

- **Metallization of peptides with silver nanoparticles**

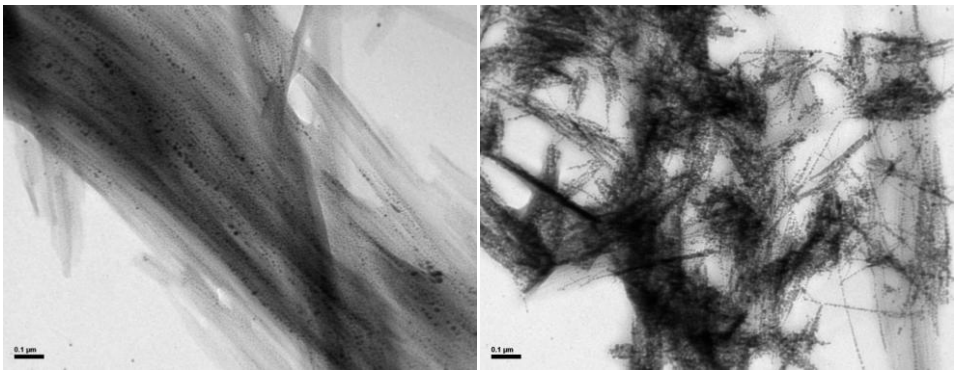

**Figure 65. TEM micrographs of (left) DDSGAITIG and (right) DDGAITIG peptide fibrils (2mg/ml) after incubation with a silver solution and reduction with 1% sodium citrate.**

- **Metallization of peptides with platinum nanoparticles**

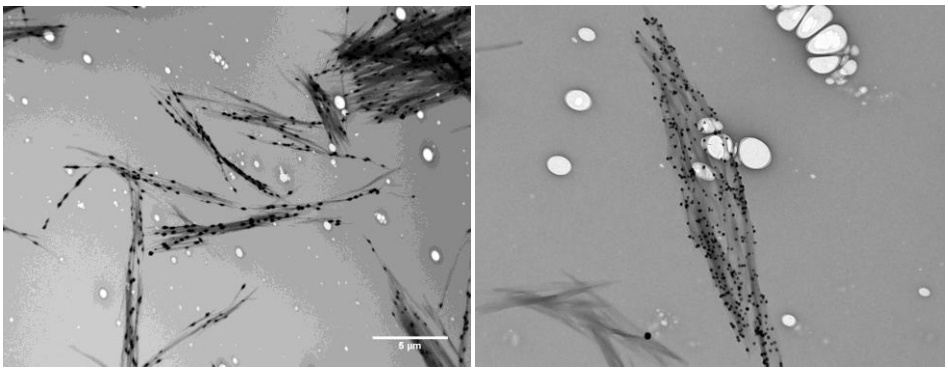

**Figure 66. TEM micrographs of (left) DDSGAITIG and (right) DDGAITIG peptide fibrils (1mg/ml ) after incubation with $K_2PtCl_4$ aqueous solution (0.02M) and reduction with ascorbic acid (0.15M)**

The fibrils formed of the peptide sequences DDSGAITIG and DDGAITIG were both uniformly covered with metal nanoparticles. Therefore, both DDSGAITIG and DDGAITIG peptide fibrils can act as templates for the nucleation of metal particles, and are appropriate for positioning onto gold decorated 3D structures.

**c) Mineralization with calcium phosphate on a holley grid**

The mineralization process followed and $CaCl_2$ and $Na_2HPO_4$ concentrations used on the peptide fibrils was the same as previously described for the DDS/DS/AS-GAITIG peptides. In the following figure the TEM images can be seen for the mineralized peptide fibrils where no negative staining was used, so the contrast comes solely from the mineral phase.

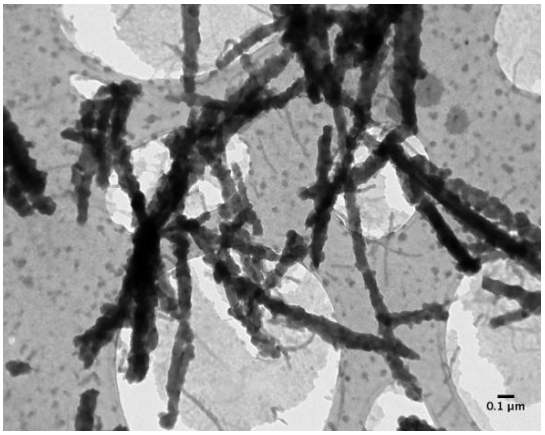


**Figure 67. TEM micrograph of DDGAITIG peptide fibrils incubated with CaCl2 and Na2HPO4 on holey grid**

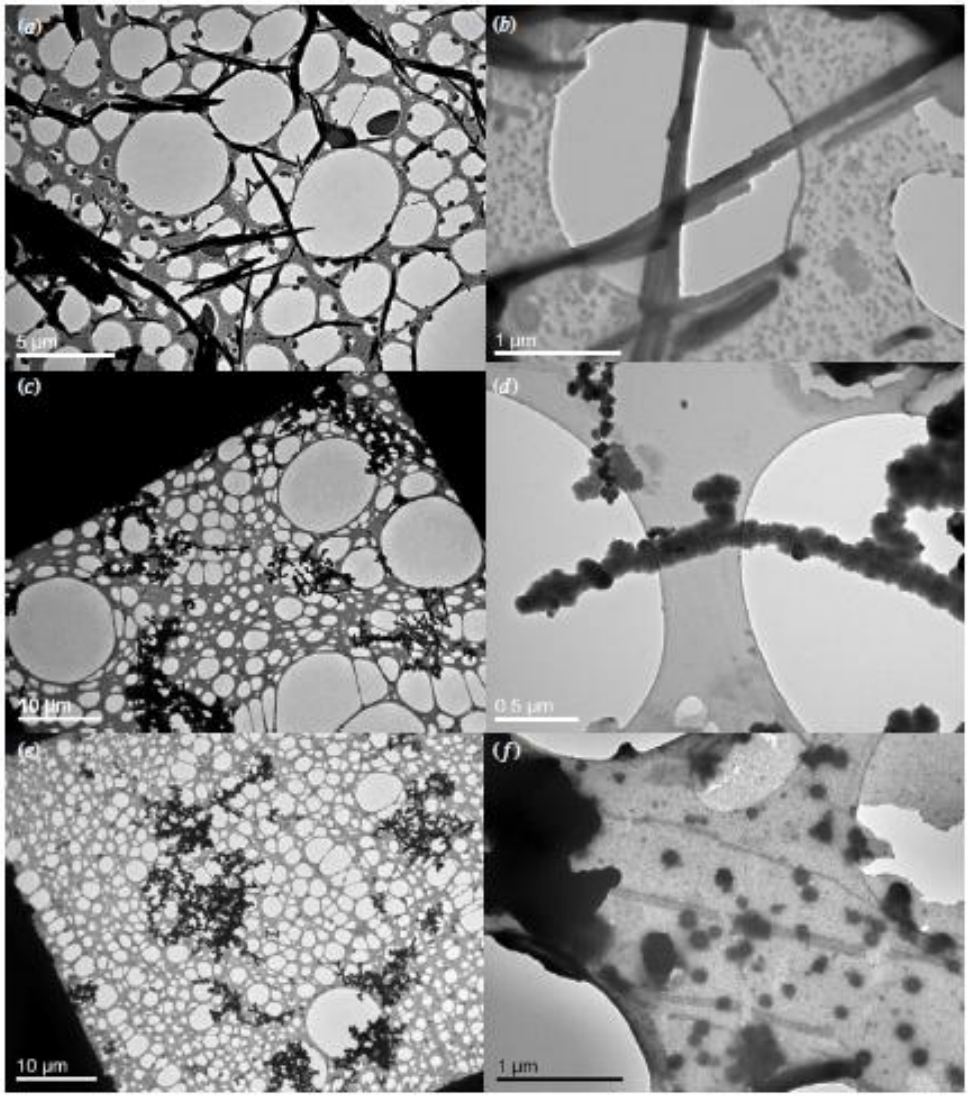


**Figure 68. TEM micrographs of peptide fibrils incubated with CaCl2 and Na2HPO4 on holey grids. (a), (b): DDSGAITIG fibrils, (c), (d): DSGAITIG fibrils, (e): ASGAITIG fibrils, and (f): ASGAITIG fibrils incubated with CaCl2 and Na2HPO4 on the grid and subsequently negatively stained.**

To evaluate the stoichiometric analysis of the mineral particles and their atomic mass ratio, EDXS analysis was used alongside with selected-area-electron diffraction (SAED), which provides information on the mineral morphology (crystal or amorphous), the crystal structure and orientation of the crystals. TEM images of the mineralized peptide fibrils were taken without negative staining, where the contrast comes solely from the mineral phase. For the DDSGAITIG, DDGAITIG and DSGAITIG peptides, fibrils covered with the mineral phase were observed. For the DDSGAITIG fibrils, a better and more homogenous coverage can be observed compared to the other peptide fibrils. Low amounts of background mineral particles (i.e. non-attached to fibrils) are observed for the DDSGAITIG peptide, while for the DSGAITIG and DDGAITIG peptides, a higher amount of background mineral coexists with those deposited on fibrils. For the ASGAITIG peptide, clusters of the mineral phase were observed, indicating absence of deposition on the fibrils. In order to verify the existence of the ASGAITIG fibrils on the sample, TEM micrographs were taken following additional negative staining. Amyloid fibrils were indeed observed, clearly segregated from the mineral phase, confirming absence of mineral deposition on the fibrils. EDXS analysis on the grid containing the DDSGAITIG peptide fibrils confirmed the presence of calcium and phosphate on this area (Konstantina, Erifyli et al. 2013). SAED performed on the DDSGAITIG mineralized peptide fibrils showed that the deposited mineral on the fibrils was characterized as amorphous calcium phosphate. These results confirm that the presence of aspartate residues is necessary for the nucleation of the calcium phosphate on the fibrils since no deposition was observed for the alanine-containing peptide.

From the moment that the DDSGAITIG peptide was characterized and was found to properly self-assemble and have a better coverage of the underlying fibril for both metal and mineral templating was chosen for the continuation of the study.

Additionally, a higher resolution image below taken with the HRTEM microscope confirms the choice of this peptide, where a very well defined coverage of the DDSGAITIG peptide fibrils is being observed where the fringes show the periodicity of the calcium particles being at around 1nm, which is comparable to the interstrand spacing between two b-strands.

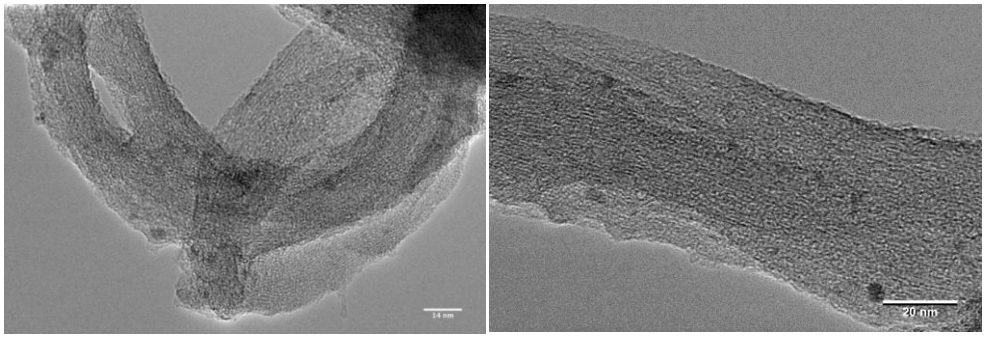


**Figure 69. HRTEM pictures of mineralized DDSGAITIG peptide without negative staining**

**d) Fibril deposition on the 3D structures and subsequent mineralization with calcium phosphate**

In the meantime, the previously studied hybrid photostructurable material for its good mechanical properties and its strong biological response on pre-osteoblastic cells (Terzaki, Kissamitaki et al. 2013) was used to fabricate three-dimensional scaffolds with DLW which were subsequently decorated with gold ions. The bi-functionality of the DDSGAITIG peptide fibrils makes them appropriate for positioning onto gold decorated 3D structures that can subsequently act as secondary scaffolds for the deposition of calcium phosphates following a 'scaffold on scaffold approach'.

In the SEM pictures below the primary 3D scaffolds can be seen after DLW having 3μm and 5μm distances between the branches in the horizontal and vertical direction respectively.

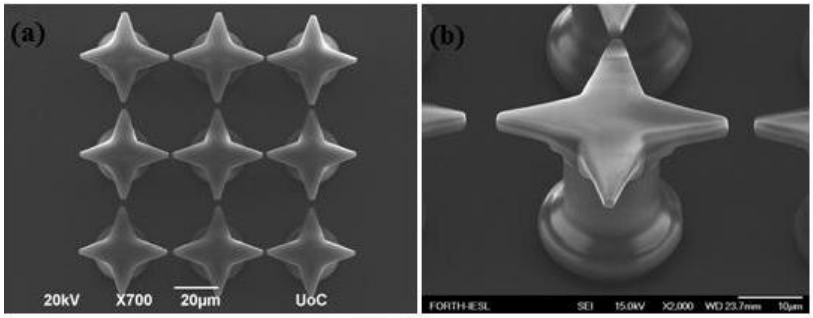


**Figure 70. SEM images of primary 3D structures fabricated with DLW**

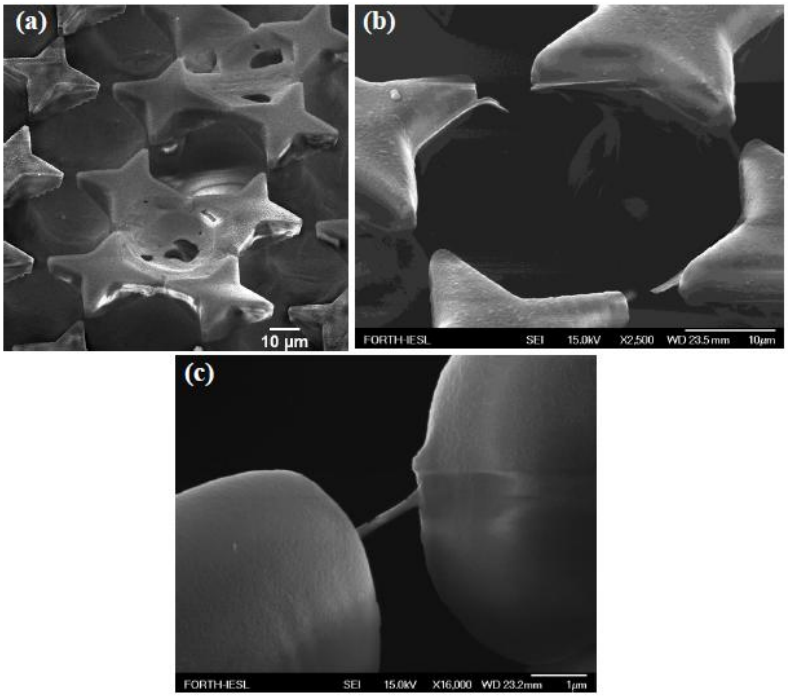


**Figure 71. Deposition of DDSGAITIG peptide fibrils on primary 3D scaffolds seeded with gold tetrachloroaurate. In a, the peptide solution was left on the scaffolds for one hour before rinsing, whereas in b and c it was left for 50 minutes.**

The fibrils attached to the primary scaffolds form bridges or sheets depending on the incubation time. They were further incubated with $CaCl_2$ and $Na_2HPO_4$. Sheets with fibrous topography and bridges connecting the structures are observed in the SEM images below.

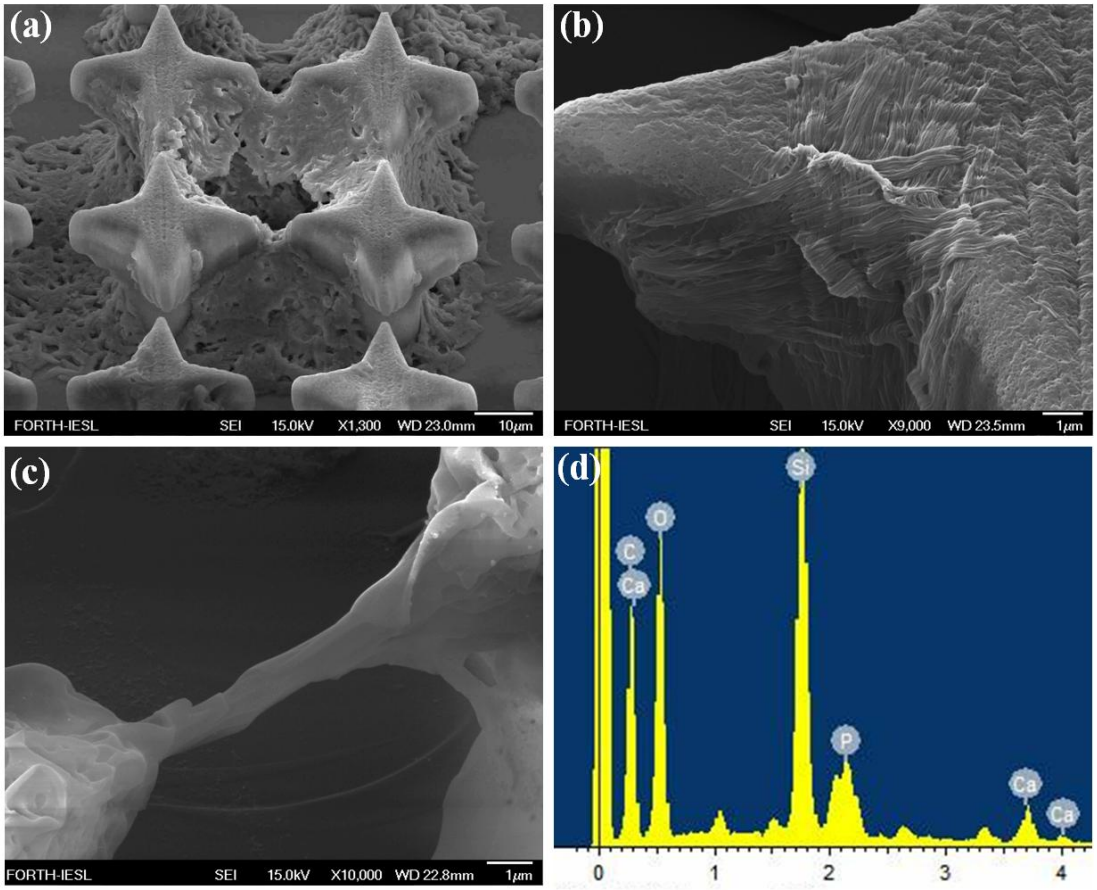


**Figure 72. SEM images of peptide fibril-covered, calcium-mineralized 3D structures (*a*), (*b*), (*c*). In (*d*), EDS analysis on the bridge formed between structures of figure 4(*c*) is shown**

EDXS analysis on the sheets and bridges connecting the structures confirmed the deposition of calcium and phosphate on this area. The stoichiometric ratio of Ca/P was found to be 1.35, which is close to the ratio of the octacalcium phosphate (1.33).

For the purposes of studying the pre-osteoblastic and bone marrow mesenchymal stem cell adhesion and growth, primary scaffolds with woodpile shapes were fabricated. The following figures show woodpile 3D scaffolds functionalized with DDSGAITIG peptide fibrils and mineralized with 1 M $CaCl_2$ but different concentrations of $Na_2HPO$, keeping the rest of the mineralized process the same for both of the samples.

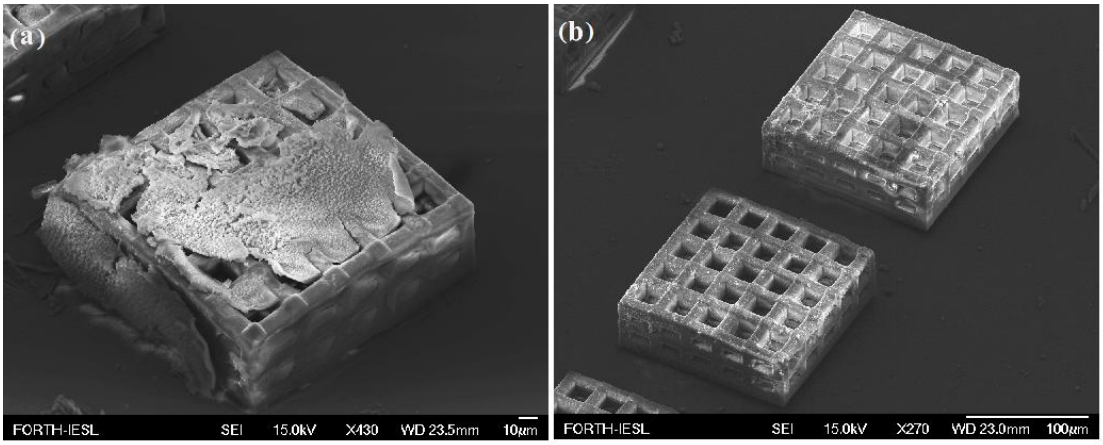


**Figure 73. SEM images of biomineralized 3D structures with 1M $CaCl_2$ and $Na_2HPO_4$ concentration a) 0.6M and b) 0.06M**

We can observe that in the case of higher concentration of $Na_2HPO_4$ the minerals almost fully covered the woodpile shaped structure filling its holes. In further experiments rods were formed in the peptide sheets connecting the structures, as it can be seen at the following SEM images. EDXS analysis on the mineral structures showed very high peaks for phosphate and almost no calcium peak.

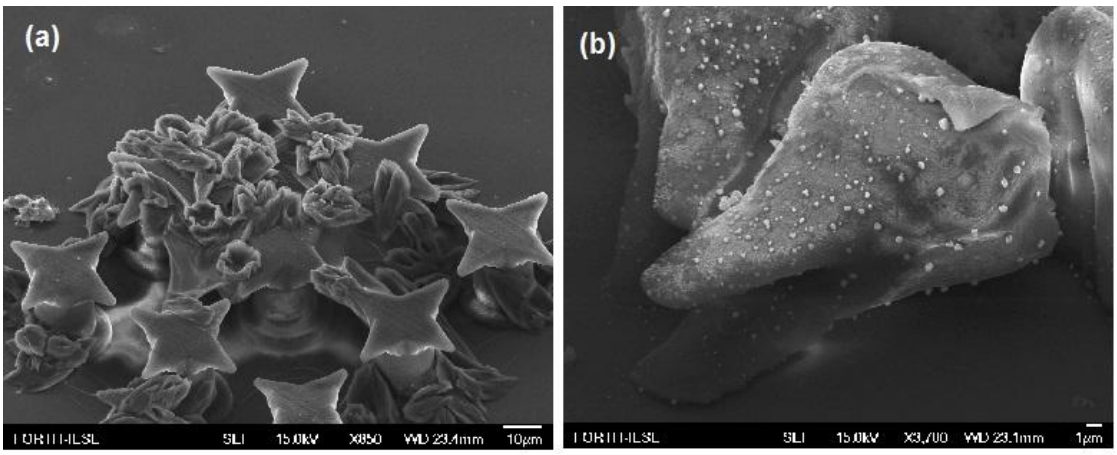


**Figure 74. SEM images of biomineralized 3D structures with 1M $CaCl_2$ and $Na_2HPO_4$ concentration a) 0.6M and b) 0.06M**

According to the above observations, the concentration used for functionalizing the 3D scaffolds was 0.06M. Additional experiments on 3D structures mineralized with 1M $CaCl_2$ and 0.06M $Na_2HPO_4$ gave the following results.

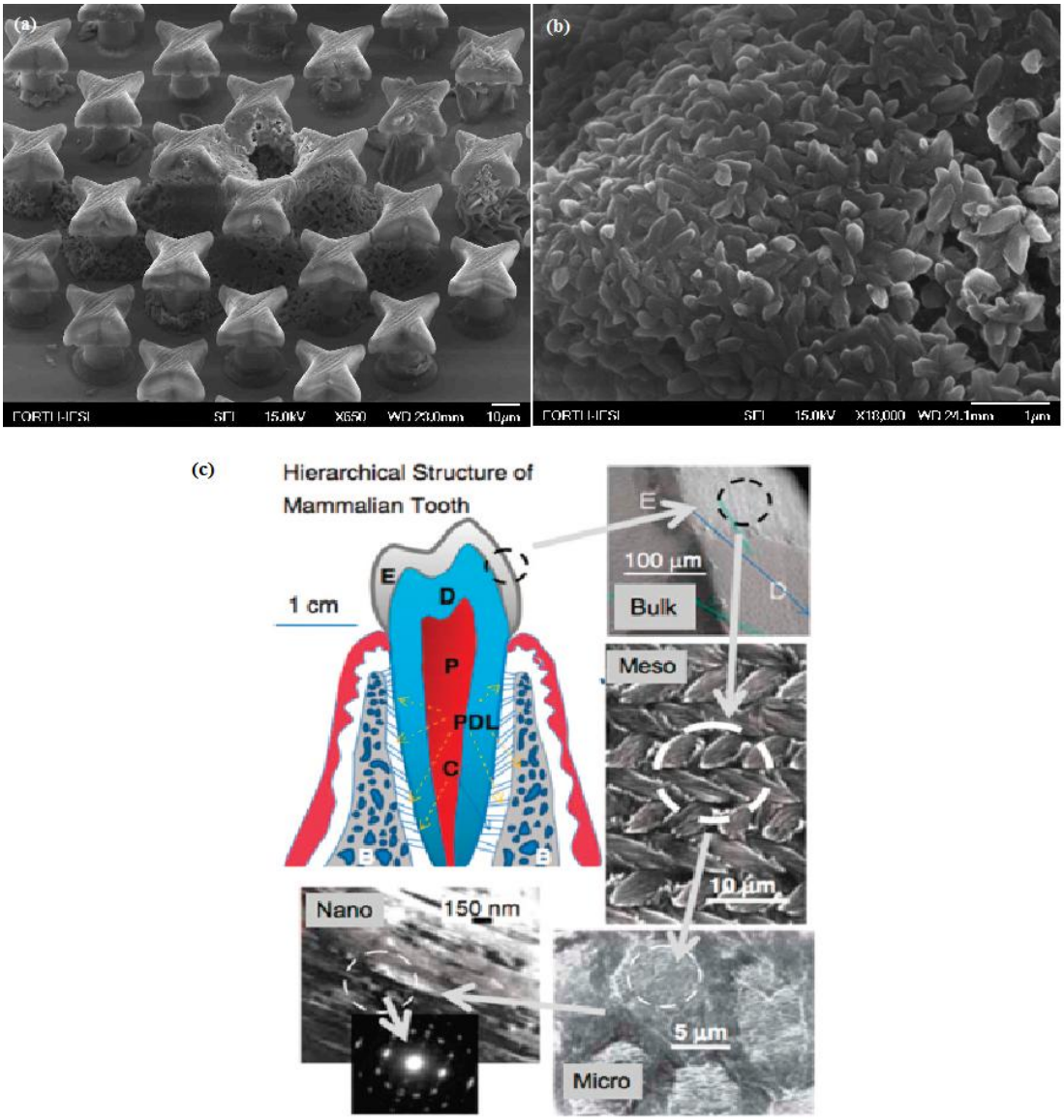


**Figure 75. a) SEM images of peptide fibril-covered, calcium-mineralized 3D structures, b) higher magnifications of the same figure, c) morphology of dental enamel (Palmer, Newcomb et al. 2008)**

According to the above SEM images a closer look to the mineral interweaving rod formations between the structures can reveal a great similarity to the morphology of dental enamel having similar interweaving bundles of crystallites.

Concluding, by controlling the mineralization conditions, including calcium phosphate concentration and incubation time, mineral structures similar to human enamel of the mesoscale can be fabricated. These structures coalesce to form a tough tissue, which can withstand high forces and resist crack fatigue damage.

### 5.2.2 Cell response on mineralized self-assembling peptides on top of a hybrid scaffold

The suitability of these peptides to support cell attachment and proliferation when coupled on the hybrid organic–inorganic material covered with mineralized peptide fibrils was investigated.

Cell culture studies with MC3T3-E1pre-osteoblastic cells on functionalized 3D scaffolds and material surfaces showed that the mineralized peptide, strongly supports cell adhesion, a proliferation increase after 3 and 7 days in culture, and exhibits a statistically significant increase of biomineralization after two weeks on material film surfaces. This strategy can be proposed as a 'scaffold on scaffold' approach for hard tissue regeneration. (Terzaki, K., Kalloudi, E., et al. 2013)

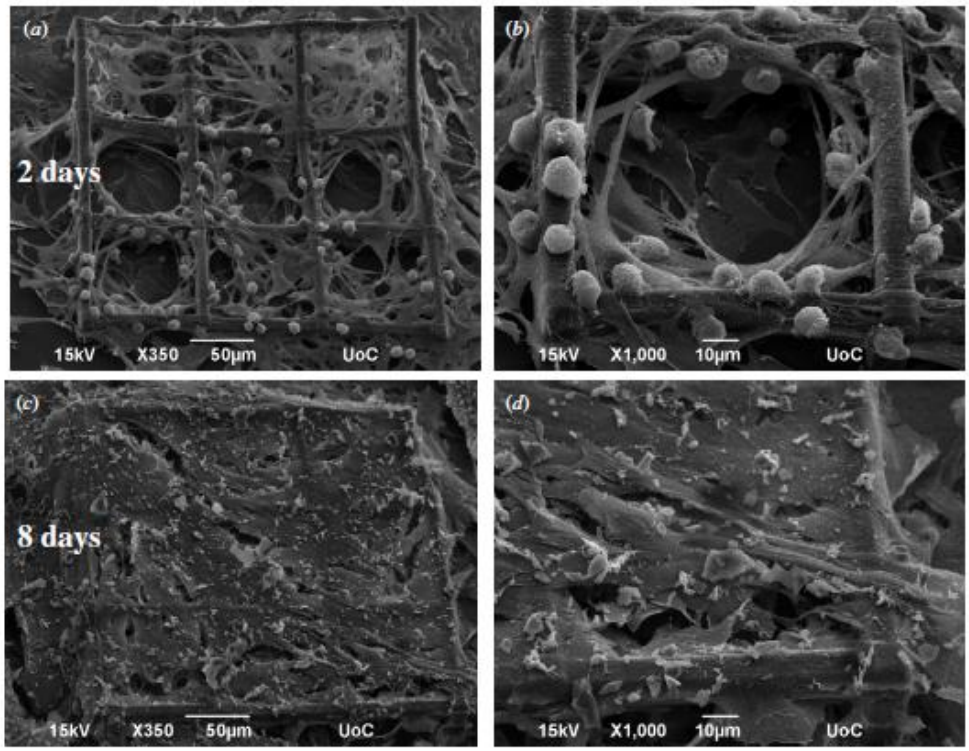


**Figure 76. SEM images showing pre-osteoblastic cells cultured on DDSGAITIG peptide-functionalized and mineralized 3D woodpile-shaped scaffolds. Cells adhere well after 2 days as shown in a 350-fold (a) and a 1000-fold magnification (b), and cell nuclei are visible as white spheres. After 8 days in culture, cell proliferation increases and cells form dense layers covering the scaffold's pores as shown in a 350-fold (c) and a 1000-fold magnification (d).**

### Conclusions

Bi-functional peptide sequences were designed which can nucleate both metal nanoparticles and calcium phosphate, forming amyloid fibrils.

Using a biomimetic approach, similar to the example of nacre a new strategy for hard tissue engineering is proposed based on the mineralization of functionalized scaffolds. The primary scaffolds of an amine-containing photosensitive hybrid material can immobilize gold ions on its surface. DDSGAITIG bi-functional self-assembling peptide, interacts with the gold ion layer of the primary scaffold, acting as a secondary

scaffold for the deposition of calcium phosphate. Strong cell adhesion and proliferation on material surfaces and onto 3D scaffolds was observed as well as a significant increase of calcium production in the extracellular matrix of the cells. This scaffold fabrication strategy opens new possibilities for future development of complex geometries and architectures for hard tissue regeneration.

## 6. Photocrosslinking of protein microstructures: evaluation of processability and bioactivity

The precise control of the cellular architecture is vital for creating engineered tissue constructs. Cell adhesion, proliferation and differentiation *in vitro* can be guided by topographical and chemical cues. Thus, photocrosslinked microscale protein topographies with biological activity offer a great opportunity to control the spatial organization of cells by affecting the cell–matrix interactions in cell culture (Pins, Bush et al. 2006), (Seidlits, Schmidt et al. 2009).

The parameters of photocrosslinking with multiphoton absorption of proteins by fabricating 2D surface structures of the model proteins avidin, bovine serum albumin (BSA) and biotinylated bovine serum albumin (bBSA) were evaluated. The two-photon absorption induced photo-crosslinking of proteins with the non-toxic biomolecule flavin mononucleotide (FMN) as a photosensitizer. Furthermore, their biofunctionality and integrity were tested. The results were compared with structures fabricated in VTT Research Centre of Finland with a picosecond pulsed Nd:YAG microlaser.

### Cross-linked protein microstructures

Some proteins form inter- and intramolecular covalent crosslinks via nonlinear excitation of a suitable photosensitizer. The crosslinking is believed to proceed either via free radical formation or via singlet oxygen generation depending on the sensitizer, the reaction conditions, the wavelength and intensity of the exciting light. The singlet oxygen or the radicals interact with the photooxidizable amino acid residues (such as tyrosine, cysteine, histidine and tryptophan) in one protein molecule to form products that react with residues in another protein molecule to promote crosslinking (Verweij, Dubbelman et al. 1981). Biomolecule flavin mononucleotide (FMN) has been shown to sensitize crosslinking by both the mechanisms depending on the pH conditions. The FMN-sensitized photooxidation at pH < 8 is probably mediated not by singlet oxygen mechanisms, but by the formation of a triplet state FMN, that can abstract an electron (or an H atom) from the protein to generate radicals of the sensitizer and the protein (Spikes, Shen et al. 1999),(Shen, Spikes et al. 2000). The excitation of FMN to triplet state can also be achieved via multi-photon absorption inducing photocrosslinking.

Photocrosslinked nano- and microscale protein topographies with biological activity offer a great opportunity to control the spatial organization of cells by affecting the cell-matrix interactions in cell cultures.

Sub-micrometer and micrometer scale structures were fabricated from several different compositions of protein and photosensitizer by varying the average laser

power and scanning speed in order to determine the optimal process parameters for efficient photocrosslinking.

The retention of bioactivity of the crosslinked protein structures was shown by fluorescence imaging of immobilized biotin or streptavidin conjugated fluorescence labels. The surface topography and the resolution of the protein patterns fabricated with the femtosecond Ti:Sapphire laser were compared to the results obtained with a Nd:YAG laser. Similar grain characteristics and minimum feature sizes were achieved with both laser sources.

**Results - Discussion**

Different protein and AFM concentrations as well as average laser power and scanning speed values were tested to determine the range of fabrication conditions suitable for protein crosslinking.

The Ti:Sapphire laser allowed the fabrication of the protein patterns with scanning speeds approximately 12 to 20fold faster in comparison to the scanning speed used with the Nd:YAG laser. This can be attributed to the much higher repetition rate (75 MHz vs. 8 kHz) and approximately 90fold higher peak power of the Ti:Sapphire laser as compared to the Nd:YAG laser, which enables more efficient crosslinking of proteins by creating favourable circumstances for the two-photon absorption to occur.

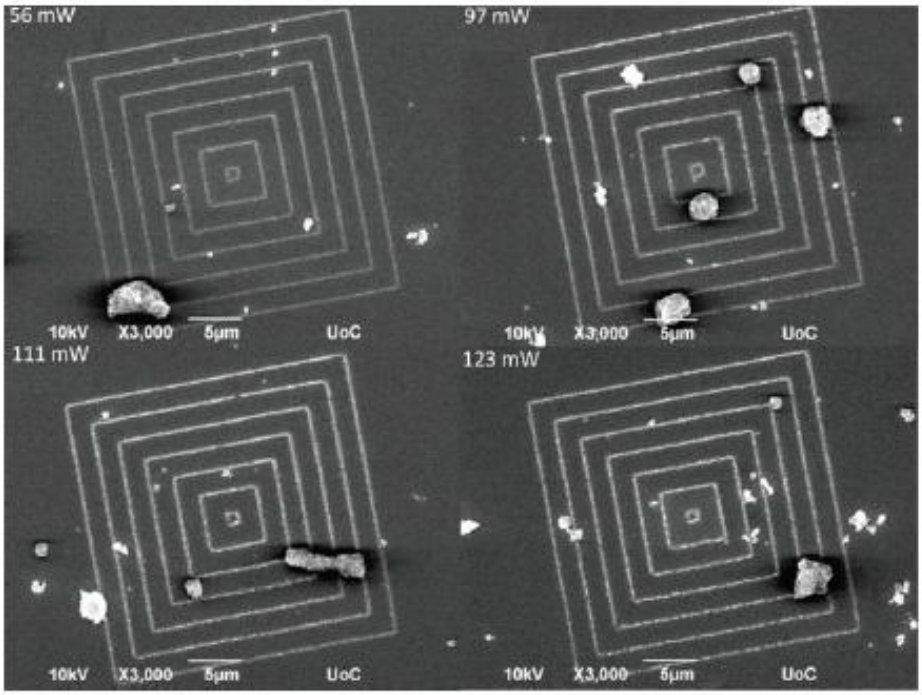


**Figure 77. SEM image of an array of concentric squares fabricated with the Ti:Sapphire laser from a solution of 100 mg/ml bBSA and 100 mg/ml BSA with 4 mM FMN. The laser beam was scanned at a speed of 0.4 mm/s and the average laser power was varied from 56 mW to 123 mW**

- 2D and 3D topography

The topography of the 2D and 3D crosslinked structures was analysed by comparing with each other the SEM images of structures fabricated with the two different laser sources and different protein compositions. The SEM images revealed some differences in the surface topography of the different protein structures. Avidin appeared to form quite uniform and dense lines when processed either with the Nd:YAG or with the Ti:Sapphire laser setup. The integrity of the avidin structures was likely also due to the very high protein concentration (400 mg/ml), which enabled efficient crosslinking of the protein.

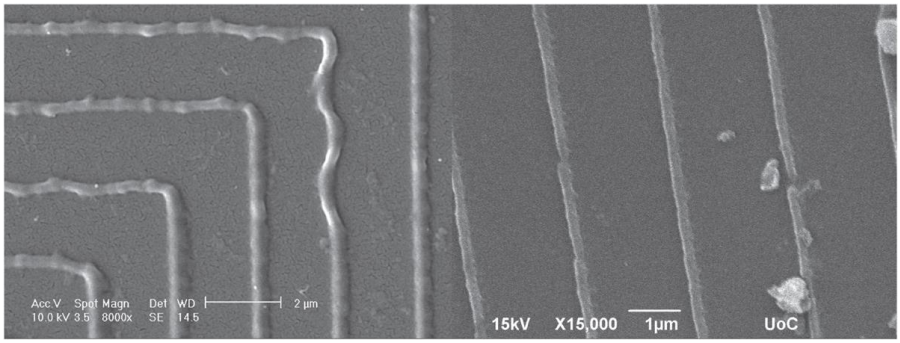


**Figure 78. Close-up SEM images of avidin lines crosslinked of a solution containing 400 mg ml−1 avidin with 2 mM FMN. (left) A linebstructure fabricated with the Nd:YAG laser setup with a scanning speed of 5 µm s−1 and an average power of 1.79 mW. (right) A line structure fabricated with the Ti:Sapphire laser setup at a scanning speed of 10 µm s−1 with an average power of 97 mW.**

In contrast to avidin, the structures fabricated from a solution of 100 mg/ml bBSA and 100 mg/ml BSA with 4 mM FMN had more porous and highly textured surface topography. The difference could be explained by the reduced crosslinking density of the more dilute BSA solution compared to the more concentrated avidin solution. However, both laser setups produced structures with quite similar grain characteristics.

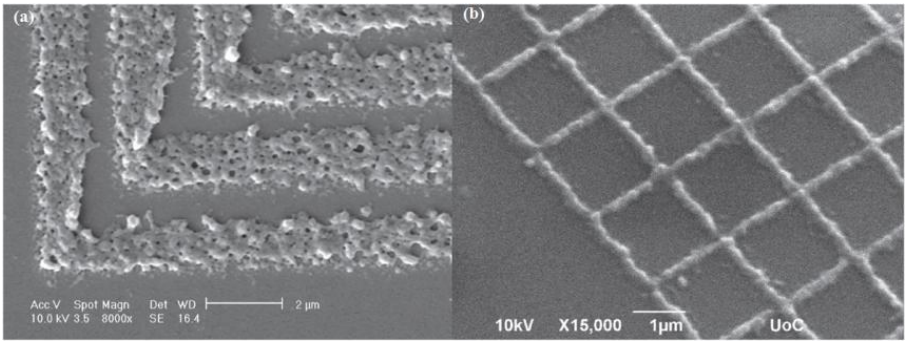


**Figure 79. SEM images of surface patterns fabricated from a solution of 100 mg/ml bBSA and 100 mg/ml BSA with 2 mM or 4 mM FMN, respectively. (*a*) A structure produced with the Nd:YAG laser with a scanning speed of 5 *µ*m/s and an average laser power of 1.79 mW. (*b*) A grid fabricated with the Ti:Sapphire laser by scanning the sample with a speed of 40 *µ*m/s and with an average laser power of 123 mW.**

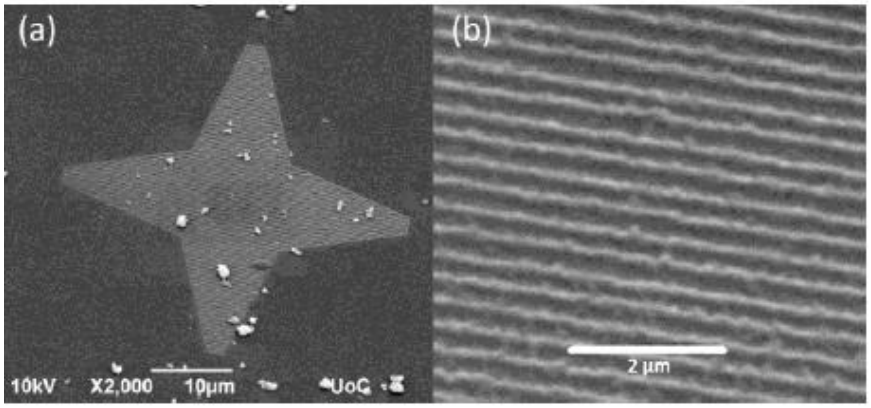


**Figure 80. (*a*) SEM image of a starshaped surface pattern fabricated from 200 mg/ml BSA with 4 mM FMN with the Ti:Sapphire laser by scanning the beam at 0.5 mm/s and with an average power of 56 mW and (*b*) a closeup of the individual protein lines within in the star.**

- Retention of ligand-binding ability of the avidin–biotin complex

The bioactivity of proteins is retained during the exposure to the high laser intensities required for efficient 2PA of the photosensitizer. It has been shown that endogenous proteins in live cells can become denatured due to accidental two and three-photon absorption when exposed to the irradiation from a Ti:Sapphire laser with a pulse width of 190 fs, wavelength of 840 nm and a pulse repetition rate of 82 MHz (Hopt and Neher 2001).

Fluorescence imaging was used as a qualitative tool to show that the patterns of avidin and bBSA retained their ability to bind either biotinylated or streptavidin conjugated fluorescence labels after photocrosslinking with the Nd:YAG laser. The fluorescence results showed that the bioactivity of the proteins was retained with the streptavidin binding capacity of the bBSA structures decreasing as the average laser power was lowered or the scanning speed was raised. If extensive thermal damage occurred during the polymerization, less binding of the streptavidin conjugated label would be expected at higher values of the laser power and at lower values of the scanning speed. **(Turunen, Käpylä et al. 2011)**

**Conclusions**

Short-pulse lasers are able to crosslink uniform protein patterns even with very fast scanning speed and the resolution and surface characteristics were exploited according to the material concentration, the laser power and scanning speed. After exposure to high laser intensities the structure's bioactivity was retained denoting that the protein microstructures could be utilized as chemical and topographical cues for cells.

## F. GENERAL CONCLUSIONS AND OUTLOOK

This study aimed at to the development of biocompatible high-precision scaffolds with complex architectures for applications in the field of biomaterials and photonics. In order to achieve this, the advantages of top-down laser fabrication (i.e. the possibility to control the scaffold geometry and micro-nano-topography) were combined with the bottom-up design possibilities of the self-assembling peptides (driving self-assembly from the nanoscale to millimeter scale). The combination of these two strategies on the 3D patterning of self-assembled peptides on hybrid structures was separated into two parts:

### 1) Part 1: Metallized structures for biosensing

- Novel photosensitive organic-inorganic materials were designed and synthesized using the sol-gel method, incorporating an organic monomer having a metal-binding affinity (DMAEMA). Among several scaffold fabrication techniques used, Direct femtosecond Laser Writing (DLW) by multiphoton polymerization was used for the construction of three-dimensional, readily assembled structures with sub-micron scale features.
- The influence of the metal binding content was examined on the material structurability, structure resolution and metallization quality. Following a silver plating technique a good compromise for resolution and conductivity was the addition of 30% DMAEMA in the hybrid photostructurable material for fabrication of 3D metallic micro/nanostructures exhibiting ohmic behaviour with conductivity $\sigma = (5.71 \pm 3.01) \cdot 10^{6}\ \Omega^{-1} \cdot m^{-1}$
- Previously studied metal-binding peptide fibrils were selectively positioned over the metallized 3D structures forming oriented peptide bridges which were further metallized in situ. This system can be used as a biosensor where the peptide plays both the role of the sensing and the recognition element. This could be achieved by depositing the sensing element on the fibril functionalized structure and after metallization measuring the voltage difference between the structures. Preliminary experiments showed that the conductivity of the system was not possible to be measured since the equipment available at UoC was destroying the fibril connections between the structures. Thus, in the context of this thesis, this project could not be carried to completion. Conductivity measurements of the system have to be further investigated by enlisting more appropriate experimental set-up and additional expertise from outside collaborations.

### 2) Part 2: Scaffolds for hard tissue engineering

- A novel approach to hard tissue regeneration was proposed based on "scaffold-on-scaffold" biofabrication. The primary 3D scaffolds were functionalized with attached secondary peptide scaffolds that could be used as a support for the directed growth of cells into biomineralized units.

- The fabrication and selection of an optimal scaffold containing 50% DMAEMA composite was investigated having mechanical properties similar to the ones of human cortical bone as well as and strong biological response, considering it as a novel material for 3D scaffold fabrication in hard tissue engineering applications.
- Self-assembling peptides were designed containing acidic amino acids in order to nucleate calcium. Bi-functional self-assembling octapeptides and nonapeptides DSGAITIG, DDGAITIG and DDSGAITIG, were specifically designed to attach on the gold ion layer covering the primary 3D scaffold, and act as a secondary scaffold for the deposition of calcium phosphate. The peptide DDSGAITIG was chosen for cell culture studies since it exhibited better and more homogenous mineralization quality.
- The observed strong pre-osteoblastic cell adhesion as well as proliferation increase and calcium production in the extracellular matrix (ECM) of pre-osteoblastic cells, makes the method promising and opens new possibilities for the development of high-precision scaffolds with complex geometries and architectures for engineered hard tissues.

- Moreover, the femtosecond laser system used for the fabrication of 3D structures was investigated over its ability to retain the bioactivity of proteins during the exposure to high laser intensities. For this purpose uniform protein micropatterns of avidin, bovine serum albumin (BSA) and biotinylated bovine serum albumin were fabricated by varying the system's power and scanning speed as well as the material's concentration. The photocrosslinked microscale protein topographies can be used for the guidance and the precise control of cellular architectures.

## E. BIBLIOGRAPHY


Addadi, L. and S. Weiner (1985). "Interactions between acidic proteins and crystals: stereochemical requirements in biomineralization." Proceedings of the National Academy of Sciences 82(12): 4110-4114.

Addadi, L. and S. Weiner (1992). "Control and Design Principles in Biological Mineralization." Angewandte Chemie International Edition in English 31(2): 153-169.

Aizenberg, J., V. C. Sundar, et al. (2004). "Biological glass fibers: Correlation between optical and structural properties." Proceedings of the National Academy of Sciences of the United States of America 101(10): 3358-3363.

Benders, K. E. M., P. R. v. Weeren, et al. (2013). "Extracellular matrix scaffolds for cartilage and bone regeneration." Trends in Biotechnology 31(3): 169-176.

Bernhard O. Palsson, S. N. B. (2004). Tissue Engineering, Prentice Hall

Bose, S., M. Roy, et al. (2012). "Recent advances in bone tissue engineering scaffolds." Trends in Biotechnology 30(10): 546-554.

Boskey, A. L. "Biomineralization: Conflicts, Challenges and Opportunities." Journal of Cellular Biochemistry Supplements 30/31: 83–91.

Boskey, A. L. (2007). "Mineralization of Bones and Teeth." E L E M E N T S 3: 387–393.

Braun, E., Y. Eichen, et al. (1998). "DNA-templated assembly and electrode attachment of a conducting silver wire." Nature 391(6669): 775-778.

Bruce Alberts, A. J., Julian Lewis, Martin Raff, Keith Roberts, and Peter Walter (2002). Molecular Biology of the Cell.

Buddy D. Ratner, A. S. H., Frederick J. Schoen,Jack E. Lemons (2004). Biomaterials Science: An Introduction to Materials in Medicine Elsevier.

C. Phipps, Springer Berlin / Heidelberg, Laser Ablation and its Applications. 129: 121-157.

Carny, O., D. E. Shalev, et al. (2006). "Fabrication of Coaxial Metal Nanocables Using a Self-Assembled Peptide Nanotube Scaffold." Nano Letters 6(8): 1594-1597.

Chen, Y.-S., A. Tal, et al. (2006). "Fabrication and Characterization of Three-Dimensional Silver-Coated Polymeric Microstructures." Adv. Funct. Mater. 16: 1739-1744.

Claeyssens, F., [1]E. A. Hasan, et al. (2009). "Three-Dimensional Biodegradable Structures Fabricated by Two-Photon Polymerization." Langmuir 25(5): 3219-3223.

Collier, J. H. and P. B. Messersmith (2001). "PHOSPHOLIPID STRATEGIES IN BIOMINERALIZATION AND BIOMATERIALS RESEARCH." Annual Review of Materials Research 31(1): 237-263.

D'Ippolito, G., P. C. Schiller, et al. (1999). "Age-Related Osteogenic Potential of Mesenchymal Stromal Stem Cells from Human Vertebral Bone Marrow." Journal of Bone and Mineral Research 14(7): 1115-1122.

Dalas, E. and P. G. Koutsoukos (1989). "The growth of calcium phosphate on ceramic surfaces." Journal of Materials Science 24(3): 999-1004.

Duan, X. M., H. B. Sun, et al. (2004). "Two-photon polymerization of metal ions doped acrylate monomers and oligomers for three-dimensional structure fabrication." Thin Solid Films 453-54: 518-521.

El-Kady, I., M. M. Sigalas, et al. (2000). "Metallic photonic crystals at optical wavelengths." Phys. Rev. B. 62: 15299.

Erhardt, M., K. Namba, et al. (2010). "Bacterial nanomachines: the flagellum and type III injectisome." Cold Spring Harbor perspectives in biology 2(11): a000299.

Espinosa, H. D., J. E. Rim, et al. (2009). "Merger of structure and material in nacre and bone – Perspectives on de novo biomimetic materials." Progress in Materials Science 54(8): 1059-1100.

Fouassier, J.-P. Photoinitiation, photopolymerization, and photocuring : fundamentals and applications, Munich; New York; Cincinnati, Hanser ; Distributed by Hanser/Gardner Publications.

Gazit, E. (2007). "Self-assembled peptide nanostructures: the design of molecular building blocks and their technological utilization." Chemical Society Reviews 36(8): 1263-1269.

Gazit, E. (2008). Self-Assembly of Short Peptides for Nanotechnological Applications. NanoBiotechnology. O. Shoseyov and I. Levy, Humana Press: 385-395.

Gelain, F., A. Horii, et al. (2007). "Designer Self-Assembling Peptide Scaffolds for 3-D Tissue Cell Cultures and Regenerative Medicine." Macromolecular Bioscience 7(5): 544-551.

Gorbitz, C. H. (2006). "The structure of nanotubes formed by diphenylalanine, the core recognition motif of Alzheimer's [small beta]-amyloid polypeptide." Chemical Communications 0(22): 2332-2334.

Hamodrakas, S. (1992). Molecular architecture of helicoidal proteinaceous eggshells, Springer-Verlag. 19: 116-186.

Hamodrakas, S. J., S. A. Asher, et al. (1982). Laser Raman studies of protein conformation in the silkmoth chorion.

Hamodrakas, S. J., T. Etmektzoglou, et al. (1985). "Amino acid periodicities and their structural implications for the evolutionarily conservative central domain of some silkmoth chorion proteins." Journal of Molecular Biology 186(3): 583-589.

Haske, W., V. W. Chen, et al. (2007). "65 nm feature sizes using visible wavelength 3-D multiphoton lithography." Opt. Express 15(6): 3426-3436.

Hauser, C. A. E. and S. Zhang (2010). "Designer self-assembling peptide nanofiber biological materials." Chemical Society Reviews 39(8): 2780-2790.

Hengsberger, S., A. Kulik, et al. (2002). "Nanoindentation discriminates the elastic properties of individual human bone lamellae under dry and physiological conditions." Bone 30(1): 178-184.

Ho, K. M., C. T. Chan, et al. (1994). "Photonic band gaps in three dimensions: new layer-by-layer periodic structures." Sol. Stat. Comm. 89: 413-416.

Hopt, A. and E. Neher (2001). "Highly Nonlinear Photodamage in Two-Photon Fluorescence Microscopy." Biophysical journal 80(4): 2029-2036.

Hutmacher, D. W. (2000). "Scaffolds in tissue engineering bone and cartilage." Biomaterials 21(24): 2529-2543.

Iconomidou, V. A., G. D. Chryssikos, et al. (2001). "Amyloid-like fibrils from an 18-residue peptide analogue of a part of the central domain of the B-family of silkmoth chorion proteins." FEBS letters 499(3): 268-273.

Iconomidou, V. A., Hamodrakas, S.J. (2010). Silkmoth chorion proteins: A protective role for amyloid Functional amyloid aggregation. S. R. a. M. Bucciantini, Research Signpost 71-88.

K. D, P. and R. K. M (1957). "The Silk of the Egg-Stalk of the Green Lace-Wing Fly: Structure of the Silk of Chrysopa Egg-stalks." Nature 179(4566): 905-906.

Kaneko, K., K. Yamamoto, et al. (2008). "Metal-nanoshelled three-dimensional photonic lattices." Optics Letters 33(17): 1999-2001.

Karageorgiou, V. and D. Kaplan (2005). "Porosity of 3D biomaterial scaffolds and osteogenesis." Biomaterials 26(27): 5474-5491.

Karambelas, G., S. Santhanam, et al. (2013). "Strombus gigas inspired biomimetic ceramic composites via SHELL—Sequential Hierarchical Engineered Layer Lamination." Ceramics International 39(2): 1315-1325.

Kasotakis, E. and A. Mitraki (2012). "Silica biotemplating by self-assembling peptides via serine residues activated by the peptide amino terminal group." Biopolymers 98(6): 501-509.

Kasotakis, E., E. Mossou, et al. (2009). "Design of Metal-Binding Sites Onto Self-Assembled Peptide Fibrils." Biopolymers 92(3): 164-172.

Kasotakis, E., E. Mossou, et al. (2009). "Design of metal-binding sites onto self-assembled peptide fibrils." Peptide Science 92(3): 164-172.

Khademhosseini, A., R. Langer, et al. (2006). "Microscale technologies for tissue engineering and biology." Proceedings of the National Academy of Sciences of the United States of America 103(8): 2480-2487.

Khan, Y., M. J. Yaszemski, et al. (2008). "Tissue Engineering of Bone: Material and Matrix Considerations." The Journal of Bone & Joint Surgery 90(Supplement_1): 36-42.

Kim, K., D. Dean, et al. (2011). "The influence of stereolithographic scaffold architecture and composition on osteogenic signal expression with rat bone marrow stromal cells." Biomaterials 32(15): 3750-3763.

Kiyan, R., C. Reinhardt, et al. (2007). "Rapid prototyping of optical components for surface plasmon polaritons." Opt. Express 15(7): 4205-4215.

Ko, F. K., S. Kawabata, et al. (2001). "Engineering Properties of Spider Silk." MRS Online Proceedings Library 702: null-null.

Konstantina, T., K. Erifyli, et al. (2013). "Mineralized self-assembled peptides on 3D laser-made scaffolds: a new route toward 'scaffold on scaffold' hard tissue engineering." Biofabrication 5(4): 045002.

Lau, M.-l., K.-t. Lau, et al. (2010). "Measurement of Bovine Bone Properties through Surface Indentation Technique." Materials and Manufacturing Processes 25(5): 324-328.

Lee, K.-W., S. Wang, et al. (2010). "Enhanced Cell Ingrowth and Proliferation through Three-Dimensional Nanocomposite Scaffolds with Controlled Pore Structures." Biomacromolecules 11(3): 682-689.

Lee SY, C. J., Royston E, Janes DB, Culver JN, Harris MT. (2006). "Deposition of platinum clusters on surface-modified Tobacco mosaic virus." Journal of Nanoscience and Nanotechnology 6: 974-981.

Lourtioz J.-M., Benisty H., et al. (2008). Towards Nanoscale Photonic Devices, Springer.

Luo, C., S. Johnson, et al. (2003). "Negative refraction without negative index in metallic photonic crystals." Opt. Express 11(7): 746–754.

Koutsopoulos, S. (2002). "Synthesis and characterization of hydroxyapatite crystals: A review study on the analytical methods." Journal of Biomedical Materials Research 62(4): 600-612.

Krampitz, G. and G. Graser (1988). "Molecular Mechanisms of Biomineralization in the Formation of Calcified Shells." Angewandte Chemie International Edition in English 27(9): 1145-1156.

Kumara, M. T., B. C. Tripp, et al. (2007). "Self-Assembly of Metal Nanoparticles and Nanotubes on Bioengineered Flagella Scaffolds." Chemistry of Materials 19(8): 2056-2064.

Lakes, R. (1993). "Materials with structural hierarchy." Nature 361: 511–515.

Lee, K.-S., D.-Y. Yang, et al. (2006). "Recent developments in the use of two-photon polymerization in precise 2D and 3D microfabrications." Polymers for Advanced Technologies 17(2): 72-82.

Liu Tsang, V. and S. N. Bhatia (2004). "Three-dimensional tissue fabrication." Advanced Drug Delivery Reviews 56(11): 1635-1647.

Liu, K. and L. Jiang (2011). "Bio-inspired design of multiscale structures for function integration." Nano Today 6(2): 155-175.

Luz, G. M. and J. F. Mano (2009). "Biomimetic design of materials and biomaterials inspired by the structure of nacre." Philosophical Transactions of the Royal Society A: Mathematical, Physical and Engineering Sciences 367(1893): 1587-1605.

Mann, S. (2001). Biomineralization Principles and Concepts in Bioinorganic Materials Chemistry, Oxford University Press.

Marc A. Meyers, A. Y. M. L., Yasuaki Seki, Po-Yu Chen, Bimal K. Kad, Sara Bodde (2006). "Structural biological composites: An overview." Journal of the Minerals, Metals and Materials Society 58: 35.

Maria Farsari, M. V. a. B. N. C. (2010). "Multiphoton polymerization of hybrid materials" Journal of OpticsEmail 12(12).

Meyer, U., Wiesmann, Hans Peter (2006). Bone and Cartilage Engineering.

n, G. B. o. i. v. i. (2007). "The hydroxyapatite crystal: a closer look." MEDICOGRAPHIA, VOL 29: 126-131.

Markus Deubel, G. v. F., Martin Wegener, Suresh Pereira, Kurt Busch and Costas M. Soukoulis (2004). "Direct laser writing of three-dimensional photonic-crystal templates for telecommunications." Nature Materials 3: 444-447.

Maruo, S., O. Nakamura, et al. (1997). "Three-dimensional microfabrication with two-photon-absorbed photopolymerization." Opt. Lett. 22(2): 132-134.

Moroz, A. (1999). "Three-dimensional complete photonic-band-gap structures in the visible." Phys. Rev. Lett. 83(25): 5274-5277.

Nasr, H. F., M. E. Aichelmann-Reidy, et al. (1999). "Bone and bone substitutes." Periodontology 2000 19(1): 74-86.

Nudelman, F., B. A. Gotliv, et al. (2006). "Mollusk shell formation: Mapping the distribution of organic matrix components underlying a single aragonitic tablet in nacre." Journal of Structural Biology 153(2): 176-187.

Ovsianikov, A., S. Passinger, et al. (2007). Three Dimensional Material Processing with Femtosecond Lasers

Palmer, L. C., C. J. Newcomb, et al. (2008). "Biomimetic Systems for Hydroxyapatite Mineralization Inspired By Bone and Enamel." Chemical Reviews 108(11): 4754-4783.

Papanikolopoulou, K., G. Schoehn, et al. (2005). "Amyloid Fibril Formation from Sequences of a Natural β-Structured Fibrous Protein, the Adenovirus Fiber." Journal of Biological Chemistry 280(4): 2481-2490.

Park, J. and R. Lakes (1992). Composites as Biomaterials. Biomaterials, Springer US: 169-183.

Pins, G. D., K. A. Bush, et al. (2006). "Multiphoton excited fabricated nano and micro patterned extracellular matrix proteins direct cellular morphology." Journal of Biomedical Materials Research Part A 78A(1): 194-204.

Reches, M. and E. Gazit (2003). "Casting Metal Nanowires Within Discrete Self-Assembled Peptide Nanotubes." Science 300(5619): 625-627.

Reinhardt, C., S. Passinger, et al. (2006). "Laser-fabricated dielectric optical components for surface plasmon polaritons." Opt. Lett. 31(9): 1307-1309.

Retsos, H., K. Papanikolopoulou, et al. (2005). "Amyloid character of self-assembling proteins based on adenovirus fiber shaft sequences." NanoBiotechnology 1(3): 219-225.

Richter, J., M. Mertig, et al. (2001). "Construction of highly conductive nanowires on a DNA template." Applied Physics Letters 78(4): 536.

Robert Lanza, R. L. a. J. V. (2007). Principles of Tissue Engineering, Elsevier Inc.

RR., B. (2002). "Limitations of autograft and allograft: New synthetic solutions." Orthopedics 25: S561–S570.

Saido, T. C. (2003). aβ metabolism and alzheimer's disease. Texas/US, Landes Bioscience.

Saiz, E., E. A. Zimmermann, et al. "Perspectives on the role of nanotechnology in bone tissue engineering." Dental Materials(0).

Seidlits, S. K., C. E. Schmidt, et al. (2009). "High-Resolution Patterning of Hydrogels in Three Dimensions using Direct-Write Photofabrication for Cell Guidance." Advanced Functional Materials 19(22): 3543-3551.

Shen, H.-R., J. D. Spikes, et al. (2000). "Photodynamic cross-linking of proteins: V. Nature of the tyrosine–tyrosine bonds formed in the FMN-sensitized intermolecular cross-linking of N-acetyl-l-tyrosine." Journal of Photochemistry and Photobiology A: Chemistry 133(1–2): 115-122.

Sievenpiper, D. F., M. E. Sickmiller, et al. (1996). "3D wire mesh photonic crystals." Phys.Rev. Lett. 76(14): 2480-2483.

Sigalas, M. M., C. T. Chan, et al. (1995). "Metallic Photonic Band Gap Materials." Phys. Rev. B 52(16): 11744-11751.

Spikes, J. D., H.-R. Shen, et al. (1999). "Photodynamic Crosslinking of Proteins. III. Kinetics of the FMN- and Rose Bengal-sensitized Photooxidation and Intermolecular Crosslinking of Model Tyrosine-containing N-(2-Hydroxypropyl)methacrylamide Copolymers." Photochemistry and Photobiology 70(2): 130-137.

Sun, Z. B., X. Z. Dong, et al. (2008). "Two- and three-dimensional micro/nanostructure patterning of CdS-polymer nanocomposites with a laser interference technique and in situ synthesis." Nanotechnology 19(3): 035611.

Takeyasu, N., T. Tanaka, et al. (2008). "Fabrication of 3D metal/polymer microstructures by site-selective metal coating." Applied Physics a-Materials Science & Processing 90(2): 205-209.

Tamamis, P., E. Kasotakis, et al. (2009). "Amyloid-Like Self-Assembly of Peptide Sequences from the Adenovirus Fiber Shaft: Insights from Molecular Dynamics Simulations." The Journal of Physical Chemistry B 113(47): 15639-15647.

Terzaki, K., A. Gaidukeviciute, et al. (2011). "Fabrication of three-dimensional conducting nanostructures by nonlinear lithography." CORD Conference Proceedings: 1-3.

Terzaki, K., Kalloudi, E., *et al* (2013). "Mineralized self-assembled peptides on 3D laser-made scaffolds: a new route toward 'scaffold on scaffold' hard tissue engineering" *Biofabrication* 5 045002

Terzaki, K., N. Vasilantonakis, et al. (2011). "3D conducting nanostructures fabricated using direct laser writing." Opt. Mater. Express 1(4): 586-597.

Terzaki, K., M. Kissamitaki, et al. (2013). "Pre-osteoblastic cell response on three-dimensional, organic-inorganic hybrid material scaffolds for bone tissue engineering." Journal of Biomedical Materials Research Part A

Thomas Scheibel, R. P., George Sawicki, Xiao-Min Lin, Heinrich Jaeger, Susan L Lindquist (2003). "Conducting nanowires built by controlled self-assembly of

amyloid fibers and selective metal deposition." Proc Natl Acad Sci U S A. 100(8): 4527–4532.

Turunen, S., E. Käpylä, et al. (2011). "Pico- and femtosecond laser-induced crosslinking of protein microstructures: evaluation of processability and bioactivity." Biofabrication **3**(4): 045002.

van Raaij, M. J. and A. Mitraki (1999). "A triple beta-spiral in the adenovirus fibre shaft reveals a new structural motif for a fibrous." Nature 401(6756): 935.

van Raaij, M. J. and A. Mitraki (2004). "Beta-structured viral fibres: assembly, structure and implications for materials design." Current Opinion in Solid State and Materials Science 8(2): 151-156.

van Raaij, M. J., A. Mitraki, et al. (1999). "A triple [beta]-spiral in the adenovirus fibre shaft reveals a new structural motif for a fibrous protein." Nature 401(6756): 935-938.

Vasilantonakis, N., K. Terzaki, et al. (2012). "Three-Dimensional Metallic Photonic Crystals with Optical Bandgaps." Advanced Materials 24(8): 1101-1105.

Verweij, H., T. M. A. R. Dubbelman, et al. (1981). "Photodynamic protein cross-linking." Biochimica et Biophysica Acta (BBA) - Biomembranes 647(1): 87-94.

Wagner, S. W. a. H. D. (1998). "THE MATERIAL BONE: Structure-Mechanical Function Relations." Annual Review of Materials Science 28: 271-298

Waleed Shinwari, M., M. Jamal Deen, et al. (2010). "Electrical Conductance in Biological Molecules." Advanced Functional Materials 20(12): 1865-1883.

Weiner, S. (2003). "An Overview of Biomineralization Processes and the Problem of the Vital Effect." Mineralogical Society of America 54: 1-31.

Weiner, S. and L. Hood (1975). "Soluble protein of the organic matrix of mollusk shells: a potential template for shell formation." Science 190(4218): 987-989.

Wenk, H. R. and F. Heidelbach (1999). "Crystal alignment of carbonated apatite in bone and calcified tendon: results from quantitative texture analysis." Bone 24(4): 361-369.

West, L. L. H. a. J. K. "The sol-gel process." Chem. Rev. 90: 33-72.

Whitford, D. (2005). Proteins:Structure and Function, John Wiley & Sons, Ltd.

Yeong, W.-Y., C.-K. Chua, et al. (2004). "Rapid prototyping in tissue engineering: challenges and potential." Trends in Biotechnology 22(12): 643-652

Zhang, S. (2002). "Emerging biological materials through molecular self-assembly." Biotechnology Advances 20(5–6): 321-339.

Zhang, S., T. Holmes, et al. (1993). "Spontaneous assembly of a self-complementary oligopeptide to form a stable macroscopic membrane." Proceedings of the National Academy of Sciences 90(8): 3334-3338.

Zuo, R., D. Örnek, et al. (2005). "Aluminum- and mild steel-binding peptides from phage display." Applied Microbiology and Biotechnology 68(4): 505-509.